Title	Time-resolved Resonance Raman Studies on Quaternary and Tertiary Dynamics of Human Adult Recombinant Hemoglobin
Author(s)	Chang, Shanyan
Citation	大阪大学, 2016, 博士論文
Version Type	VoR
URL	https://doi.org/10.18910/59522
rights	
Note	

Doctoral Thesis

Title of Thesis　Time-resolved Resonance Raman Studies on Quaternary and Tertiary Dynamics of Human Adult Recombinant Hemoglobin

(時間分解共鳴ラマン分光法を用いた Human Adult Recombinant Hemoglobin の四次および三次構造ダイナミクスに関する研究)

Department: Department of Chemistry
Name: Shanyan CHANG

Graduate School of Science, Osaka University

Table of Contents

Chapter 1 Introduction

1.1 A paradigmatic allosteric protein – Human Adult Hemoglobin

Allostery is a phenomenon that “*indirect* interactions are established between *topographically distinct* sites and mediated by a discrete reversible *alteration* in the molecular structure of the protein”[1]. Allosteric interactions account for the regulation of the activity of many enzymes and regulatory proteins. Although the first allosteric model, the Monod-Wyman-Changeux (MWC) model[2], has been published for about 50 years, the detailed mechanism of protein allostery remains mysterious. Human adult hemoglobin (HbA) is a paradigm to study the mechanism of protein allostery, and continues to offer the best platform for developing mechanistic insight.

HbA is a good example to understand the concept of allostery. The major physiological function of HbA is to transport oxygen (O_2), therefore, it is indispensable in the processes of respiration and metabolism. HbA contains four binding sites of (O_2), which locate far apart from one another[3]. However, the apparent ligand affinity of HbA increases with the degree of saturation, which implies that certain *indirect* interactions must exist between these *distant* binding sites. The structural basis of this phenomenon is the reversible *quaternary transition* between the low-affinity (T or tense) state and the high-affinity (R or relaxed) state, which was first proposed by the MWC model[1] and then verified by a substantial amount of X-ray crystallographic studies[4].

HbA has been widely employed as a paradigmatic allosteric protein due to its important physiological function, as well as its extensive database of structure and function[1, 2, 5]. HbA was among the first proteins to be sequenced and its globin genes were almost the earliest to be cloned. So far, there are about 200 entries in the protein data bank to record the X-ray crystal structures of HbA, its mutants and chemically modified species. In addition, study of the more than 1000 naturally occurring Hb variants, which contain single amino acid substitutions throughout the molecule, have provided a wealth information on understanding the structure-function properties of HbA.

Due to these reasons, HbA was chosen as the target protein in this present study, in order to get some insights into the allosteric mechanism of proteins. The quaternary and tertiary dynamics of several Hb species have been carefully investigated, the implications of which have been discussed substantially.

1.2 Human Adult Hemoglobin

1.2.1 Structure of HbA

HbA is a heterotetramer composed of two α- and two β-subunits. Each α-subunit contains 141 amino acids; while β-subunit is slightly longer, composed by 146 amino acids. α- and β-subunits share similar structural and functional properties.

Figure 1-1A shows the tertiary structures of α- and β-subunits, most of which are composed by α-helices. In general, the tertiary structures are similar, unless that the β-subunit contains an additional D-helix. Each subunit bears a prosthetic group, iron-protoporphrin IX, which is often referred to as heme. As shown in Figure 1-1B, heme is a large heterocyclic organic ring made up of four pyrrolic groups joined together by methine bridges. The ferrous ion (Fe^{2+}) in the center of the heme is coordinated to four nitrogen atoms of the pyrrolic groups. In addition, the Fe^{2+} is also coordinated to a histidine residue in F-helix (as shown in Figure 1-1A). The sixth coordination site is responsible for binding of diatomic molecules, such as, oxygen (O_2), carbon monoxide (CO), or nitric oxide (NO) (Figure 1-1A, pink spheres).

The tetrameric HbA is actually a “dimer’s dimer”. One α- and one β-subunit form a αβ dimer, and then two dimmers associate into a tetramer, as shown in Figure 1-1C. Within the tetramer, the interface between the α subunit of one dimer and the β subunit of the other dimer is termed as $\alpha_1\beta_2$ interface (Figure 1-1C). The $\alpha_1\beta_2$ interface is stabilized/destabilized upon ligand dissociation/binding, resulting in a reversible transition of the quaternary structure between the T and R states (detailed information is introduced in Section 1.2.2). Figure 1-1D is an example of the crystal structure of Hb tetramer.

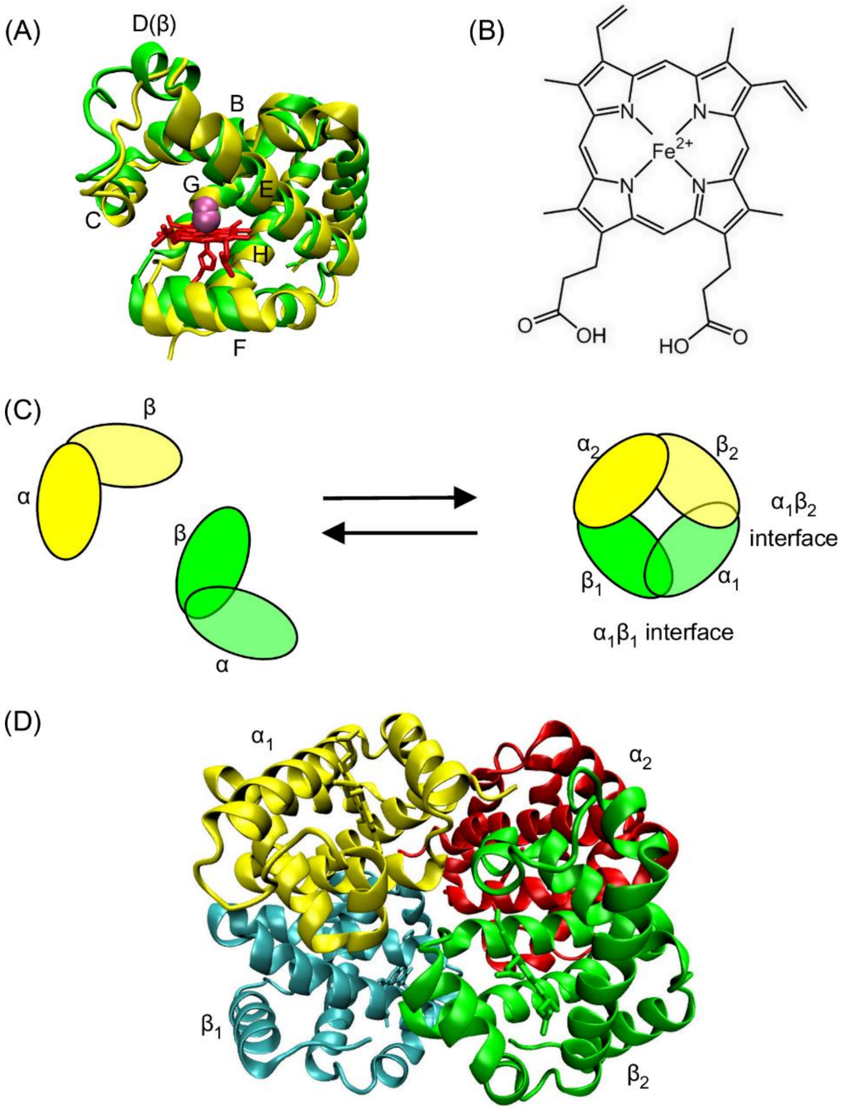

Figure 1-1 Structure of HbA. (A) Tertiary structures of α- (yellow) and β-subunits (Green). The heme group and proximal histidine of α-subunit are colored in red. The pink spheres represent carbon monoxide (CO). (B) The chemical structural formula of heme. (C) The process of two αβ dimers associate into a tetramer. (D) Quaternary structure of HbA.

1.2.2 Quaternary transition between R and T states

HbA has two quaternary states, a “T” (tense, low affinity, unliganded) and a “R” (relaxed, high affinity, ligand-bound) state. Transitions between T and R are mediated largely through $\alpha_1\beta_2$ interactions. The quaternary transition between T and R states is initiated by ligand binding/dissociation. The pink spheres in Figure 1-2A to 1-2C represent the Fe^{2+}. In the ligand-bound forms (Figure 1-2A), the $Fe^{2+}$is in the heme plane, so that we cannot see it. Meanwhile, the proximal histidine (His) is almost perpendicular to the heme. However, in the unliganded form, the Fe^{2+} is out of plane and the proximal His is obviously tilted (Figure 1-2B). Figure 1-2C overlaps the ligand-bound and unliganded structures, it seems that the ligand moves the Fe^{2+} into the heme plane, while the proximal His pull the Fe^{2+}out of the plane. These local structural perturbations in heme can be propagated through a series of α-helices to the $\alpha_1\beta_2$ interface, and then to another subunit, eventually resulting in the quaternary structural transition, as shown in Figure 1-2D.

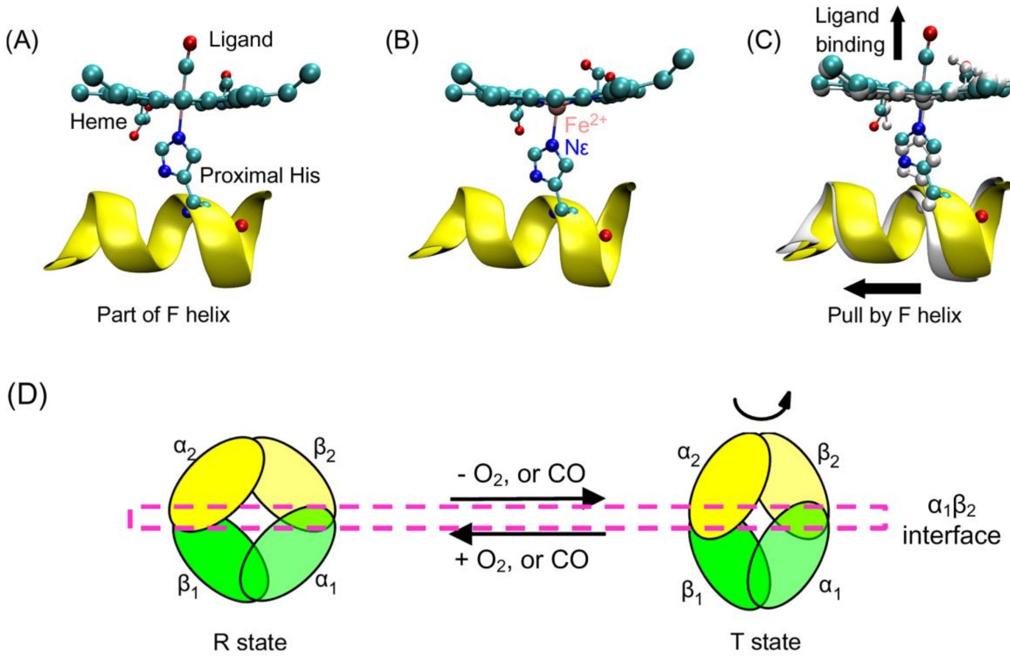

Figure 1-2Structure of heme and its adjacent residues in ligand-bound (A) and unliganded (B) forms. (C) overlaps (A) and (B). (D) Schematic view of the reversible quaternary transition between R and T states.

1.2.3 Quaternary dynamics of HbA

As early as 1979, Baldwin and Chothia[6] proposed the famous model to describe the R→T transition, by comparing the X-ray crystal structures of deoxy-Hb and CO-Hb. The schematic diagram of their model is shown in Figure 1-3A. They found that no significant structural change occurs in the central regions of the αβ dimer, therefore, the αβ dimer can be regarded as a semi-rigid body. On the other hand, the R→T quaternary transition is interpreted as the relative rotation/translation of the two αβ-dimers. All other structural changes are considered as tertiary relaxations. This model has been widely accepted and written in many textbooks, and is still being cited by most of the researchers.

However, Baldwin and Chothia's only examined the T and R end states. Time-resolved measurements are necessary to uncover the allosteric pathway. The earliest time-resolved absorption spectroscopic study suggested that the R→T transition occurred at ~20 μs[7], however, recent time-resolved studies challenged this perspective. In 2004, Spiro et al[8] monitored the allosteric transition of Hb following CO photolysis with a combination of time-resolved absorption and UV resonance Raman (UVRR) spectroscopy. Their results suggested that the R→T quaternary transition had a fast (3 μs) as well as a slow (20 μs) step (Figure 1-3B). Until recently, Cammarata's group applied their newly developed technique of time-resolved wide-angle X-ray scattering (TR-WAXS)[9, 10] and it into the study of Hb dynamics, demonstrating that the main structural rearrangement of the R→T transition takes place at ~2 μs.

Besides these time-resolved techniques, the simulation method has also been employed in the study of Hb quaternary transitions. In 2011, Karplus[11] calculated the minimum energy pathway (MEP) of the transition path between T and R states, the result of which also suggested that the R→T quaternary transition has two steps (Figure 1-3D). The early large quaternary change would correspond to the relative rotation of two αβ-dimers, whereas the smaller late quaternary change would correspond to a simultaneous rotation of each α-subunit relative to the 'stationary' $\beta_1\beta_2$-

dimer.

In all, the studies on the quaternary dynamics of HbA imply that the R→T allosteric transition pathway is composed by at least two quaternary steps, one at ~2 μs and the other at ~20 μs. It is also indicated that the main quaternary transition occurs in the first step (~2 μs).

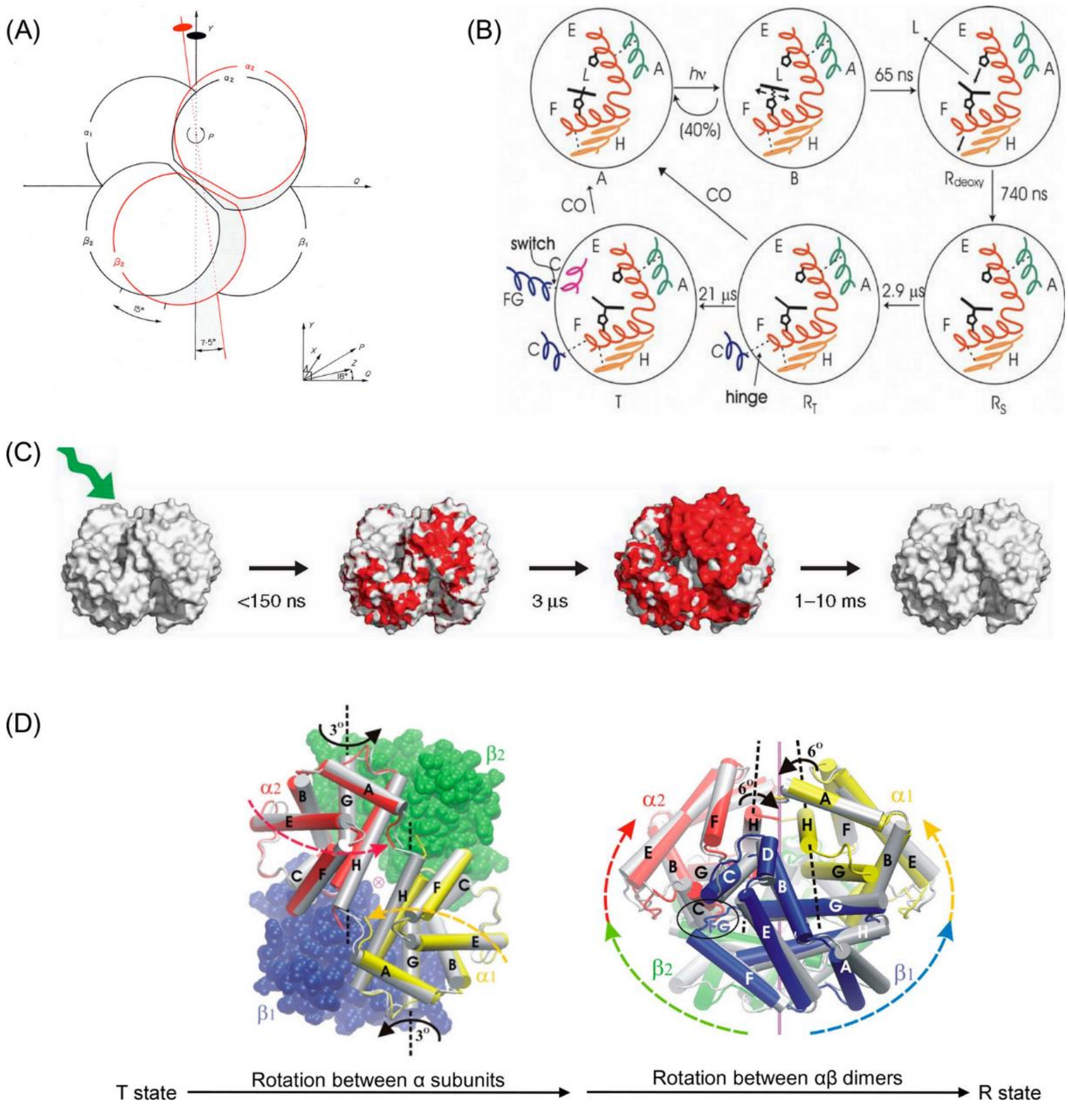

Figure 1-3. Quaternary dynamics of HbA. (A) Schematic diagram of Baldwin and Chothia's model[6]. T and R states are colored by black and red, respectively. (B) Spiro's stepwise quaternary transition model[8]. (C) Cammarata's model[10] as revealed by time-resolved wide-angle scattering. (D) Karplus' model[11] as suggested by calculating the minimum energy pathway.

1.2.4 Tertiary dynamics of HbA

1.2.4.1 Rotation of E-F clamshell

Within each subunit, the E and F helices form a “clamshell” around the heme, hinged at the EF corner, as shown in Figure 1-4A. The proximal histidine at the F helix is covalently linked to heme. On the other hand, the distal histidine at E helix forms hydrogen bond with the ligand. Therefore, the E and F helices are very sensitive to the structural perturbations in heme. UVRR studies have revealed that, upon the broken of the Fe-CO bond, the displacement of Fe^{2+} from the heme plane results in the motion of F helix away from the heme. On the distal side, upon the escaping of CO, the empty space left by CO allows the E helix to move toward the heme. The concerted motion of E and F helices produces a rotation of the “clamshell” relative to the heme, as shown in Figure 1-4A. UVRR studies indicated that the rotation of the E-F clamshell occurs at ~65 ns after the photolysis of CO (Figure 1-4B).

1.2.4.2 Break and restore of interhelical hydrogen bonds

The E-F “clamshell” mentioned in Section 1.2.4.1 is tethered to A and H helices by hydrogen bonds (H-bond), which are referred as “interhelical H-bonds” (Figure 1-4A). The H-bond connecting the E and A helices is between the Trpα14/β15 of the A helix and the Thrα67/Serβ72 of the E helix. In addition, the H-bond between F and H helices is constituted by the Tyrα140/β145of the H helix and the Valα93/β98of the F helix.

Spiro’s UVRR studies demonstrated that the rotation of the E-F “clamshell” leads to the weakening of these “interhelical H-bonds”, which takes place at ~65 ns as well. Moreover, they also discovered that these “interhelical H-bonds” restores at ~740 ns.

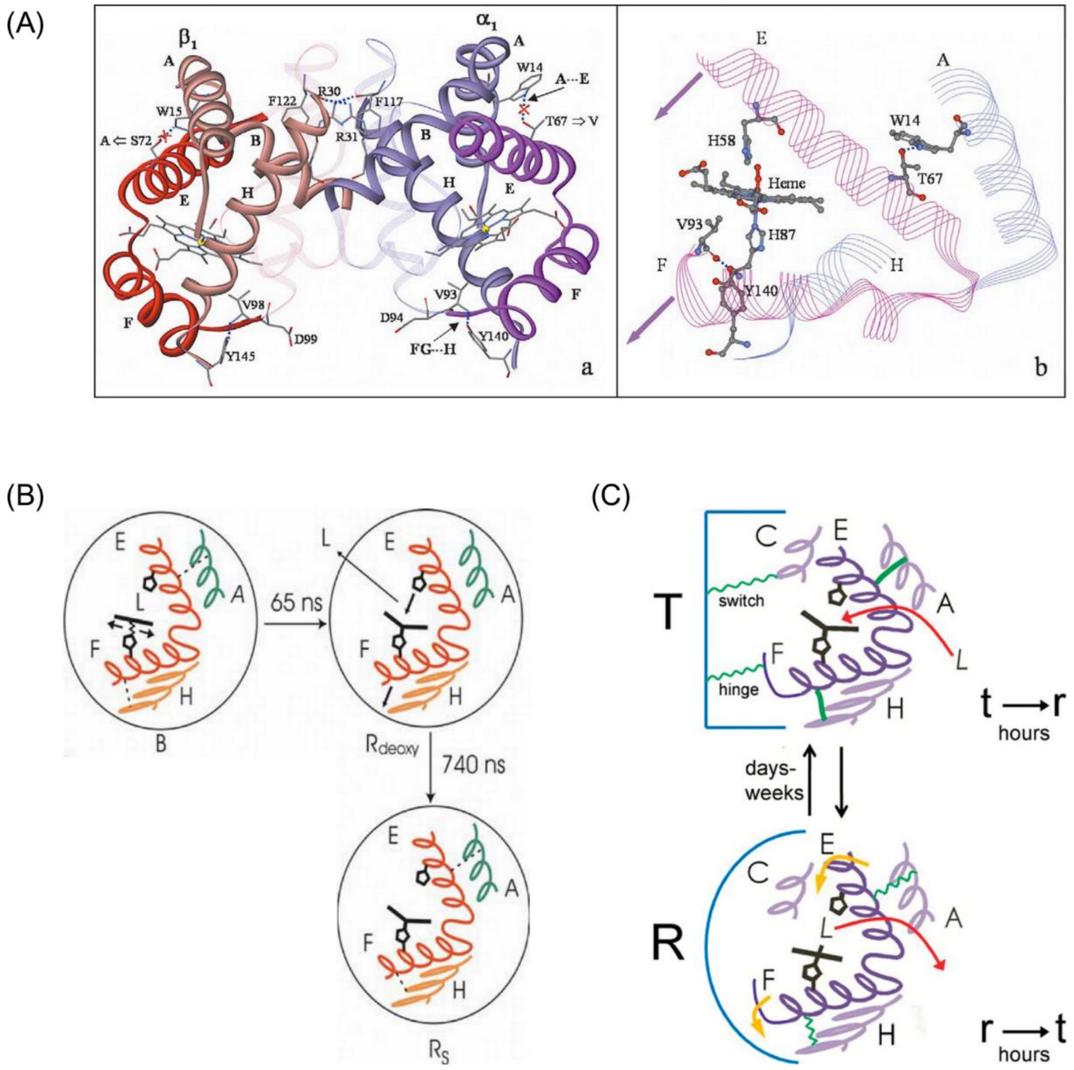

Figure 1-4. Tertiary dynamics of HbA. (A) Ribbon diagram showing the relative positions of A, E, F, H helices and the heme plane[12]. (B) Part of Spiro's stepwise model[8], showing the tertiary dynamics. (C) Tertiary dynamics of HbA encapsulated in sol-gel[13].

1.2.4.3 Tertiary dynamics of Hb in gel

Recently, Spiro and his colleagues[13] encapsulated Hb in silica sol-gels to investigate the dynamics of Hb, using the time-resolved visible and UVRR spectroscopy. They made two improvements in their tertiary dynamic model, as seen in Figure 1-4C.

(1) In R quaternary structure, the A-E H-bond breaks well before the F-H H-bond, which modifies the concerted breaking of the A-E and F-H H-bonds detected in solution.

(2) The T quaternary structure constrains E and F helices from rotation by the intersubunit H-bonds at the $\alpha_1\beta_2$ interface.

1.2.5 Naturally occurring Hb mutants

So far, over 1000 naturally occurring Hb mutants have been discovered. Those Hb mutants with single amino acid substitutions at the $\alpha_1\beta_2$ interface always have abnormal oxygen affinity and reduced cooperative[14]. For example, some of these Hb mutants only prefer one quaternary state. Therefore, only tertiary structural changes happen after the photodissociation of CO. Hb Kempsey and Hb Kansas are two representatives of them. By the way, these mutants were named after the geographic origin of the affected individual[14].

1.2.5.1 Hemoglobin Kempsey

Hemoglobin Kempsey (Hb Kempsey) is a naturally occurring Hb mutant with increased oxygen affinity and little cooperativity, which results from the single amino acid substitution at β99 (βD99→N)[15]. This mutation prevents the formation of a hydrogen bond between β_2D99 and α_1Y42 in T state, consequently, destabilizing the T quaternary state and shifting the quaternary equilibrium toward R state. The R-type quaternary structure of deoxy-Hb Kempsey is supported by NMR[16] and functional[17] studies.

1.2.5.2 Hemoglobin Kansas

Hemoglobin Kansas (Hb Kansas) is an Hb mutant with abnormally low oxygen affinity and a small degree of cooperativity[18], in which the 102nd residue of the β-subunit (asparagine) was replaced by threonine (βN102→T)[19]. In HbA, a hydrogen bond between β_2N102 and α_1D94 specifically stabilize the R state. Therefore, replacement of βN102 to a neutral amino acid (N) abrogates this hydrogen bond and shifts the quaternary equilibrium toward T state. A crystallographic evidence confirms that the liganded Hb Kansas possesses a T-type quaternary structure[20]. In addition, NMR studies carried out in solution proved that the fully liganded Hb Kansas can be switched to T quaternary state with the help of IHP at low pH[21].

1.3 Resonance Raman Spectroscopy

Resonance Raman (RR) spectroscopy with visible excitation was utilized in this study to probe the tertiary as well as quaternary structural changes of Hb. In this section, the principle of RR spectroscopy was introduced first. After that, the application of RR spectroscopy on the study of Hb was briefly reviewed.

1.3.1 Principle of RR spectroscopy

1.3.1.1 Raman scattering

When a monochromatic wave ($h\nu_0$) passes over a molecule, the energy present in the wave may be transferred into the molecule and then immediately released as scattered radiation. There are two types of scattering, as illustrated in Figure 1-5. Rayleigh scattering is the most intense one. It is an elastic process and the scattered wave ($h\nu_0$) is the same in energy as the incident one. The other type of scattering is much rarer and termed as Raman scattering. If Raman scattering occurs, the vibrational state of the molecule will alter, so that the energy of the scattered wave will be either lower ($h(\nu_0-\nu)$, Stokes scattering)or higher ($h(\nu_0+\nu)$, anti-Stokes scattering)than that of the incident wave. Apparently, the energy difference between the Raman scattered wave and the incident wave ($\pm h\nu$) is in quantity equal to the energy difference of two vibrational states of the molecule. Therefore, Raman spectroscopy can provide valuable structural information on molecules.

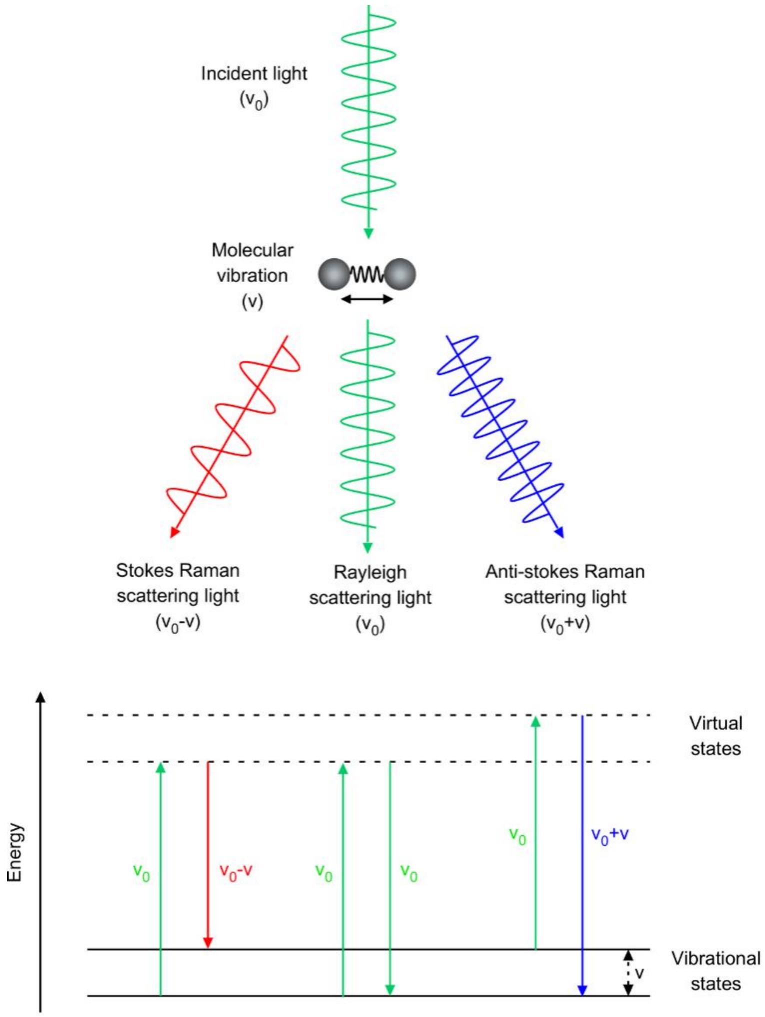

Figure 1-5. Rayleigh and Raman scatterings

1.3.1.2 Resonance Raman scattering

Suppose that there is a Raman scattering process, molecules initially in the vibrational state *m* are excited by a monochromatic wave ($h\nu_0$), and eventually relax to a vibrational state *n*. Accordingly, the intensity of this process (*I*) is defined by Eq. (1-1):

$$I = \frac{128\pi^5}{9c^4}(\nu_0 \pm \nu)^4 I_0 \sum_{\sigma,\rho} \left|(\alpha_{\rho\sigma})_{mn}\right|^2 \tag{1-1}$$

In Eq. 1-1, *c* is the speed of light, ν is the observed Raman shift, and I_0 is the intensity of the incident wave. Therefore, once the power (I_0) and the frequency (ν_0) of the incident light are set, the intensity of the Raman scattering (*I*) for a given Raman mode at frequency (ν) is only determined by the polarizability of the molecule (α).

$(\alpha_{\rho\sigma})_{mn}$ is an component of the polarizability tensor, which is described using the Kramer Heisenberg Dirac (KHD) expression, as shown in Eq. (1-2).

$$(\alpha_{\rho\sigma})_{mn} = \frac{1}{h}\sum_{e}\left[\frac{\langle n|\mu_{\rho}|e\rangle\langle e|\mu_{\sigma}|m\rangle}{\nu_{em}-\nu_{0}+i\Gamma_{e}}+\frac{\langle n|\mu_{\sigma}|e\rangle\langle e|\mu_{\rho}|m\rangle}{\nu_{en}+\nu_{0}+i\Gamma_{e}}\right] \qquad \text{Eq. (1-2)}$$

In this equation, *m* is the initial vibronic state, *e* is a vibronic state of an excited electronic state (abbreviated as “excited state”), and *n* is the final vibronic state of the ground state. Σ is the sum over all vibronic states of the excited electronic state.

Consider the numerators first. μ_ρ and μ_σ are dipole operators. The subscripts ρ and σ represent the incident and scattered polarization directions, respectively. Each triple interval in the numerators mixes two corresponding states. Altogether, the numerators describe electronic states of the molecule which exist only when the molecule is excited to the virtual energy state.

In the denominators, ν_{em} describes the energy difference between the excited and the initial state, similarly, ν_{en} corresponds to the energy difference between the excited and the final state. $i\Gamma_e$ is a damping factor, which is small relative to the energies ν_{em} and ν_{en} but cannot be omitted. In the 2nd term, ν_{en} and ν_0 are added, so that the denominator will always be larger than that of the Hence, the 2nd term is less important in Raman scattering and let’s focus on the 1st term.

If the frequency of the incident light (ν_0) is similar to the frequency of the electronic transition (ν_{em}), the denominator of the 1st term will become so small that the Raman scattering will be greatly enhanced by several orders of magnitude (10^4 to 10^6). This phenomenon is called resonance Raman scattering.

1.3.1.3 Characteristics of RR spectroscopy

RR spectroscopy has been more and more popular in recent years, due to its high sensitivity and selectivity. In normal Raman spectroscopy, the Raman signals may be sheltered by the intense fluorescence signals. Nevertheless, when the resonance condition occurs, the intensity of the

Raman signal will be enhanced by 10^4-10^6. As a result, the fluorescence interference becomes less significant, and the RR spectroscopy becomes a much more sensitive technique.

The high selectivity means some part of the molecule can be selectively probed by RR spectroscopy. This can be achieved when at a particular frequency, some part of the molecule has an intense electronic transition but the rest of the molecule does not. So, if this particular frequency is used to excite the molecule, RR scattering will occur at some part of the molecule but not at the rest part. Consequently, this particular part of the molecule can be selectively investigated. This characteristic of RR spectroscopy is extremely useful when we want to exclusively study the chromophore of a very large molecule. For example, in this study, the heme chromophore of Hb was selectively investigated.

There are still some advantages of RR scattering, which limit its application. Raman scattering is a two photon process, the probability of which is still lower than the one photon processes, such as, absorption. Therefore, the application of RR spectroscopy requires high sensitive detectors, for instance, the multichannel detector CCD. In addition, a powerful probe laser is liable to cause protein decomposition. The spinning cell technique was used in this study to prevent the protein decomposition as much as possible.

1.3.2 RR studies of Hb

RR spectroscopy has been popular for the study of Hb, since its prosthetic group, the heme, has strong RR signals. The chemical structural formula of heme is shown in Figure 1-1. The π-π^* transitions from the porphyrin ring of the heme group give rise to a very intense electronic absorption band at about 400-430 nm, called Soret band (Figure 1-6). Visible excitation near Soret absorption band produces RR bands of the heme chromophore (Figure 1-7). Among these RR bands shown in Figure 1-6, the ν(Fe-His), ν_8, ν_4, and ν_3 bands have been used as marker bands to monitor the structural changes of the heme pocket, as well as the tertiary and quaternary transition of Hb. Therefore, the origin and significance of these four bands are illustrated in detail in this section.

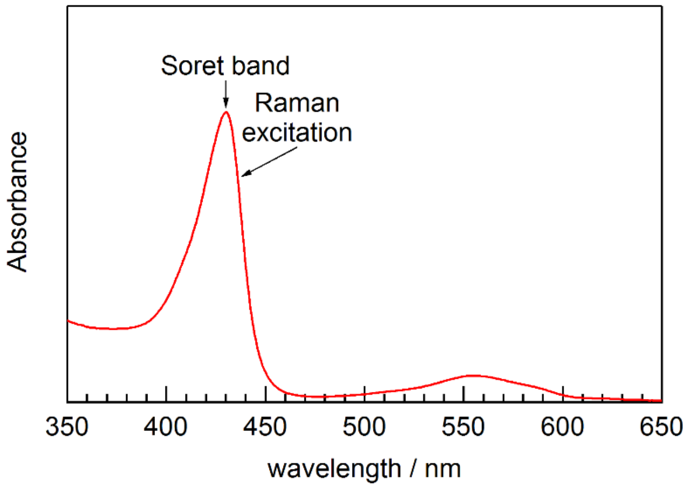

Figure 1-6. UV-visible absorption band of deoxy-form Hb.

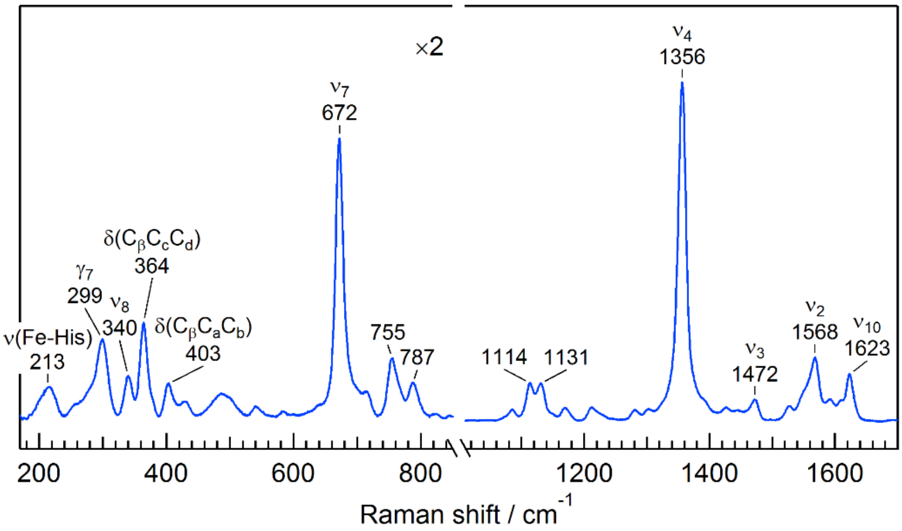

Figure 1-7. An example of heme-resonant Raman spectra of Hb.

1.3.2.1 ν(Fe-His) mode

The ν(Fe-His) band near 210-230 cm^{-1} originates from the stretching mode of the bond between the heme Fe^{2+} and the N_ε atom of the proximal histidine (i.e., the Fe-N_{His} bond)[22], as shown in Figure 1-8A. The Fe-N_{His} bond is the only covalent link between the heme group and the protein globin, therefore plays a very important role in the realization of the cooperativity of Hb. The generally accepted theory[6, 23] demonstrates that the cooperativity of Hb consists of a change of tension at hemes, caused by a quaternary transition between R and T states. Part of the tension stores at the Fe-N_{His} bond: in R state, the bond is relaxed and is perpendicular to the heme plane; however, the bond in T state becomes tense since it is tilted and lengthened. The change of Fe-N_{His} bond in orientation and bond length is supposed to result in the frequency variation of the ν(Fe-His) Raman band.

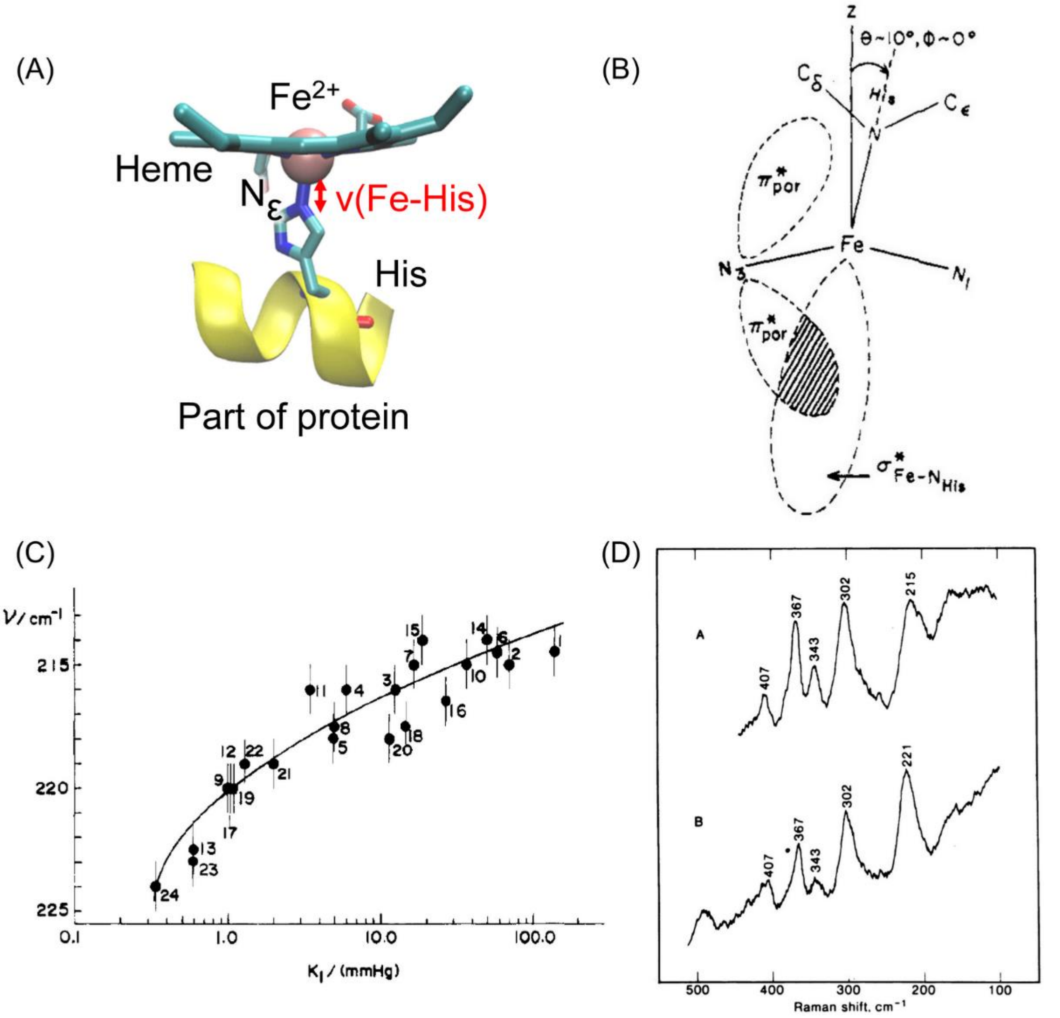

Figure 1-8. ν(Fe−His) band. (A) Vibrational mode. (B) A diagrammatic representation of the coupling between the ν(Fe−His) mode and the Soret transition (π_{por}-π^*_{por})[24]. (C) The ν(Fe−His) vs. K_1 plot[25]. (D) Examples of the ν(Fe−His) frequency in T (upper) and R (lower) quaternary states[26].

The ν(Fe−His) Raman band can be substantially enhanced using Soret excitation[24]. However, it is observable only for five-coordinate Hb species (deoxy-Hb or unliganded transient generated by photolysis), not for the six-coordinate liganded species[27]. These characteristics of the ν(Fe−His) band can be explained by Figure 1-8B[24]. In five-coordinate Hb species, the Fe-N_{His} bond is tilted relative to the normal of the heme plane by angle θ, so that the orbital mixing of π^*_{por} and $\sigma^*_{Fe\text{-}N_{His}}$ occurs. As a result, the ν(Fe−His) mode is relatively strongly coupled to the Soret transition (π_{por}-π^*_{por}). Unfortunately, for six-coordinate Hb species, no $\sigma^*_{Fe\text{-}N_{His}}$-$\pi^*_{por}$ mixing takes place, since the Fe-N_{His} bond is perpendicular to the heme plane (θ=0). Therefore, the ν(Fe−His) mode is no longer coupled to the Soret transition. Although the equilibrium liganded species has no ν(Fe−His) signal, the ν(Fe−His) band of R-state Hb can still be detected with other methods, for example, with the help of naturally occurring Hb variants[25], chemically modified Hb species[26, 28], or the photolysis technique[29]. No matter what method has been used, same phenomena have been observed.

The ν(Fe‑His) frequency has been correlated with the heme reactivity[25].As shown in Figure 1-8C, the variation of the ν(Fe‑His) frequency has been correlated with the dissociation constant of oxygen which leaves oxyHb last (K_1)[25].In addition, a ~4 cm^{-1} shift of the ν(Fe‑His) frequency corresponds to an increase of K_1 by one order of magnitude, meaning that the ν(Fe‑His) frequency is a very sensitive marker of the heme reactivity.

In addition, a frequency difference has been observed between R and T quaternary states[26, 28, 29]. Generally speaking, the ν(Fe−His) frequency of a typical R-state species is higher as compared with a typical T-state species, an example of which is shown in Figure 1-8D[26]. Furthermore, using time-resolved RR spectroscopy, Jayaraman *et al*[30] successfully observed a sequential frequency shift of the ν(Fe−His) band (228→224→222→216 cm^{-1}) upon the CO photolysis.

In all, these experimental evidences verify that the ν(Fe−His) frequency is a very important structural marker, not only for probing local structural perturbations in heme upon ligand combination/dissociation, but also for monitoring the quaternary transition of Hb.

1.3.2.2 ν_8-Peripheral interaction

For deoxy Hb, the mode at ~340 cm^{-1} is assigned to ν_8, a metal-pyrrole stretch and substituent bending mode (Figure 1-9A)[31]. This mode is sensitive to movements of the heme and its two propionate substituents relative to the globin[32]. When the two propionates are in a well-defined geometry, the ν_8 band is relatively prominent. As the two propionates become more disordered, the ν_8 intensity decreases. Besides that, the ν_8 mode is also sensitive to changes of the distal side of the heme pocket[33]. When the distal His is substituted to Arg[33] or Glu[34], the temporal variation of the ν_8 frequency after CO photolysis is altered. In all, the ν_8 mode is a good spectral marker for the environments of the heme pocket.

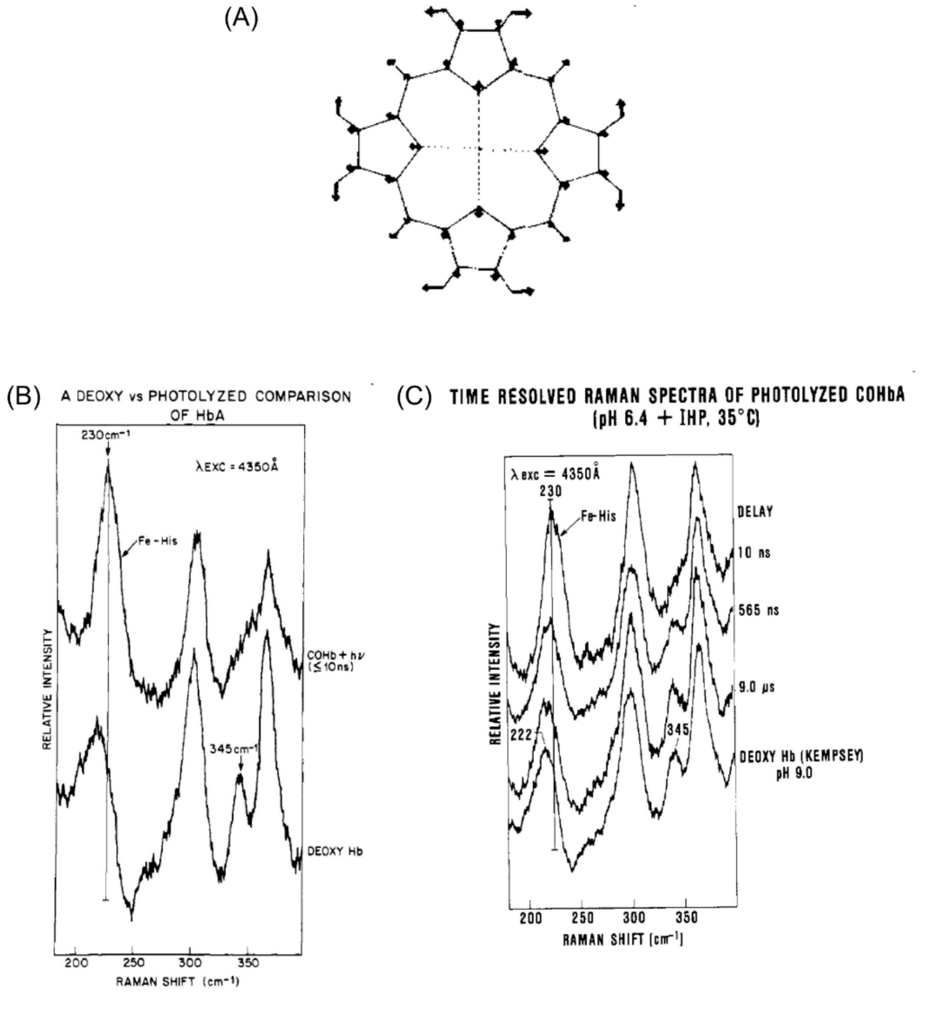

Figure 1-9. The ν_8 mode. (A) Vibrational mode[31]. (B) Comparison of ν_8 mode in ≤10 ns photoproduct and deoxy Hb[35]. (C) Temporal evolution of ν_8 band[35].

Since the environments of the heme pocket change during the R to T quaternary transition, the ν_8 mode is a sensitive marker for the quaternary and tertiary structural changes of Hb. After photodissociation of CO, the ν_8 band only appears as a shoulder of the $C_\beta C_c C_d$ band in the ≤10 ns spectrum, but is more prominent at 345 cm^{-1} in deoxy Hb (i.e. Figure 1-9B[35]). Time-resolved resonance Raman studies have observed that, after the photolysis of CO, the ν_8 band shifts to lower frequency and increases in intensity (i.e. Figure 1-9C[35]). It is also interesting to see that, as shown in Figure 1-9C, the intensity increase of the ν_8 band follows approximately the same time evolution as the ν(Fe-His) band. Above all, the ν_8 intensity has been proved to be a structural marker due to its sensitivity to the environments of the heme pocket.

1.3.2.3 ν_4-electron density

The ν_4 band in the 1350-1380 cm^{-1} region is an in-plane symmetric stretching mode of skeletal atoms[31], as shown in Figure 1-10A. This band is sensitive to the porphyrin π-electron density[36], so that is often referred to as the electron density marker. To be specific, the lower the ν_4 frequency is, the higher electron density there is in the π* orbitals of the porphyrin.

For the ligand bound Hb, the π* electron density is depleted, thus the ν_4 frequency is relatively high (1370-1380 cm^{-1})[37].On the contrary, the π* electron density in deoxy Hb is higher, consequently, the ν_4 frequency becomes lower (~1355 cm^{-1}). Therefore, the frequency of ν_4 band is useful to monitoring the state of ligand binding in heme proteins. In addition, time resolved measurements have revealed that the ν_4 frequency is sensitive to both tertiary and quaternary structures of HbA[38], as shown in Figure 1-10B and 1-10C. However, the time evolution of ν_4 frequency has not yet been investigated in detail.

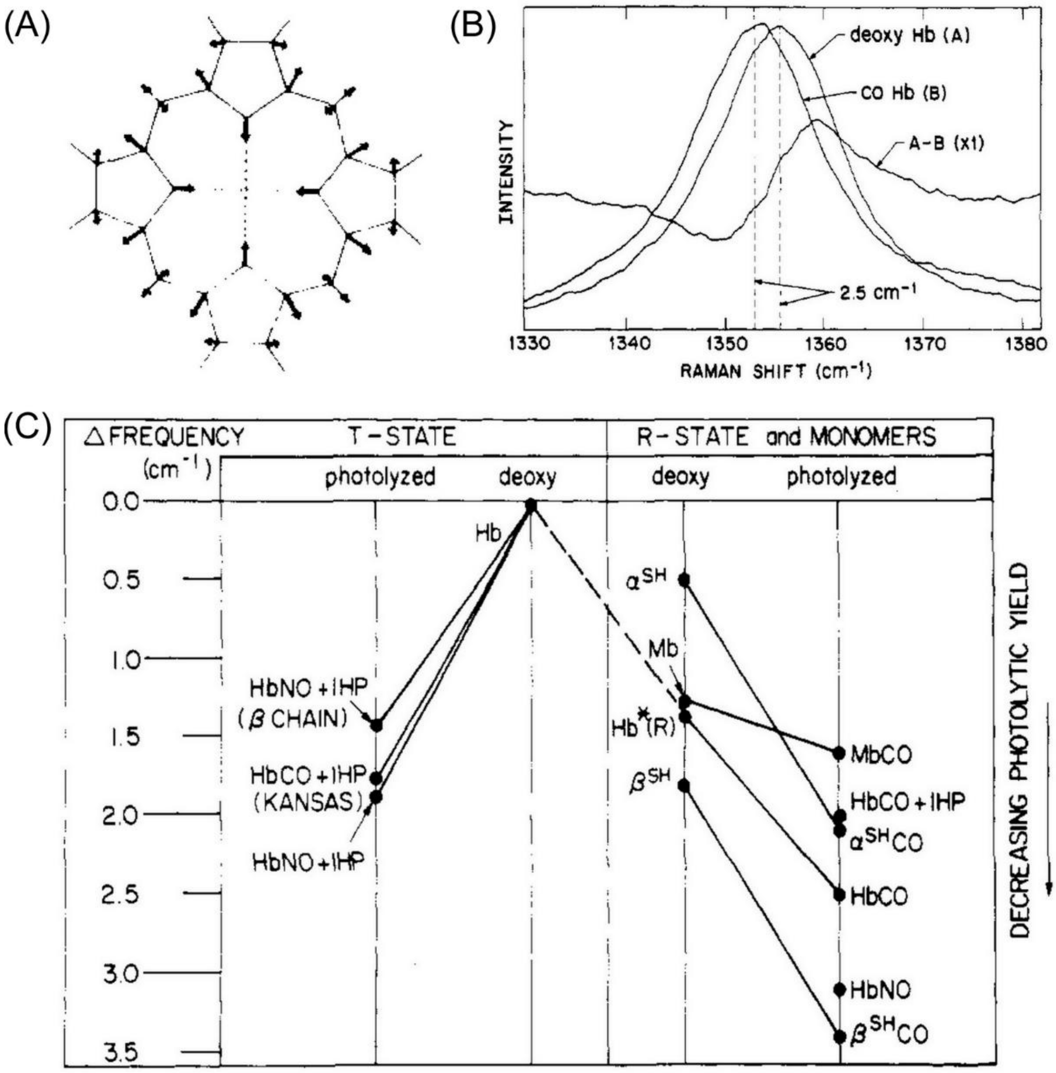

Figure 1-10. ν_4 band. (A) Vibrational mode[31]. (B) The ν_4 frequency shift in going from the 10-ns CO-photolyzed metastable form to the stable deoxy-form for HbA[38]. (C) Frequency changes in $\nu_4$in a variety of stable deoxy and 10-ns CO-photolyzed metastable species[38]. The frequencies are referenced to that of deoxy-Hb (T). Points below the zero indicate lower frequencies.

1.3.2.4 ν_3-core size marker

The porphyrin core of heme is defined as the distance between the four pyrrole nitrogen atoms. Typically, the distance between a pyrrole nitrogen atom and the heme center is used to monitor the core size. It has been proved that the frequency of ν_3 band is sensitive to the core size[39], with a high sensitivity[40] of ~0.002 Å/cm^{-1}. Consequently, small shift in ν_3 frequency predicts important structural information. The upshift of the ν_3 represents the contract of core size, otherwise, the downshift means the core size is expanded.

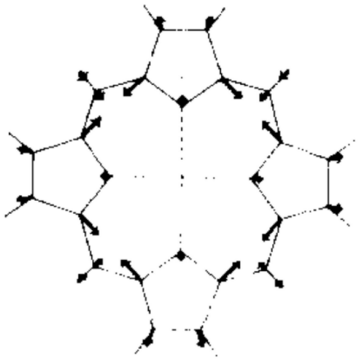

Figure 1-10. Vibrational mode of ν_3 band[31].

References

1. Changeux, J.-P., *Nature Reviews Molecular Cell Biology* **2013,** *14* (12), 819-829.

2. Monod, J.; Wyman, J.; Changeux, J. P., *Journal of Molecular Biology* **1965,** *12* (1), 88-118.

3. Perutz, M. F.; Rossmann, M. G.; Cullis, A. F.; Muirhead, H.; Will, G.; North, A. C. T., *Nature* **1960,** *185* (4711), 416-422.

4. Bolton, W.; Perutz, M. F., *Nature* **1970,** *228* (5271), 551-552; Fermi, G., *Journal of Molecular Biology* **1975,** *97* (2), 237-256; Fermi, G.; Perutz, M. F.; Shaanan, B.; Fourme, R., *Journal of Molecular Biology* **1984,** *175* (2), 159-174; Park, S.-Y.; Yokoyama, T.; Shibayama, N.; Shiro, Y.; Tame, J. R. H., *Journal of Molecular Biology* **2006,** *360* (3), 690-701.

5. Eaton, W. A.; Henry, E. R.; Hofrichter, J.; Mozzarelli, A., *Nature Structural Biology* **1999,** *6* (4), 351-358.

6. Baldwin, J.; Chothia, C., *Journal of Molecular Biology* **1979,** *129* (2), 175-220.

7. Hofrichter, J.; Sommer, J. H.; Henry, E. R.; Eaton, W. A., *Proceedings of the National Academy of Sciences of the United States of America-Biological Sciences* **1983,** *80* (8), 2235-2239.

8. Balakrishnan, G.; Case, M. A.; Pevsner, A.; Zhao, X. J.; Tengroth, C.; McLendon, G. L.; Spiro, T. G., *Journal of Molecular Biology* **2004,** *340* (4), 843-856.

9. Cammarata, M.; Levantino, M.; Wulff, M.; Cupane, A., *Journal of Molecular Biology* **2010,** *400* (5), 951-962.

10. Cammarata, M.; Levantino, M.; Schotte, F.; Anfinrud, P. A.; Ewald, F.; Choi, J.; Cupane, A.; Wulff, M.; Ihee, H., *Nature Methods* **2008,** *5* (10), 881-886.

11. Fischer, S.; Olsen, K. W.; Nam, K.; Karplus, M., *Proceedings of the National Academy of Sciences* **2011,** *108* (14), 5608-5613.

12. Balakrishnan, G.; Tsai, C. H.; Wu, Q.; Case, M. A.; Pevsner, A.; McLendon, G. L.; Ho, C.; Spiro, T. G., *Journal of Molecular Biology* **2004,** *340* (4), 857-868.

13. Jones, E. M.; Balakrishnan, G.; Spiro, T. G., *Journal of the American Chemical Society* **2012,** *134* (7), 3461-3471.

14. Thom, C. S.; Dickson, C. F.; Gell, D. A.; Weiss, M. J., *Cold Spring Harbor Perspectives in Medicine* **2013,** *3* (3).

15. Reed, C. S.; Hampson, R.; Gordon, S.; Jones, R. T.; Novy, M. J.; Brimhall, B.; Edwards, M. J.; Koler, R. D., *Blood* **1968,** *31* (5), 623-632.

16. Lindstro.Tr; Baldassa.Jj; Bunn, H. F.; Ho, C., *Biochemistry* **1973,** *12* (21), 4212-4217.

17. Bunn, H. F.; Wohl, R. C.; Bradley, T. B.; Cooley, M.; Gibson, Q. H., *Journal of Biological Chemistry* **1974,** *249* (23), 7402-7409.

18. Reissmann, K.; Ruth, W. E.; Nomura, T., *Journal of Clinical Investigation* **1961,** *40* (10), 1826-1833.

19. Bonavent.J; Riggs, A., *Journal of Biological Chemistry* **1968,** *243* (5), 980-991.

20. Anderson, L., *Journal of Molecular Biology* **1975,** *94* (1), 33-49.

21. Ogawa, S.; Shulman, R. G.; Mayer, A., *Biochemical and Biophysical Research Communications* **1972,** *49* (6), 1485-1491.

22. Kincaid, J.; Stein, P.; Spiro, T. G., *Proceedings of the National Academy of Sciences of the United States of America* **1979,** *76* (2), 549-552; Kitagawa, T.; Nagai, K.; Tsubaki, M., *Febs Letters* **1979,** *104* (2), 376-378; Argade, P. V.; Sassaroli, M.; Rousseau, D. L.; Inubushi, T.; Ikedasaito, M.; Lapidot, A., *Journal of the American Chemical Society* **1984,** *106* (22), 6593-6596.

23. Perutz, M. F., *Nature* **1972,** *237* (5357), 495-499; Gelin, B. R.; Lee, A. W. M.; Karplus, M., *Journal of Molecular Biology* **1983,** *171* (4), 489-559.

24. Bangcharoenpaurpong, O.; Schomacker, K. T.; Champion, P. M., *Journal of the American Chemical Society* **1984,** *106* (19), 5688-5698.

25. Matsukawa, S.; Mawatari, K.; Yoneyama, Y.; Kitagawa, T., *Journal of the American Chemical Society* **1985,** *107* (5), 1108-1113.

26. Nagai, K.; Kitagawa, T., *Proceedings of the National Academy of Sciences of the United States of America-Biological Sciences* **1980,** *77* (4), 2033-2037.

27. Walters, M. A.; Spiro, T. G., *Biochemistry* **1982,** *21* (26), 6989-6995.

28. Nagai, K.; Kitagawa, T.; Morimoto, H., *Journal of Molecular Biology* **1980,** *136* (3), 271-289.

29. Ondrias, M. R.; Rousseau, D. L.; Shelnutt, J. A.; Simon, S. R., *Biochemistry* **1982,** *21* (14), 3428-3437.

30. Jayaraman, V.; Rodgers, K. R.; Mukerji, I.; Spiro, T. G., *Science* **1995,** *269* (5232), 1843-1848.

31. Abe, M.; Kitagawa, T.; Kyogoku, Y., *Journal of Chemical Physics* **1978,** *69* (10), 4526-4534.

32. Peterson, E. S.; Friedman, J. M.; Chien, E. Y. T.; Sligar, S. G., *Biochemistry* **1998,** *37* (35), 12301-12319.

33. Scott, T. W.; Friedman, J. M.; Macdonald, V. W., *Journal of the American Chemical Society* **1985,** *107* (12), 3702-3705.

34. Carson, S. D.; Wells, C. A.; Findsen, E. W.; Friedman, J. M.; Ondrias, M. R., *Journal of Biological Chemistry* **1987,** *262* (7), 3044-3051.

35. Findsen, E. W.; Friedman, J. M.; Ondrias, M. R.; Simon, S. R., *Science* **1985,** *229* (4714), 661-665; Scott, T. W.; Friedman, J. M., *Journal of the American Chemical Society* **1984,** *106* (19), 5677-5687.

36. Spiro, T. G.; Burke, J. M., *Journal of the American Chemical Society* **1976,** *98* (18), 5482-5489.

37. Kitagawa, T.; Abe, M.; Kyogoku, Y.; Ogoshi, H.; Sugimoto, H.; Yoshida, Z., *Chemical Physics Letters* **1977,** *48* (1), 55-58.

38. Friedman, J. M.; Stepnoski, R. A.; Stavola, M.; Ondrias, M. R.; Cone, R. L., *Biochemistry* **1982,** *21* (9), 2022-2028.

39. Spiro, T. G.; Stong, J. D.; Stein, P., *Journal of the American Chemical Society* **1979,** *101* (10), 2648-2655; Choi, S.; Spiro, T. G.; Langry, K. C.; Smith, K. M.; Budd, D. L.; Lamar, G. N., *Journal of the American Chemical Society* **1982,** *104* (16), 4345-4351.

40. Spaulding, L. D.; Chang, C. C.; Yu, N. T.; Felton, R. H., *Journal of the American Chemical Society* **1975,** *97* (9), 2517-2525.

Chapter 2 Experimental Methods

2.1 Site-directed mutagenesis

Site-directed mutagenesis was performed using the PrimerSTAR MAX DNA polymerase according to the manufacturer's instructions. Mutated plasmids were constructed from the pHE7 expression plasmid, which was kindly provided by Prof. Chien Ho of Carnegie Mellon University[1]. The schematic map of the pHE7 expression plasmid is shown in Figure 2-1. In this plasmid, cDNA α- and β-globin genes and the *E. coli* methionine aminopeptidase (Met-AP) gene are coexpressed under the control of separate *tac* promoters, which are inducible by lactose and analogs such as isopropyl β-D-thiogalactoside (IPTG). In addition, it also contains an ampicillin resistance gene (Amp^R), allowing for selection against any bacteria not carrying the plasmid.

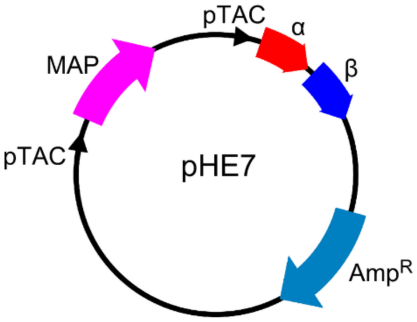

Figure 2-1 Schematic map of the pHE7 expression plasmid.

2.1.1 Design of mutagenic primers

The sequence of β-globin cDNA was downloaded from the NCBI databases (http://www.ncbi.nlm.nih.gov/), the gene ID of which is 3043. In the sequence, the first triplet code are the start codon, so that the 298th to 300th nucleotides encode the 99th residue (βD99), and the 307th to 309th nucleotides encode the 102nd residue (βN102), as shown in Figure 2-3.

For R mutant (i.e. Hb Kempsey), the 298th to 300th nucleotides were designed to change from "GAT" to "AAT", as a result, the 99th residue of β-globin could be mutated from aspartate (D) to asparagine (N). Similarly, for T mutant (i.e. Hb Kansas), the 307th to 309th nucleotides were designed to vary from “AAC” to “ACC” to realize the βN102→T mutation, that is, from asparagine to threonine. Table 2-1 shows the sequences of mutagenic primers.

Table 2-1. Sequences of mutagenic primers.

Purpose of mutation	Type of primer	Sequence of primer
R mutant (βD99→N)	Forward	5’-CACGTGAAT[a]CCTGAGAACTTCAGGCTC-3’
	Reverse	5’-CTCAGGATTCACGTGCAGCTTGTCACA-3’
T mutant (βN102→T)	Forward	5’-CCTGAGACCTTCAGGCTCCTGGGCAAC-3’
	Reverse	5’-CCTGAAGGTCTCAGGATCCACGTGCAG-3’

[a] The underlined sequences are mutated sites.

2.1.2 Preparation of PCR reaction mixture

The DNA polymerase solution purchased from Takara Bio Inc. (PrimeSTAR MAX DNA Polymerase Premix) was used. In this solution, DNA polymerase has already been premixed with reaction buffer and dNTP mixture. Thus, only DNA template and primers are additionally needed to prepare the PCR reaction mixture. In this study, the pHE7 plasmid was used as a template.

Table 2-2 shows the composition of the PCR reaction mixture used in this study. A negative control was also carried out to confirm the validity of the mutagenesis. The preparations were conducted at room temperature, however, all the reaction components were kept on ice.

Table 2-2. Composition of PCR reaction mixture.

Component	Mutagenesis / μL	Control / μL
DNA polymerase solution	25	25
Template (1000-fold dilution)	1	1
Forward primer (10 pmol·μL^{-1})	1	0
Backward primer (10 pmol·μL^{-1})	1	0
Distilled water	22	24
Total	50	50

2.1.3 PCR cycles

The 2720 thermal cycler produced by Applied Biosystems was employed to perform the PCR cycles, the conditions of which are shown as follows:

Denaturing at 98 °C for 10 s→ Annealing at 55 °C for 15 s → Extension at 72 °C for 34 s

30 cycles

Since the extension time is 5 seconds per kb of plasmid, the 6.83 kb[1] pHE7 plasmid needs 34 s to complete the extension step.

After that, the PCR products were transformed into the JM109 competent cells to check whether the plasmids were amplified using these primers (please see Section 2.2.1 for methods of transformation). Results of the transformation suggested that (Figure 2-2) the plasmids were successfully amplified.

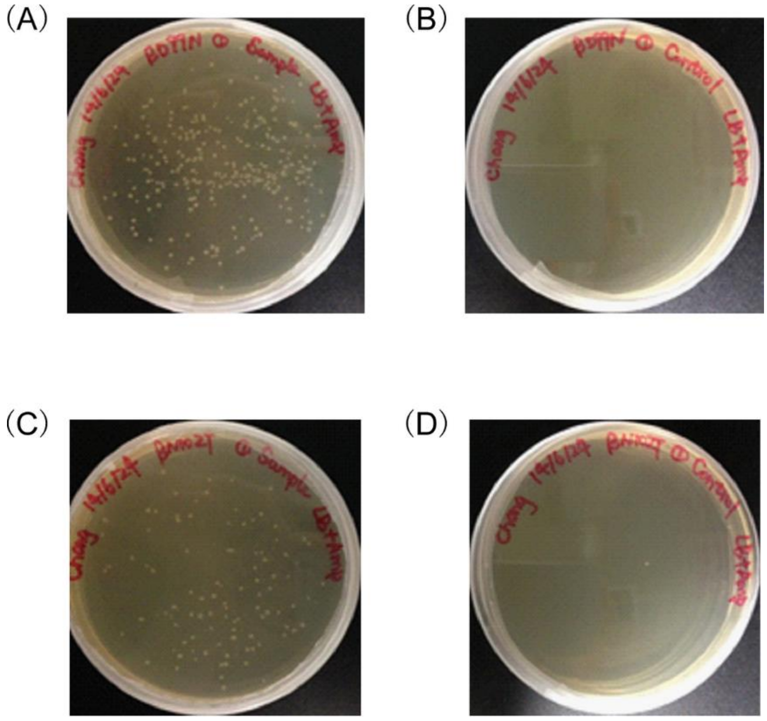

Figure 2-2. Results of transformation of the PCR products. (A) and (C) are the results of mutated plasmids which can express R and T mutants, respectively. (B) and (D) are negative controls of (A) and (C), respectively.

2.1.4 DNA sequencing

Results of DNA sequencing (by Operon) confirmed that the desired mutations were correctly introduced into the pHE7 plasmid, as seen in Figure 2-3.

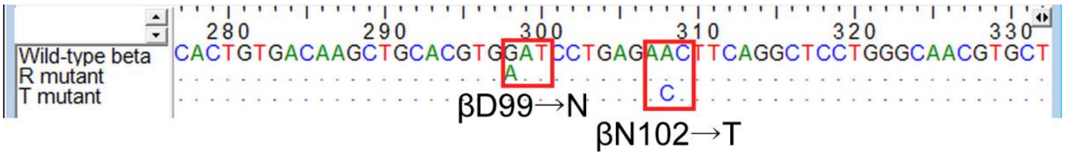

```
                 280       290       300       310       320       330
Wild-type beta   CACTGTGACAAGCTGCACGTGGATCCTGAGAACTTCAGGCTCCTGGGCAACGTGCT
R mutant         .....................A..................................
T mutant         ...............................C........................
```

Figure 2-3. Results of DNA sequencing. The first row is the sequence of β-globin cDNA. The second row is the sequence of mutated plasmid which expresses R mutant, whereas the third is for mutated plasmid expressing T mutant. Dots in the second and third rows represent the same sequences as in the first row.

2.2 Preparation of normal rHb, R mutant, and T mutant

The normal rHb (it was termed as normal recombinant Hb (rHb) in Chapter 3 and wild-type rHb in Chapter 4) was expressed from the pHE7 expression plasmid. Mutated plasmid, which expressed R or T mutant (Chapter 4), was constructed from the pHE7 expression plasmid. Therefore, same method was employed for preparing normal rHb, R mutant, and T mutant.

2.2.1 Transformation

The plasmid was transformed into *E. coli* JM109 competent cells using the heat-shock method. There were three steps, as shown below: (1) 1 μL plasmid was added into a tube of competent cells and mixed by vortexing (Scientific Industries, VORTEX-GENIE2) for 1 s. (2) The competent cell/DNA mixture was incubated on ice for 5 min and at 42℃ for 45 s. (3) The transformed *E. coli* cells were spread on LB agar plate containing 50 mg/L ampicillin (Amp), then the plates were incubated at 37℃ overnight.

2.2.2 Protein expression

In this section, *E. coli* cells were grown in TB medium supplemented with ampicillin at 100 mg/L, which is referred to as TB+Amp medium. For pre-culture, *E. coli* colonies from the LB+Amp plate were inoculated into 50 mL LB+Amp medium in 500 mL Erlenmeyer flask. The culture was incubated with shaking at 37℃ (TAITEC, Bioshaker BR-22FH) until $OD_{600} \approx 1.2$ (GE Healthcare, Gene Quant 100). In general, it takes ~5 hours.

Then, 20 mL pre-culture was used to inoculate the 2 L TB+Amp medium in 5 L Erlenmeyer flask. The 2 L culture was incubated with shaking at 30℃ overnight. By the way, if baffled flask was used, the shaking speed was 80-90 rpm; otherwise, the shaking speed was 180-200 rpm. In the morning of the second day, the OD_{600} was 7-10. At that time, protein production was induced by addition of IPTG to a final concentration of 0.2 mM. As Ho suggested in personal communications, the temperature of the *E. coli* culture was increased to 32℃ after induction, in order to obtain higher yields of rHb and better processing of the N-terminal methionine. The culture was then supplemented with 20 mg/L hemin and 10g/L glucose, and the growth was continued for more than 4 hours. Cells were harvested by centrifugation at 8000 rpm for 10 min at 4℃ (HITACHI, himac CR20GII) and stored at -80℃. Typically, ~12 g *E. coli* pellet can be harvested from 2 L TB culture. Figure 2-4 are examples of *E. coli* pellets, the red color implies that rHb was successfully expressed. The black color of the pellets was due to the excess hemin.

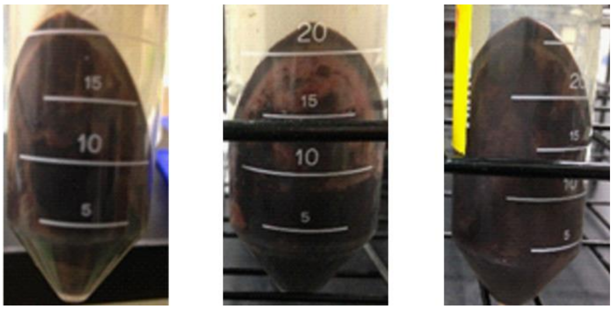

Figure 2-4 Example of the harvested *E. coli* pellets. (Left) Normal rHb (*i.e.* wild-type rHb). (Middle) R mutant. (Right) T mutant.

2.2.3 Protein purification

Cells were lysed by sonication and protein sample was purified primarily according to the method of Looker *et al*[2] with some modifications[1]. The purification was performed at 4-10℃ and near pH 8 in order to minimize autoxidation.

(1) Preparation of cell lysate

The -80℃ *E. coli* pellet was thawed on ice, and then resuspended by vortexing in 3 mL/g cells of CO-saturated buffer, 40 mM Tris-HCl, 1 mM Benzamidine, 1 g/L Lysozyme, pH 8.0. The cell suspension was lysed on ice by sonication for 8×60 sec, using an ultrasonic homogenizer (VP-30S, TAITEC) at output level 6-7. It is extremely important to guarantee that there is enough interval between two times of sonication, in order to keep the temperature below 10℃ and to avoid denaturing the protein samples. After sonication, the cell lysate was saturated with CO and then centrifuged at 4℃ for 45 min at 14000 rpm. The protein-sample-containing supernatant was collected.

(2) Lysate clarification

1 M Tris base was used to adjust the lysate to pH 8.0. Then, polyethyleneimine (PEI; 3.6% (v/v) aqueous stock, pH 8.0) was added with stirring to a final concentration of 0.2%. The mixture was incubated at 4℃ for 10 min to precipitate nucleic acids. The PEI-treated lysate was centrifuged at 4℃ for 45 min at 14000 rpm. The supernatant was recovered. In order to prepare for loading into the first column, the supernatant was dialyzed against the equilibration buffer of Column Q1.

(3) Chromatographic purification step

Three chromatographic steps were employed. The example given is for the purification of R mutant (Sep. 2014). The following steps were carried out at 4℃ or on ice.

Column Q1

The first column was the Q-Sepharose anion exchange column (GE Healthcare, HiTrap^{TM} Q HP), which was equilibrated with 20 mM Tris-HCl/0.1 mM triethylenetetraamine hydrochloride (TETA), pH 7.4. At this pH, a large amount of the unwanted bacterial proteins and nucleic acids were captured while rHb passed through.

Figure 2-5 compares the absorption spectrum of the lysate loading into the column Q1 with that of the eluate. The 413.5/418 nm bands were the Soret bands of heme. Based on their absorbance, it was estimated that most (over 75%) of the rHb passed through the column Q1. The bands near 260 nm were mainly contributed by nucleic acids, which would be removed in the next step.

To prepare for loading into the second column, the rHb-containing eluate of Q1 was adjusted to pH 8.3 with 1 M Tris base.

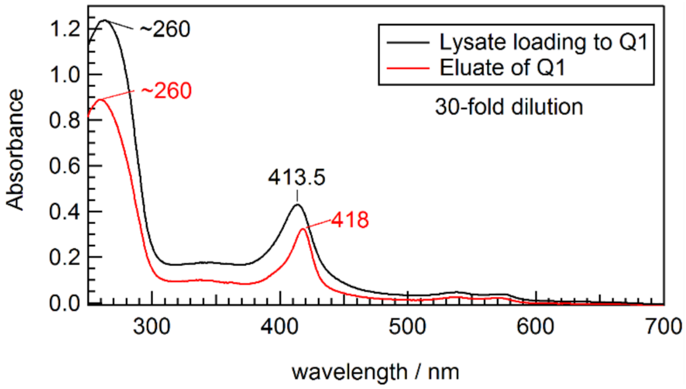

Figure 2-5 Absorption spectra of the lysate loading to Q1 (black) and eluate of Q1 (red).

Column Q2

The second column was the same as the first one, but was run at different pH conditions. The column was equilibrated with 20 mM Tris-HCl/0.2 mM TETA at pH 8.3 to capture rHb. After loading the rHb-containing fraction, the column was washed with equilibration buffer and the pass-through was monitored at 260 nm until the contaminating nucleic acids had eluted. Figure 2-6 shows the variation in absorption spectrum of the pass-through during washing. At last, the value of absorbance at 260 nm was no more than 0.1.

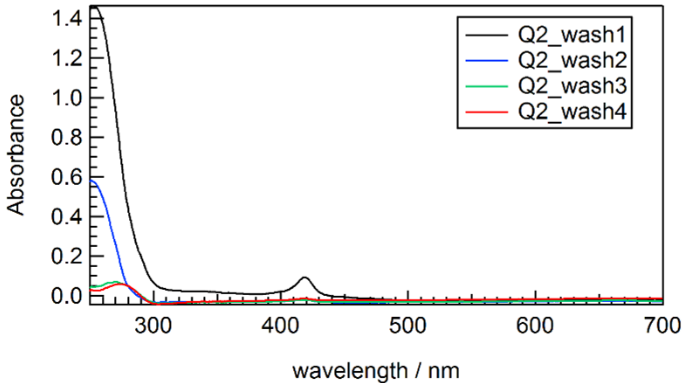

Figure 2-6 Absorption spectra of the pass-through during washing of Q2 column.

After washing, the bound rHb was then eluted with 20 mM Tris-HCl/0.2 mM TETA at pH 7.2[1]. Figure 2-7 shows the absorption spectrum of the solution eluted from Q2 column. It was clear that the nucleic acids were almost removed.

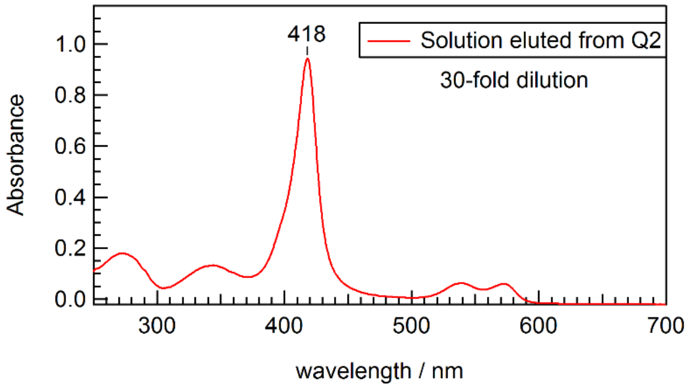

Figure 2-7 Absorption spectrum of the solution eluted from Q2 column.

Column S1

The SP-Sepharose cation exchange column (GE Healthcare, HiTrap^{TM} SP HP) was used for the final purification. The column was equilibrated with Buffer A (10 mM sodium phosphate/0.2 mM EDTA at pH 6.8). After loading and washing, a linear gradient of equilibration buffer versus Buffer B (20 mM sodium phosphate/0.2 mM EDTA at pH 8.3) was used to elute normal rHb (GE Healthcare, ÄKTA pure, at 4℃). The elution diagram was shown in Figure 2-8. The absorption spectra of the 14th-20th fractions were shown in Figure 2-9. Finally, the 17th-18th fractions were collected.

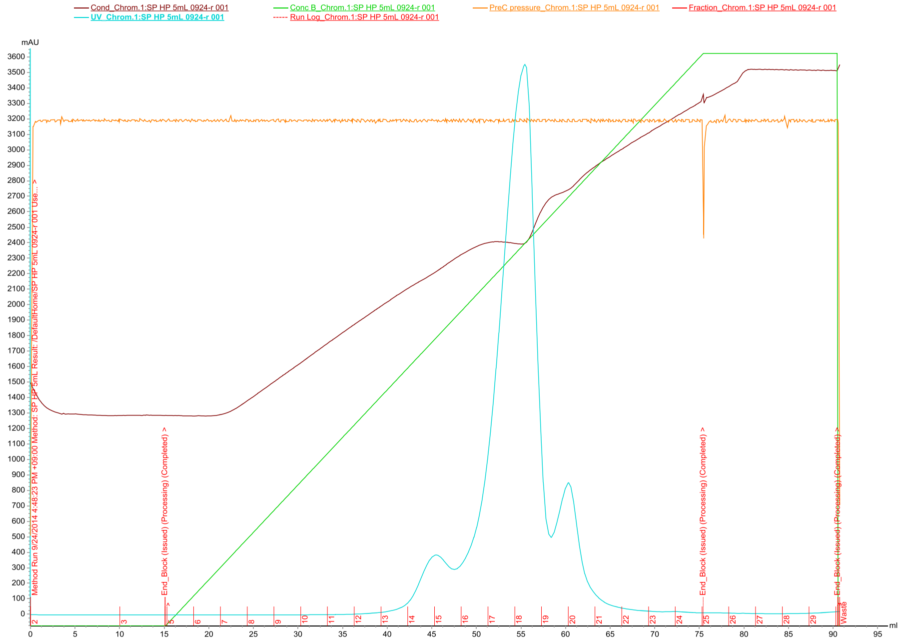

Figure 2-8 Elution diagram of the column S1.

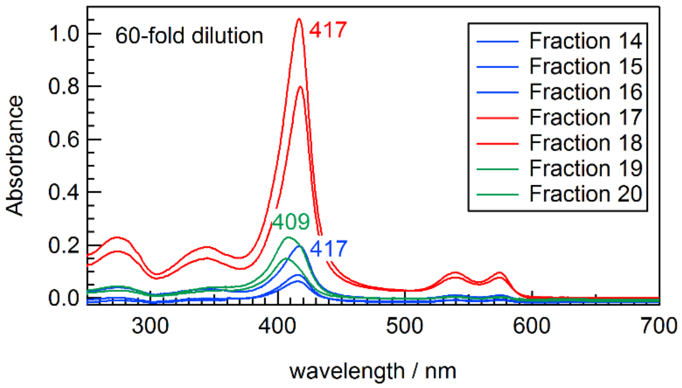

Figure 2-9 Absorption spectra of the 14th-20th fractions in Figure 2-8.

The examples given in Figure 2-8 and 2-9 are just for a single purification (R mutant, purified in Sep. 2014). Figure 2-10 summarizes the elution profiles of normal rHb and two rHb mutants, and makes a comparison with HbA from blood. Normal rHb was eluted at the same position as HbA from blood, whereas the two mutants were eluted later, perhaps because the substitution of amino acid in $\alpha_1\beta_2$ interface may affect the charge distribution of the protein surface. Figure 2-12A is the photo of rHbs after the chromatographic procedures.

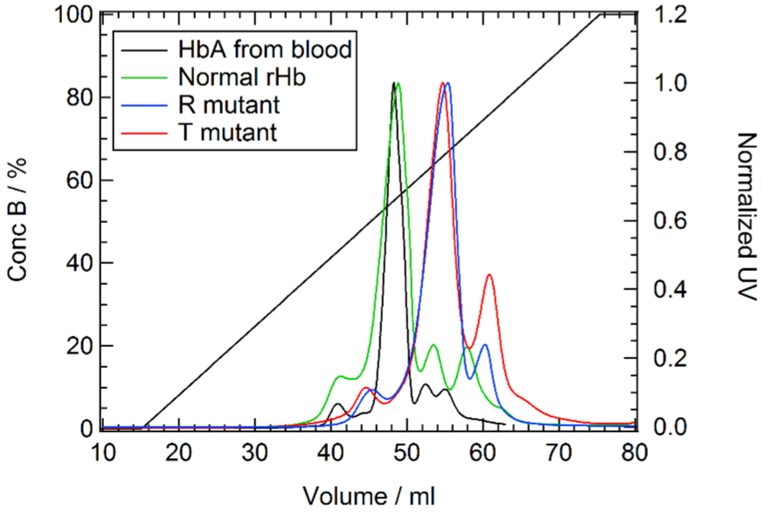

Figure 2-10 Elution diagram of the column S1. The left axis is the percentage of Buffer B, the right axis shows the normalized UV absorbance at 280 nm.

(4) Oxidation-reduction process

After the chromatographic procedures, Prof. Chien Ho[1, 3] reported that a fraction of the heme in rHb was not inserted correctly, and further demonstrated that those incorrectly inserted heme can be converted into the normal conformation by a simple oxidation-reduction process.

It is worthwhile to note that the duration of the oxidation step determines the efficiency of the heme reorientation. Ho[1] stated that at room temperature, 16 hours was enough, but 2 hours was not. Nagai[4] reported that at 4℃, 2 days were necessary to reorient the heme. In the present study, the protein sample was oxidized by a fivefold molar excess of potassium ferricyanide, and then left to stand at 4℃ for 2 days. After that, the sample was reduced to the ferrous state by dithionite and finally converted to the CO or deoxy form.

Time-resolved spectra of normal rHb before (A) and after (B) this oxidation-reduction process in the 280-450 cm^{-1} region were compared in Figure 2-11. In each panel, the spectra of HbA from blood were used as references. Apparently, if this oxidation-reduction process is not carried out, the band shapes of γ_7, ν_8, $\delta(C_\beta C_c C_d)$, and $\delta(C_\beta C_a C_b)$ of normal rHb were slightly distinct from those of HbA from blood (Figure 2-11A). On the contrary, the transient spectra of normal rHb after the oxidation-reduction process perfectly overlapped with the reference spectra (Figure 2-11B). This phenomenon indicates that the oxidation-reduction process is essential for obtaining correct transient spectra in the 280-450 cm^{-1} region.

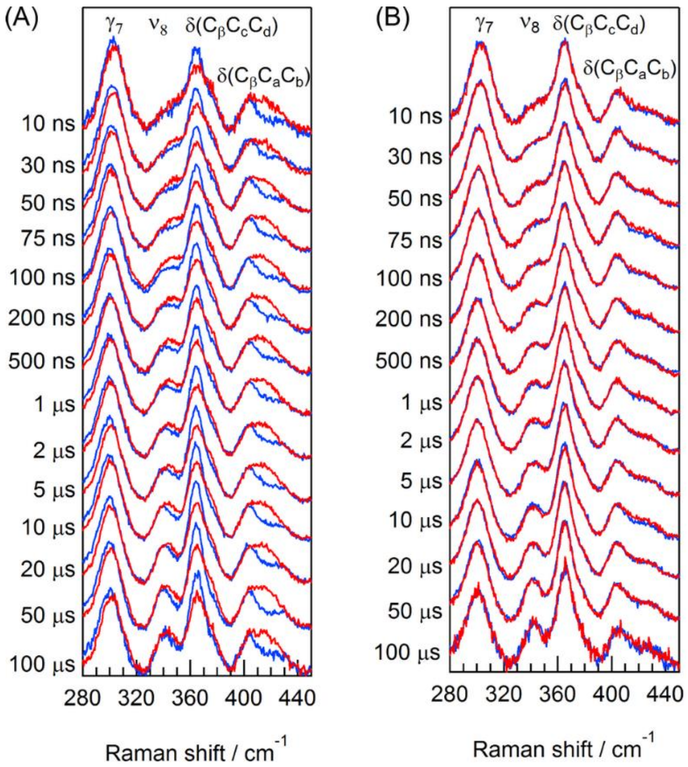

Figure 2-11. Effect of the oxidation-reduction process on the spectral region of 280-450 cm^{-1} of normal rHb. (A) Red spectra: normal rHb before oxidation-reduction process; Blue spectra: HbA from blood. (B) Red spectra: normal rHb after oxidation-reduction process; Blue spectra: HbA from blood. The accumulation time of each spectrum was 18 minutes.

(5) Confirmation of purity

The purity of the each rHb species was confirmed by SDS-PAGE and absorption spectroscopy. The method of SDS-PAGE is described below. Adding SDS and boiling at 99℃ for 5 min made the protein sample denatured. The marker and protein sample were loaded into 15% acrylamide gel. The current was set constant at 20 mA, then the electrophoresis was run for 40-50 min.

Figure 2-12B to D show the result of SDS-PAGE and absorption spectrum (CO-form), suggesting that the purified protein samples were of high purity.

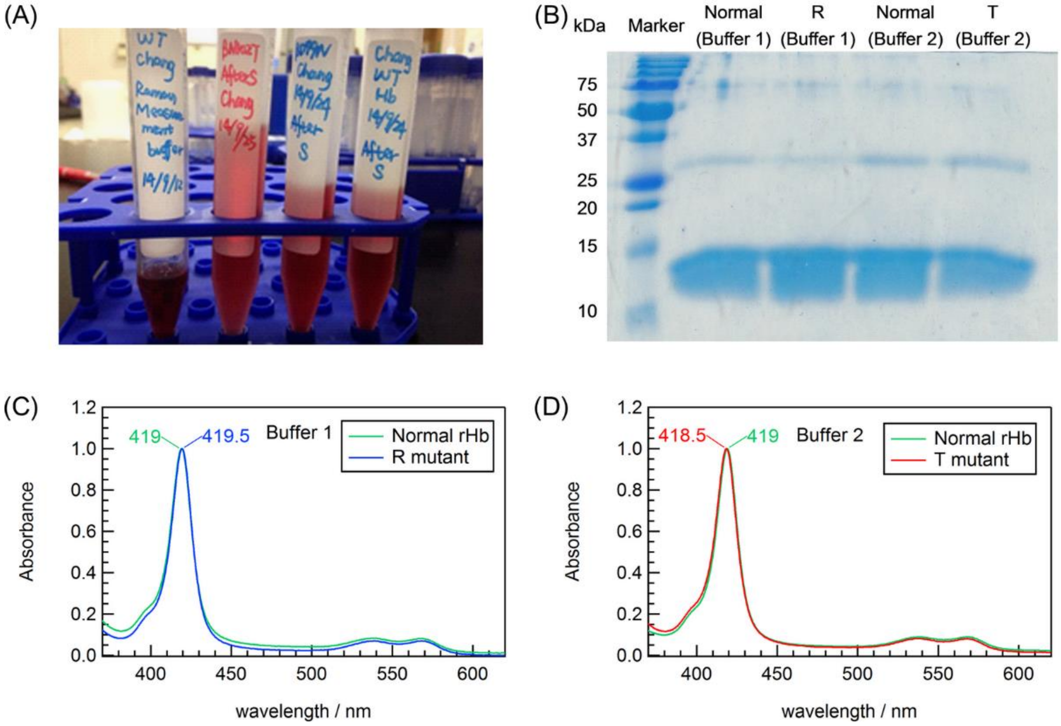

Figure 2-12 (A) is the photo of the purified normal rHb and two rHb mutants. (B) shows the result of SDS-PAGE. (C) and (D) are absorption spectra (CO form) of rHbs. In this figure, Buffer 1 represents 50 mM sodium phosphate buffer, pH 8.0; while Buffer 2 corresponds to 50 mM HEPES buffer, pH 6.4.

2.3 Preparation of α(V1M)/β(V1M) double mutant

The α(V1M)/β(V1M) double mutant was expressed from the pSGE1702 expression plasmid, which was provided by Prof. John S. Olson of Rice University. Figure 2-13 is the schematic map of the pSGE1702 plasmid. This plasmid contains one copy each of the α- and β-globin genes, in which the valine (V) residues at the N-termini were substituted by methionine (M). In addition, it also contains a tetracycline resistance gene (Tet^R), allowing for selection against any bacteria not carrying the plasmid. These genes are positioned under the control of the *tac* promoter, so that their expression is inducible by lactose and analogs such as IPTG.

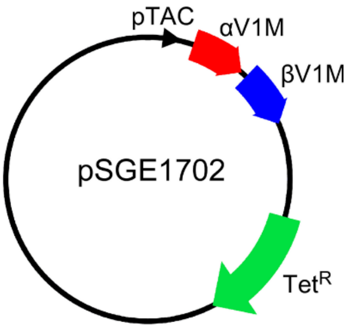

Figure 2-13 Schematic map of the pSGE1702 expression plasmid.

Because the pSGE1702 and pHE7 plasmids were constructed by separate research groups, the transformation, fermentation, and purification procedures were not identical. In the rest of this section, experimental steps, which are distinct from those introduced in Section 2.2, are described in detail. On the contrary, the same steps as shown in Section 2.2 are omitted.

2.3.1 Transformation

The pSGE1702 expression plasmid was transformed into *E. coli* SGE1661 or *E. coli* JM109 competent cells using the heat-shock method. My and Mr. Kurokawa's results showed that the activity of *E. coli* JM109 is much higher than *E. coli* SGE1661. In addition, it takes three days for the transformation using *E. coli* SGE1661, whereas it only takes two days using *E. coli* JM109. Therefore, for efficiency, it is better to use *E. coli* JM109.

Another thing to note is that, since it takes longer time for *E. coli* cells to express tetracycline resistance gene, the transformation method of pSGE1702 plasmid is more complex, as compared with pHE7 plasmid.

In the case of *E. coli* SGE1661, the procedures are as follows:

(1) 1 μL plasmid was added into a tube of competent cells and mixed by vortexing (Scientific Industries, VORTEX-GENIE2) for 1 s. (2) The competent cell/DNA mixture were incubated on ice for 30 min, at 42℃ for 1 min, and then back on ice for 3 min. (3) 900 μL LB media (with no antibiotic) was added into the mixture and then the mixture was incubated at 37℃ overnight shaking at 150 rpm (TAITEC, Bioshaker BR-22FH). (4) The transformed *E. coli* cells were spread on LB agar plate containing 20 mg/L tetracycline (Tet), then the plates were incubated overnight at 37℃.

In the case of *E. coli* JM109, the middle two steps are different as compared with SGE1661:

(2) The competent cell/DNA mixture were incubated on ice for 5 min, at 42℃ for 45 s, and then back on ice for 2 min. (3) 200 μL LB media (with no antibiotic) was added into the mixture and then the mixture was incubated at 37℃ for 30 min shaking at 150 rpm (TAITEC, Bioshaker BR-22FH).

2.3.2 Protein expression

The LB medium used in this section all contained 20 mg/L tetracycline (Tet), thus is referred to as LB+Tet medium. The method of pre-culture is similar as mentioned in Section 2.2.2. Once the OD_{600} reached 1.2, 20 mL pre-culture was used to inoculate the 2 L LB+Tet medium in 5 L Erlenmeyer flask. The 2 L culture was incubated with shaking at 32℃ (New Brunswick Scientific, Innova 43). At $OD_{600} \approx 0.8$, protein production was induced by addition of IPTG to a final concentration of 0.2 mM. Meanwhile, hemin was added to a final concentration of 40 mg/L, and the temperature was decreased to 28 ℃. After that, the culture was incubated with shaking overnight (New Brunswick Scientific, Innova 43). Figure 2-14 is an example of *E. coli* pellets harvested from 4 L LB culture. The color of the pellets should be red. However, there was excess hemin, which was twice as much as that used in Section 2.2.2. Therefore, the color was black.

Figure 2-14 Example of the harvested *E. coli* pellets which expressed the α(V1M)/β(V1M) double mutant.

2.3.3 Protein purification

Protein isolation and purification were carried out according to the protocol provided by Mr. E. Singleton of Rice University[2, 5]. The purification was performed at 4-10℃ and near pH 8 in order to minimize autoxidation.

(1) Preparation of cell lysate

Until sonication, the method is the same as mentioned in Section 2.2.3. After sonication, the cell lysate was saturated with CO and then centrifuged at 4℃ for 60 min at 12000 rpm. The protein-sample-containing supernatant was collected. Since the precipitate contained not only cell debris, but also inclusion bodies, it was resuspended, sonicated, and centrifuged again based on the protocol described above. The supernatant from two times of centrifugation was mixed and ultracentrifuged at 4℃ for 20 min at 35000 rpm (HITACHI, himac CS 150GX II). Finally, the supernatant was saturated with CO and then kept at -4℃ overnight.

(2) Chromatographic purification step

On the second day, Zn acetate was added into the cell lysate (final concentration: 2 mM); the pH was adjusted to 8.0. Afterwards, the lysate was ultracentrifuged at 4℃ for 60 min at 35000 rpm. The supernatant was then filtered through a 0.45 μm PES filter. After all these steps, the cell lysate was loaded on the Zn^{2+}-preloaded Chelating Sepharose Fast Flow (GE Healthcare) column.

The column was washed by sequential passage of Buffer B (20 mM Tris/HCl, 500 mM NaCl, pH 8.5; 3 column volumes (CV)), Buffer C (200 mM Tris/HCl, pH8.5; 2CV), and Buffer D (20 mM Tris/HCl, pH8.5; 3CV). rHb was eluted with Buffer D+15 mM Ethylenediaminetetraacetic acid (EDTA). The eluate was shown in Figure 2-16A.

(3) Oxidation-reduction process

The procedures described above are the same as Mr. Yamada's method. However, subsequently, I added a new step. An additional oxidation-reduction process was carried out on the purified α(V1M)/β(V1M) double mutant, just the same as the oxidation-reduction process purifying normal rHb, in order to make sure that all the hemes were correctly inserted into the globins[1, 3].

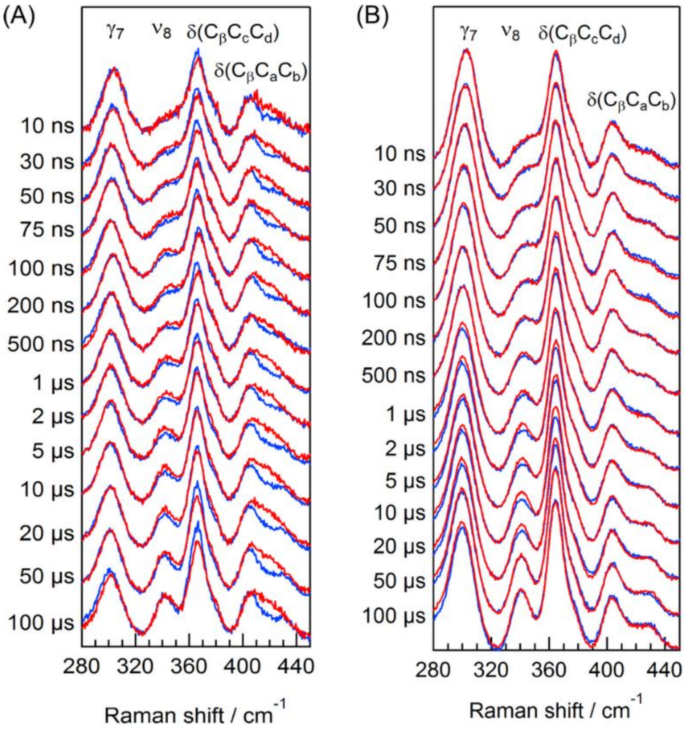

Figure 2-15. Effect of the oxidation-reduction process on the spectral region of 280-450 cm^{-1} of α(V1M)/β(V1M) double mutant. (A) Red spectra: Hb mutant before oxidation-reduction process; Blue spectra: HbA from blood. (B) Red spectra: Hb mutant after oxidation-reduction process; Blue spectra: HbA from blood. The accumulation time of each spectrum in Panel A was 24 minutes, while in Panel B was 60 minutes.

Time-resolved spectra of the α(V1M)/β(V1M) double mutant before (A) and after (B) this oxidation-reduction process in the 280-450 cm^{-1} region were compared in Figure 2-15. In each panel, the spectra of HbA from blood were used as references. The $\delta(C_{\beta}C_{a}C_{b})$ band was obviously affected by the oxidation-reduction process, verifying that not all the hemes were correctly inserted. Therefore, the additional oxidation-reduction process is essential for obtaining correct spectra in the 280-450 cm^{-1} region.

(4) Confirmation of purity

The purity of the purified protein sample was confirmed by SDS-PAGE and absorption spectroscopy. Figure 2-16B and C show the result of SDS-PAGE and absorption spectrum (met-form), respectively. The molecular weight indicated by SDS-PAGE and the position of Soret band in the absorption spectrum all demonstrated that the purified protein sample was high purity rHb.

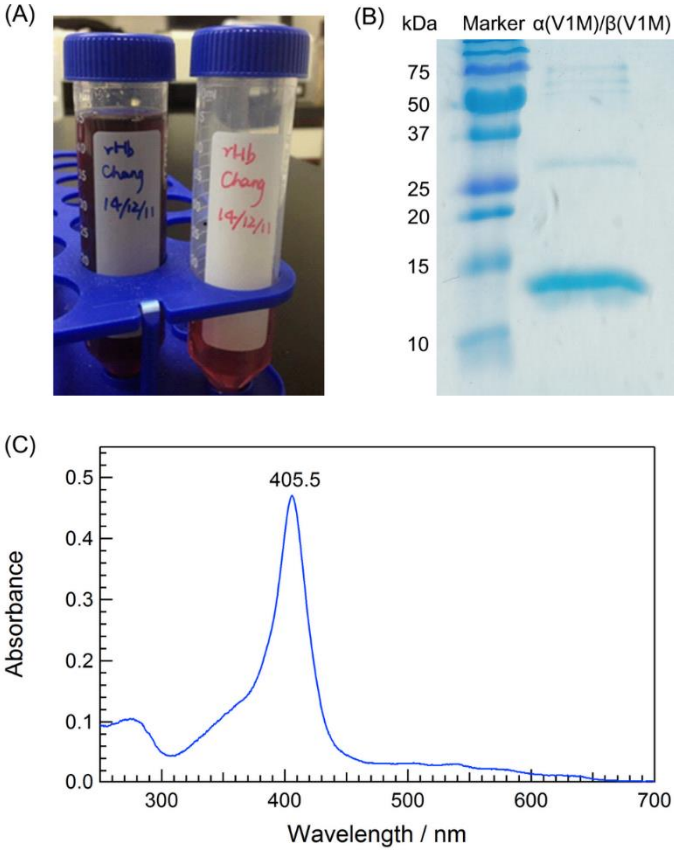

Figure 2-16 (A) The purified α(V1M)/β(V1M) double mutant, before the oxidation-reduction process. (B) Result of SDS-PAGE. (C) Absorption spectrum, met form.

2.4 Measurements of absorption and Raman spectra

2.4.1 Measurement of ultraviolet-visible absorption spectra

Ultraviolet-visible (UV-Vis) absorption spectra were measured using the UV-Visible-NIR spectrophotometer (Shimadzu, UV-3150). Quartz cells with the optical path of 2 mm or 10 mm were used in the measurement. Figure 2-17 is the absorption spectra of normal rHb in three different forms. Peaks of the absorption spectra are contributed by the electronic transitions of the heme group. The peak positions of the Soret band were shown in the figure, which agree with the previous reported values.

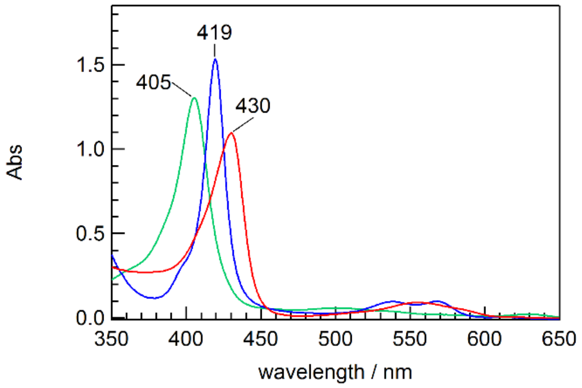

Figure 2-17 UV-Vis absorption spectra of normal rHb.
(Green) Met form (Fe^{3+}); (Blue) CO-bound form (Fe^{2+}); (Red) Deoxy form (Fe^{2+}).

2.4.2 Heme-resonant Raman measurements

Resonance Raman (RR) spectroscopy provides valuable information on the structure of Hb. RR excitation at the wavelengths near the Soret absorption band produce enhanced vibrational bands of the heme chromophore, which are sensitive to both tertiary and quaternary structural changes of Hb. In this study, we investigated the static structures as well as the dynamic behavior of several Hb species, by monitoring the variations in frequency or intensity of some heme-resonant Raman modes.

Heme-resonant Raman spectra of Hbs in CO-form or deoxy-form were detected in the steady-state Raman measurements. The pump-probe time-resolved spectroscopy was applied to monitor the Hb dynamics after the photolysis of CO, as illustrated in Figure 2-18. Hb is initially in CO-bound form (HbCO). The pump pulse photodissociates CO from Hb, and then the probe pulse excites the Raman spectra of Hb intermediates. The photodissociation occurrs so fast that the protein structure is almost unaltered upon that moment (i.e. Hb*≈HbCO). However, Hb* is thermodynamically unstable. It will spontaneously evolve to the thermodynamically stable deoxy structure (deoxyHb) through many intermediates (Hb_1*, Hb_2*, Hb_3*,⋯). By varying the delay time of probe pulse relative to the pump pulse, transient Raman spectra at different delay times (Δt_1, Δt_2, Δt_3,⋯) can be recorded, which characterize the structures of Hb intermediates (Hb_1*, Hb_2*, Hb_3*,⋯).

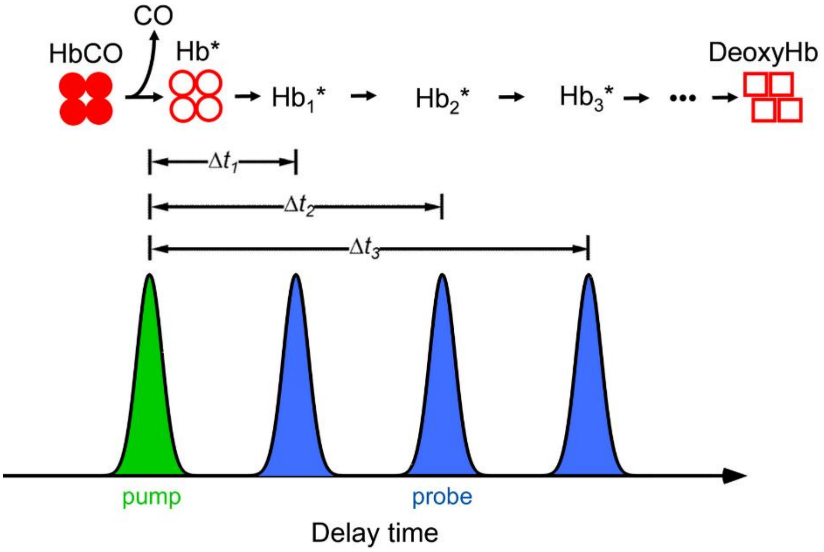

Figure 2-18 Pump-probe time-resolved spectroscopy.

2.4.2.1 Sample preparation

One milliliter 100 μM Hb solution was put into an airtight NMR tube (10 mmΦ), and then two steps were carried out to prepare the static CO-form or deoxy-form Hb. First, the air in the tube and the remaining oxygen in the solution were removed by at least five cycles of degassing and backfilling with CO or N_2. If backfilling with CO, the CO-form Hb was prepared; on the other hand, the deoxy-form Hb was prepared. Second, the samples were reduced with a 10-fold sodium dithionite in a small amount of solution (~10 μL). During the Raman measurements, the Hb sample was replaced with a fresh one every two hours.

2.4.2.2 Apparatus

Figure 2-19 shows the heme-resonant Raman apparatus. Without the pump laser and the delay generator, the apparatus is for measuring steady-state Raman spectra; while with these two devices, it is for the time-resolved measurement.

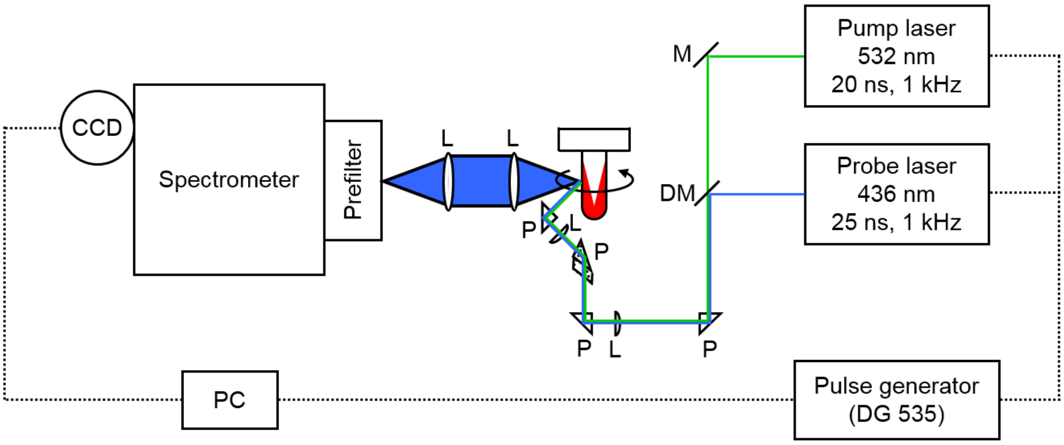

Figure 2-19 Heme-resonant Raman apparatus. Without the pump laser and the delay generator, the apparatus is for measuring steady-state Raman spectra; while with these two devices, it is for the time-resolved measurement. M: mirror; DM: dichroic mirror; P: prism; L: lens.

Since the tertiary and quaternary dynamics of the photodissociated Hb take place in the time region from tenths of nanoseconds to sub-milliseconds[6], nanosecond pulse lasers operating at 1 kHz were employed in this study. The probe pulses at 436 nm, which is close to the Soret band wavelength of deoxy Hb (Figure 2-17), was used to excite the Hb solution, allowing the measurement of heme-resonant Raman spectra. The probe pulses were second harmonics of the output of an Nd:YLF-pumped Ti:sapphire laser (Photonics Industries, TU-L), the power of which was set as low as possible (0.5 μJ/pulse) to avoid photolysis of the ligand by probe pulses. The pump pulses at 532 nm was used to photodissociate CO from Hb, which were generated with a diode-pumped Nd:YAG laser (Megaopto, LR-SHG). The pump power was adjusted to 185 μJ/pulse.

The pump and probe beams were directed collinearly and coaxially using a dichroic mirror, and delivered through several prisms and lenses, eventually focusing onto the sample-containing NMR tube. Figure 2-20 is a schematic diagram showing how pump and probe pulses illuminating onto the sample cell. The time interval between two adjacent pump lasers or two adjacent probe ones was 1 millisecond (since the repetition rate was 1 kHz), which determines that the maxima delay time of probe pulse relative to the pump one cannot exceed 1 ms. Actually, the maxima delay time was only several hundreds of microseconds. The timing between the probe and pump pulses (Δt) was adjusted by a computer-controlled digital pulse generator (Stanford Research System, DG 535) via a GPIB interface, and was accurately checked before each measurement: the probe and pump pulses were detected with a photodiode (Electro-Optics Technology, ET-2000) just before the sample point and monitored with an oscilloscope (Iwatsu, Wavenumber DS-4262).

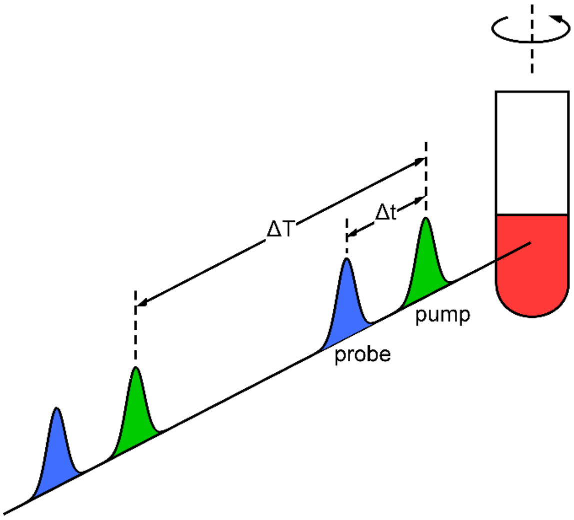

Figure 2-20 Schematic diagram of pump (green) and probe (blue) pulses incidenting onto the sample cell. ΔT: time interval between two adjacent pump or two adjacent probe pulses. Δt: the delay time of probe pulse relative to the pump pulse.

Back to Figure 2-19, the sample-containing NMR tube was continuously spun during the measurement, in order to prevent multiple probing of the same portion of the sample. The spinning cell device was configured of 135° backscattering illumination and collection. The scattered light was collected and collimated by a doublet achromat and focused onto the 200 μm entrance slit of a custom-made prism prefilter (Bunko Kerki) using another doublet achromat. The prism prefilter had a Czerny-Turner configuration, which removed Rayleigh scattering as well as fluorescence.

After that, the scattered light entered the main spectrometer (HORIBA, iHR550), the focal length of which was 550 μm. The main spectrometer was equipped with a blazed-holographic grating (1800 grooves/mm), which is capable of measuring a ~700 cm^{-1}-wide spectrum in the Soret region. However, we are interested in the spectral region from ~200 cm^{-1} (ν(Fe-His)) to ~1600 cm^{-1} (ν_{10}), which is too wide to be recorded all at once. Instead, the whole region was split into two, the “low frequency region” (160-850 cm^{-1}) and the “high frequency region” (1000-1700 cm^{-1}), which were measured separately. A liquid nitrogen-cooled charge-coupled detector (CCD) was attached to the exit of the main spectrometer to detect the Raman scattered light.

2.4.2.3 Strategy of data acquisition

Although enhanced by several orders of magnitude, the heme-resonant Raman signals are still not so strong. As a result, the exposure time of tens of minutes is necessary to accumulate one spectrum. In our time-resolved measurement, we carried out many experimental cycles, and the final transient spectra were averages of the data for these cycles. Our strategy is capable of avoiding random environmental perturbations (thermal drifts of the apparatus, laser fluctuations, etc.), which become evident for hours of measurement.

In the present study, each experimental cycle was composed of one forward and one backward scan. In the forward scan, delay times were altered by increasing them. At each delay time, Raman signals were collected for three 20 s exposures. After that, the pump-only, probe only, and dark measurements for equivalent exposures were also conducted. On the other hand, the procedure of the backward scan was the same, except that the delay times were changed in an opposite direction. To be specific, the sequences of the data acquisition per experimental cycle used here was listed in Table 2-3. In most cases, Cycle A was applied; however, if the maxima delay time was extended to 350 μs, Cycle B was utilized.

Table 2-3. Sequence of the data aquisition per experimental cycle.

Cycle A	Forward	-50 ns→0 ns→10 ns→30 ns→50 ns→75 ns→100 ns→200 ns→500 ns→1 μs→2 μs→5 μs→10 μs→20 μs→50 μs→100 μs→pump-only →probe-only→dark
	Backward	100 μs→50 μs→20 μs→10 μs→5 μs→2 μs→1 μs→500 ns→200 ns →100 ns→75 ns→50 ns→30 ns→10 ns→0 ns→-50 ns→pump-only →probe-only→dark
Cycle B	Forward	-50 ns→100 ns→1 μs→10 μs→100 μs→200 μs→350 μs→ pump-only→probe-only→dark
	Backward	350 μs→200 μs→100 μs→10 μs→1 μs→100 ns→-50 ns→ pump-only→probe-only→dark

2.4.2.4 Data analysis

The raw spectrum observed by the pump-probe time-resolved method contains a small but unneglected contribution from the unphotodissociated species (~15%). There are three reasons. First, it is impossible to photolyze the CO molecules by 100%. Second, some photolyzed CO rebind to the heme. Third, at longer delay times (i.e. 100 μs), the sample cell was spun so fast that the probe and the pump spots only partly overlapped. As a result, a fraction of Hb detected by the probe spot had not been photolyzed at all.

In this study, the proportions of the photolyzed species in the transient spectra was estimated by the ν_4 band, and then the spectra of photolyzed species in the high and low frequency regions were extracted, respectively. It has been established that the ν_4 band is sensitive to the state of ligand binding in Hb. As illustrated in Figure 2-21, in the raw spectrum of normal rHb at 100 ns (b), the ν_4 band had an intense peak at 1354 cm^{-1} and a small shoulder on the higher wavenumber side (1372 cm^{-1}). The intense peak was similar in frequency to the ν_4 band of the deoxy-form (d), so that was attributed to the photolyzed species. On the other hand, the small shoulder coincided in frequency with the ν_4 band of the CO-form (d), thus was contributed by the unphotolyzed species. Subtracting the CO-form spectrum by an appropriate ratio from the raw spectrum, the small shoulder would disappear. Obviously, the ratio used here was just the proportion of unphotolyzed species. Once the proportions of the photolyzed species in the raw spectra were estimated, the spectra of photolyzed species in the high (i.e. Figure 2-21c) and low frequency regions were extracted, respectively.

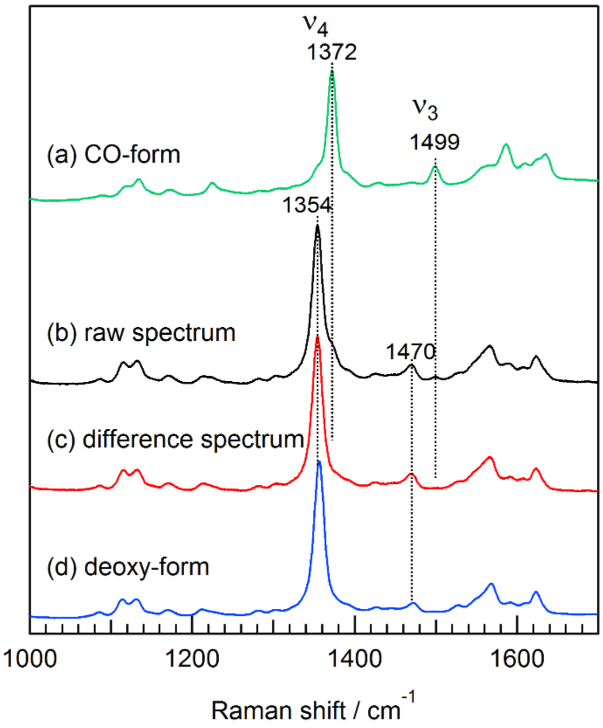

Figure 2-21. The method to determine the proportion of photolyzed species.

There is another method to check whether the proportion of the photolyzed species is appropriated estimated. As shown in Figure 2-21, the region right around 1499 cm^{-1} became flat upon CO photolysis, since the ν_3 band shifted to a lower frequency region by ~30 cm^{-1}.

Therefore, in a correct difference spectrum (c), the region right around 1499 cm^{-1} should be flat, instead of having a small band.

To facilitate the detection of frequency shifts, as well as the relative intensity variations, two subsequent steps were carried out, as describe in Figure 2-22. At first, the baselines of the spectra of the photolyzed species were flattened. After that, the spectra were normalized, so that the ν_7 intensity in the low frequency region, or the ν_4 intensity in the high frequency region, was scaled to unit.

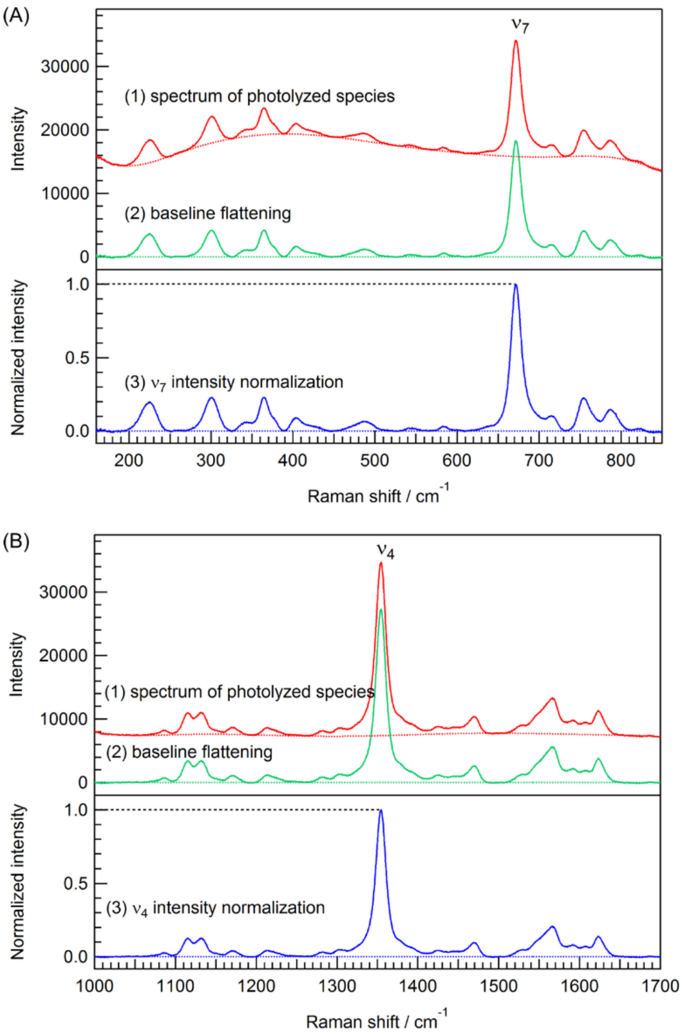

Figure 2-22. Baseline flattening and intensity normalization in the low (A) and high (B) frequency region.

2.5 Determination of small frequency shifts by Raman difference spectroscopy

Previous studies have revealed that the ν_4 frequency is sensitive to both tertiary and quaternary structures of HbA[7], however, the frequency shift of ν_4 band is too small to study accurately utilizing conventional Raman spectroscopy. Raman difference spectroscopy (RDS) is the most accurate method detecting very small wavenumber shifts. In the present study, we apply RDS to study the temporal evolution of ν_4 frequency after the CO photolysis.

2.5.1 Principle of RDS

RDS can be applied to determine small frequency shifts of Raman-active modes, especially when changes in band shapes are negligible[8, 9]. The primary advantage of this method is that the frequency shift can be determined even more accurately (i.e. ±0.01 cm^{-1}) than that of the absolute frequencies (±0.1 cm^{-1})[8].

To illustrate this method, Figure 2-23 gives an example and defines relative parameters. Spectra A and B have identical bands shapes ($I_A=I_B=I_0$, $\Gamma_A=\Gamma_B=\Gamma$), except that their frequencies are separated by Δ. The difference spectrum (B-A) is generated by subtracting spectrum A from spectrum B. In the difference spectrum, the peak-to-peak height of the derivative like curve is defined as d, whereas the frequency separation of these two peaks is denoted as δ.

Laane and Kiefer's theory[8, 9] proved that, d and Δ exhibit a linear dependence when Δ is sufficiently small ($\Delta/\Gamma < 0.2$), regardless of the nature of the band shape. The mathematical expression is,

$$\Delta = Ad\,, \quad \text{when } \Delta/\Gamma < 0.2 \tag{2-1}$$

where A is a constant. Therefore, the linear correlation between d and Δ permits the determination of small frequency shifts (Δ) by measuring the peak-to-peak intensities (d) of the Raman difference spectra.

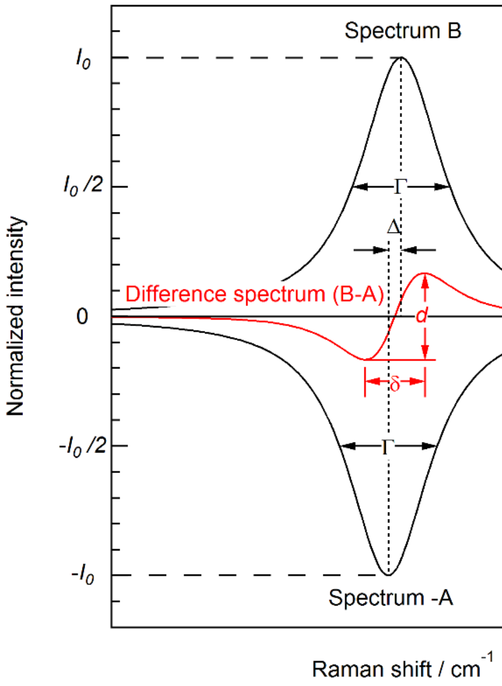

Figure 2-23 Definition of parameters for Raman difference spectroscopy

2.5.1.1 Determination of *A*

There are at least two methods to determine the value of *A*. The value can be either estimated using Laane and Kiefer's method[8, 9], or determined more accurately by simulating difference spectra via the experimental spectrum.

(1) Estimation using Laane and Kiefer's method

Laane and Kiefer developed their method through investigating pure Lorentzian and Gaussian band shapes, and also suggested that the method was applicable to any intermediate band shape. They proved that,

$$\Delta = Ad = \frac{B\Gamma}{I_0} d\,, \quad \text{when } \Delta/\Gamma < 0.2 \qquad (2\text{-}2)$$

where *B* is a constant. The value of *B* is a function of the band shape. For pure Lorentzian bands and pure Gaussian bands, *B* is 0.385 and 0.350, respectively. For intermediate band shapes, the value of *B* depends on the percentages of Lorentzian and Gaussian character. The fraction of Lorentzian character *L* can be estimated by measuring δ/Γ. When $\Delta/\Gamma < 0.2$, δ/Γ is

0.577 for Lorentzian bands and 0.850 for Gaussian bands. Linear extrapolation using these values yields the value of L. Then, B is determined by

$$B = 0.0347L+0.3501 \tag{2-3}$$

Except B, other parameters (Γ and I_0) in Equation 2-3 are experimentally measurable. Consequently, the value of A can be estimated.

(2) Simulation of Raman difference spectra

The basic idea of this method is to slightly shift the experimental Raman spectrum with respect to itself. For every shift Δ, a simulated Raman difference spectra and the intensity of the difference spectrum d are obtained. A standard curve is drawn by plotting the data of Δ versus d, the slope of which is just the value of A.

(3) Comparison of two methods

The first method is very powerful. However, it possesses more theoretical than practical significance. In many practical cases, several broadening effects of the Raman bands may exist, or several Raman bands might overlap with each other, or there might be other practical problems. Under these circumstances, the shape of the Raman band might be irregular, so that the second method is more practical and accurate.

2.5.1.2 Requirements of utilizing RDS

The increase in precision utilizing RDS (i.e. ±0.01 cm^{-1}) requires that certain strict experimental conditions much be satisfied.

Firstly, the two Raman spectra, which are used to calculate the difference spectrum, should “preferably be recorded simultaneously”[8], in order to prevent environmental perturbations. Among various apparatus accomplishing this purpose[10-13], the very simple rotating sample technique introduced (with PM detector)[11] and improved (with CCD detector)[12] by Kiefer is very popular. There is a small drawback of this improved technique[12]: the CCD detector favors more longer exposure time per spectrum, which might cause slight environmental perturbations (thermal drifts of the apparatus, laser fluctuations, etc.)[13].

Secondly, before subtracting two Raman spectra, the peak intensities of corresponding Raman bands must be accurately matched[8].

In practice, the accuracy of RDS also depends on the signal-to-noise (S/N) ratio of the spectrum[13]. The intensity of the difference signal (*d*) is only one or two orders of magnitude lower than the peak intensity of the Raman band, therefore, the accurate measurement of *d* is noise limited.

2.5.2 Application of RDS in this paper

2.5.2.1 Determination of *A*

(1) Estimation using Laane and Kiefer's method

In this part, the transient spectra of wild-type rHb at pH 6.4 was set as an example, as shown in Figure 2-24. The bandwidth of ν_4 (Γ) was 15.5 cm^{-1}. The difference spectrum was calculated by subtracting the 30-ns spectrum from the 100-μs spectrum. The frequency separation of two peaks in the difference spectrum (δ) was 10.2 cm^{-1}. So that, δ/Γ was 0.658. Linear interpolation between the Lorentzian and Gaussian limits yields L=0.703. Therefore, B was calculated to be 0.374 (Eq. 2-3). Finally, the value of A was estimated to be 5.80 (Eq. 2-2).

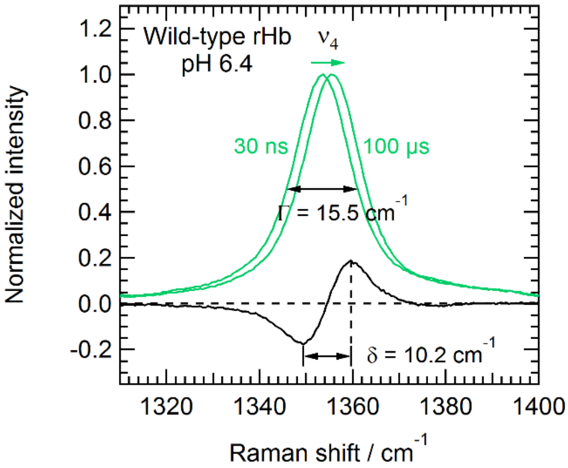

Figure 2-24 Frequency shift of ν_4 band from 30 ns to 100 μs, wild-type rHb, pH 6.4. The green and black curves represent original and difference spectra, respectively.

For other three cases (wild-type rHb and R mutant at pH 8.0, as well as T mutant at pH 6.4), the estimated values of *A* were quite similar. Altogether, the average value of *A* was 5.76.

(2) Simulation of Raman difference spectra

Figure 2-25 illustrated the method to simulate the difference spectra and then to calculate the value of *A*. The experimentally measured 30-ns spectrum of wild-type rHb at pH 6.4 is used as an example. It is important to note that the largest Δ should not exceed 3.1 cm^{-1} in the simulation. As indicated by Laane and Kiefer's theory, Δ and d are linearly correlated only when $\Delta/\Gamma < 0.2$. In our case, Γ is 15.5 cm^{-1} (Figure 2-24), so that, the linear correlation between Δ and d will hold only when Δ is smaller than 3.1 cm^{-1}.

It is better to do linear interpolation first, due to the limited data points of the measured spectrum (Figure 2-25A). Our CCD detector has 1340 pixels, and the frequency difference between two pixels in the measured spectrum was 0.5-0.6 cm^{-1}. Since the largest Δ should not exceed 3.1 cm^{-1}, we can obtain at most 6 simulated difference spectra, indicating that the standard curve contains only 6 points, and that the value of *A* might be determined in low accuracy. The step of linear interpolation can increase the data points of the original spectrum, then generate more data points of the standard curve, and eventually improve the accuracy of *A*. In our case, the 1340 pixels was interpolated to 10,000 points, which were uniformly spaced by 0.072 cm^{-1}.

The interpolated 30-ns spectrum was right-shifted by n points (Δ=0.072n cm^{-1}), yielding a shifted Raman spectrum (Figure 2-25B). The simulated Raman difference spectrum was constructed by subtracting the 30-ns spectrum from the shifted spectrum. Then the value of d was measured. By changing n from 0 to 35, we obtained 36 pairs of data for Δ versus d. Meanwhile, the largest Δ was still lower than 3.1 cm^{-1}, satisfying the requirement of linear correlation. These 36 pairs of data were plotted and fitted by a linear equation, as shown in Figure 2-25C. The fitting was in high quality, as suggested by the value of R^2. The value of *A* equals to the slope of the line, and here, it was 5.67.

Figure 2-25D compared the real difference spectrum (black) with the simulated (red) one. The black curve represents the real difference spectrum by subtracting the 30-ns spectrum from the 100-μs spectrum. *d* of the real difference spectrum was 0.367, then $\Delta = 5.67d = 2.08$ cm^{-1}. If the interpolated 30-ns spectrum was right-shifted by 29 points, the shifted spectrum (red) and the 30-ns spectrum were separated by 2.09 cm^{-1}, which was the closest to 2.08 cm^{-1}. Apparently, the shifted spectrum almost overlapped with the 100-μs one. The simulated difference spectrum was also shown in red, which agrees reasonably well with the real difference spectrum. Therefore, the present method is highly effective to predict the frequency shift Δ.

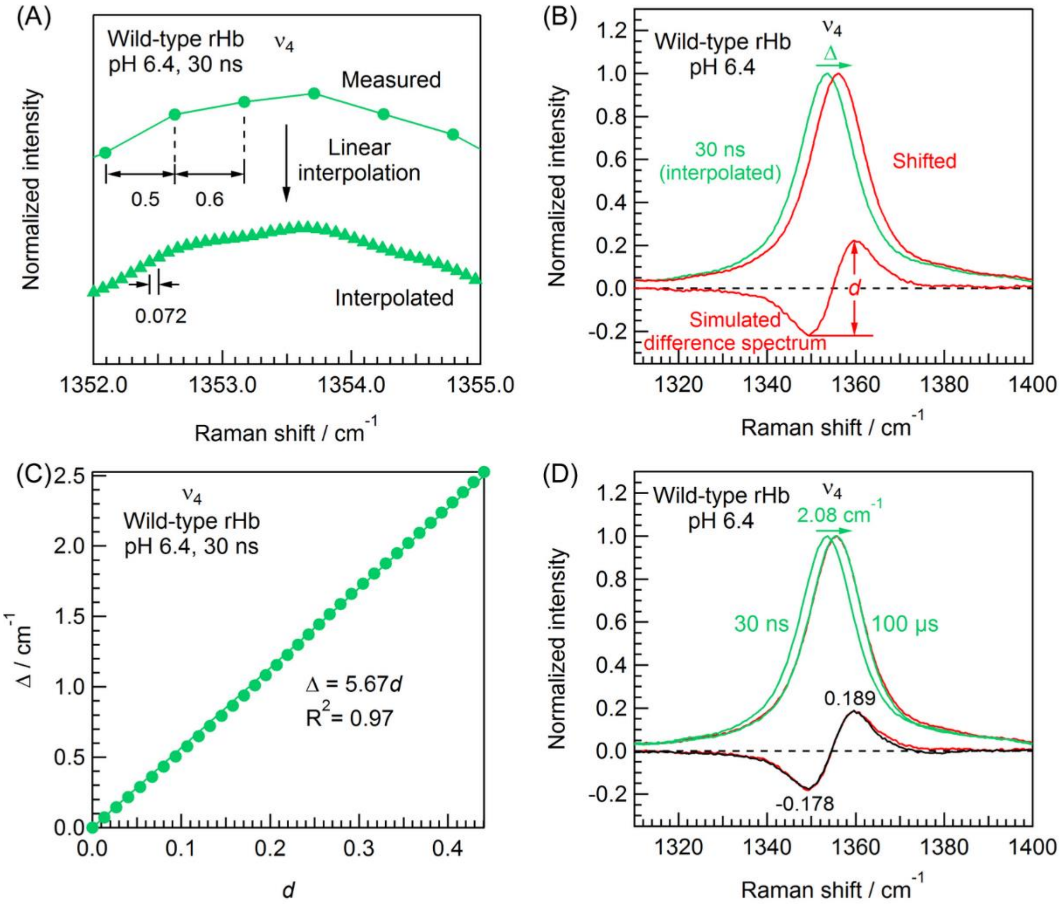

Figure 2-25 Illustration of the method to calculate *A* by simulating Raman difference spectra. (A) Method of linear interpolation; (B) Method to generate the simulated difference spectra; (C) The simulated standard curve of Δ against *d*; (D) Comparison of the real difference spectra (black) with the simulated one (red).

In all, Figure 2-25 introduced the method in detail. We applied this method to different rHb species, at different pH values, and also at two distinct delay times. The calculated values of *A* in all these conditions were quite similar, with an average of 5.64 (Table 2-4).

Table 2-4. Summarization of the values of *A* derived from simulation method.

		30 ns		100 μs		Average
		A	R^2	*A*	R^2	*A*
pH 8.0	R mutant	5.79	0.97	5.58	0.95	5.64
	Wild type	5.65	0.95	5.67	0.97	
pH 6.4	T mutant+IHP	5.67	0.98	5.53	0.96	
	Wild type	5.67	0.97	5.59	0.96	

(3) Comparison of two methods

In summary, *A* was estimated to be 5.76 using the first method, and simulated to be 5.64 by the second. These two values were generally consistent, but we choose to use the latter one in Chapter 4, since the second method is more accurate.

2.5.2.2 Requirements of utilizing RDS

Section 2.5.1.2 described three requirements of utilizing RDS. Here in this part, we checked our time-resolved Raman technique and data analysis method, the results of which demonstrate that our technique and method generally meet all these requirements.

(1) Quasi-simultaneous measurement

Our time-resolved Raman apparatus is, in principle, similar to Kiefer's rotating cell device with CCD detector[12]. Kiefer divided the rotating cell into several compartments in order to compare the spectra of various samples. We also used rotating cell technique, but we did not need a divided cell. Instead, we altered the delay time between pump and probe pulses consecutively, as described in Table 2-3. Our purpose is to compare the spectra of the same sample at distinct delay times.

Similar to Kiefer's technique, our apparatus has the same small drawback: it is impractical to record all the transient spectra exactly simultaneously. If the time elapsing between two adjacent delay times is short enough, the measurement can certainly be regarded as simultaneous. However, we need at least 1 minute to record one meaningful spectrum, due to the very weak Raman signal. In practice, we altered the delay time every 1 minute. The increased time interval between two transient spectra may possibly, at the same time, increase the uncertainty caused by random environmental perturbations.

One possible way to reduce these random perturbations is to conduct multiple experimental cycles. In the present study, for each rHb species, we ran three cycles in one single measurement, and repeatedly carried out three independent measurements. The reproducibility of these independent measurements were carefully checked in two aspects: "ν_4 frequency shift between two delay times" and "ν_4 frequency".

(*i*) The reproducibility of "ν_4 frequency shift between two delay times"

The reproducibility of "ν_4 frequency shift between two delay times" is illustrated in Figure 2-26, using the spectra and data of R mutant at pH 8.0 as examples. The "ν_4 frequency shift" from 30 ns to a given delay time *t* was analyzed using RDS. For each independent measurement, or for the average spectra, the difference spectra at delay time *t* was calculated as:

$$\text{Difference spectrum } (t) = \text{Transient spectrum } (t) - \text{Transient spectrum } (30\text{ ns}) \qquad (2\text{-}4)$$

In Figure 2-26, panels (A) to (C) show the transient difference spectra of three independent measurements, respectively (red, blue, and green curves). In addition, in each panel, although quite inconspicuous, the average spectra of these three measurements (black curves) are also shown behind the colorized spectra. The inconspicuous of the average spectra suggests that the "ν_4 frequency shift between two delay times" can be well reproduced in every independent measurement. Panel (D) quantifies the frequency shifts. The deviations of data between three measurements were very small, with an average of only ~0.02 cm^{-1}, further verifying the high reproducibility of the "ν_4 frequency shift between two delay times".

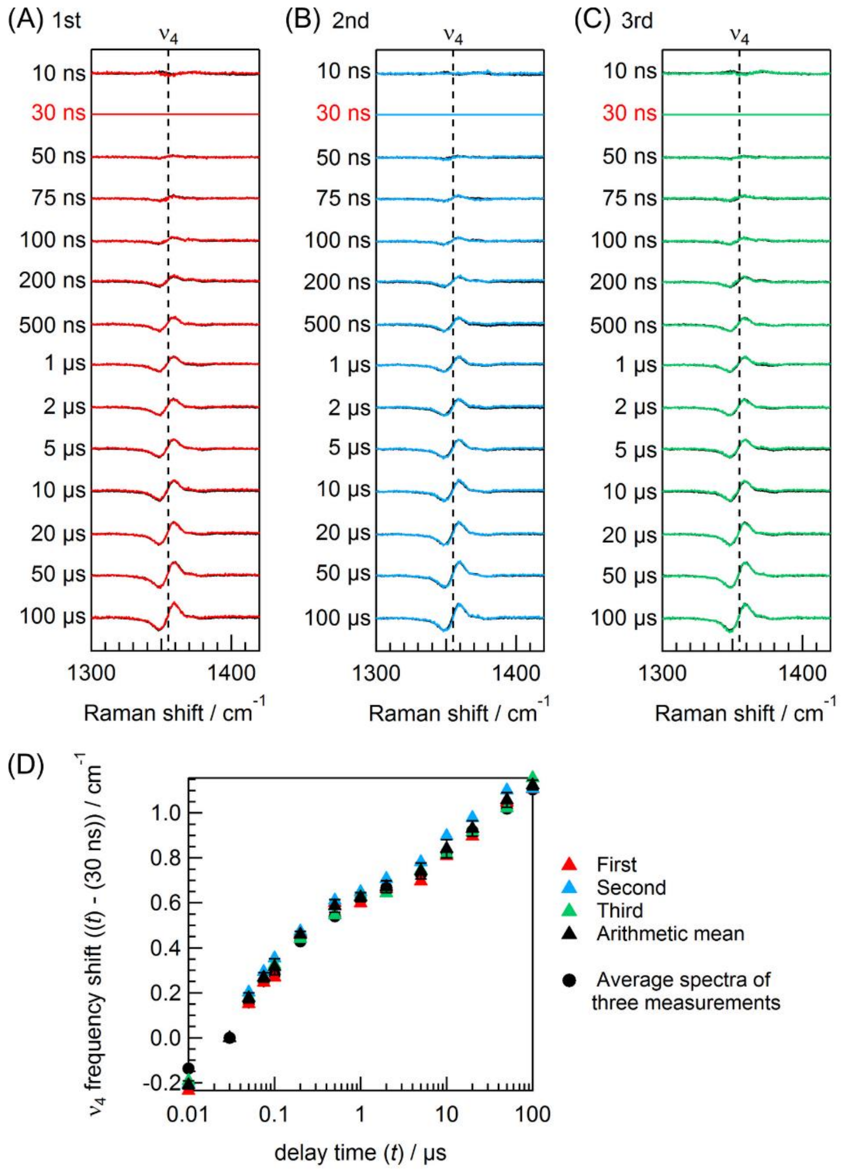

Figure 2-26 Reproducibility of the "ν_4 frequency shift between two delay times", in the case of R mutant at pH 8.0. (A) to (C) are the time-resolved difference RR spectra of ν_4 band: the red, blue, and green curves represent the spectra in the first, second, and third measurement, respectively; meanwhile, the black curves on the background are the average spectra of these measurements. The difference spectrum at delay time *t* was obtained by subtracting the 30-ns spectrum from the spectrum at *t*. (D) shows the time plot of the "ν_4 frequency shift relative to the frequency at 30 ns".

In addition to R mutant at pH 8.0, the reproducibility of the "ν_4 frequency shift between two delay times" had also been examined under other circumstances, i.e., wild-type rHb at pH 8.0 and 6.4, as well as T mutant+IHP at 6.4. To avoid repetition, their data were not shown here, but were summarized in Figure 4-6 of Chapter 4. The very small error bars in Figure 4-6 proved that, despite being influenced by rHb species and pH conditions, the "ν_4 frequency shift between two delay times" is well reproduced in three independent measurements of the same rHb species at the same pH.

(*ii*) The reproducibility of "ν_4 frequency"

Unlike the highly reproduced "ν_4 frequency shift between two delay times", the fluctuations of the "ν_4 frequency" between three independent measurements were much larger. For example, Figure 2-27 reflects the fluctuations of the "ν_4 frequency" in the case of R mutant at pH 8.0. The spectra of independent measurements were compared with their corresponding average spectra, based on the following equation:

$$\begin{aligned}\text{Difference spectrum }(n^{\text{th}}\text{ measurement}, t) &= \text{Transient spectrum }(n^{\text{th}}\text{ measurement}, t)\\ &\quad - \text{Transient spectrum (average}, t) \qquad (2\text{-}5)\end{aligned}$$

where n = 1, 2, or 3. Apparently, in each panel, the intensities of all the difference spectra were very similar, implying that the frequencies at all the delay time systematically deviated from their average values, in all three independent measurements.

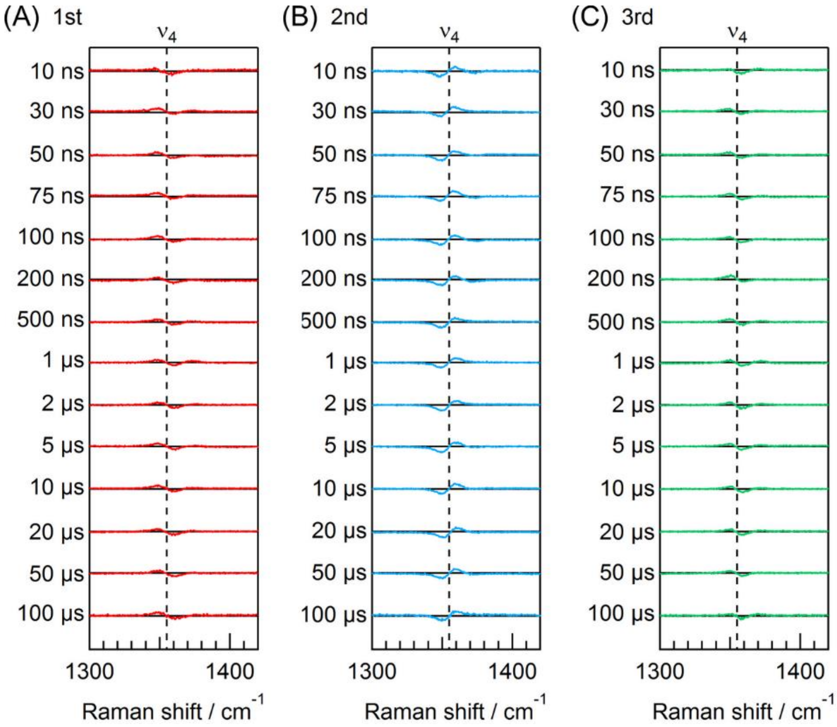

Figure 2-27 Fluctuations of the "ν_4 frequency" relative to its average value, in the case of R mutant at pH 8.0. (A) to (C) are the difference RR spectra of ν_4 band by subtracting the average spectra from its corresponding ones in one single measurement: the red, blue, and green curves represent the spectra in the first, second, and third measurement, respectively; meanwhile, the black lines show the positions of zero intensity.

Figure 2-28 quantitatively describes the fluctuations of "ν_4 frequency", for wild-type rHb at pH 8.0 (A), R mutant at pH 8.0 (B), wild-type rHb at pH 6.4 (C), and T mutant+IHP at pH 6.4 (D), respectively. The results manifest that: (*a*) the "ν_4 frequency" is less reproduced (σ = 0.1-0.3 cm^{-1}) than the "ν_4 frequency shift between two delay times" (σ = 0.02-0.03 cm^{-1}); (*b*) the systematic shift of "ν_4 frequencies" is verified by all of the independent measurements. Actually, the latter observation consists with the high reproducibility of the "ν_4 frequency shift between two delay times".

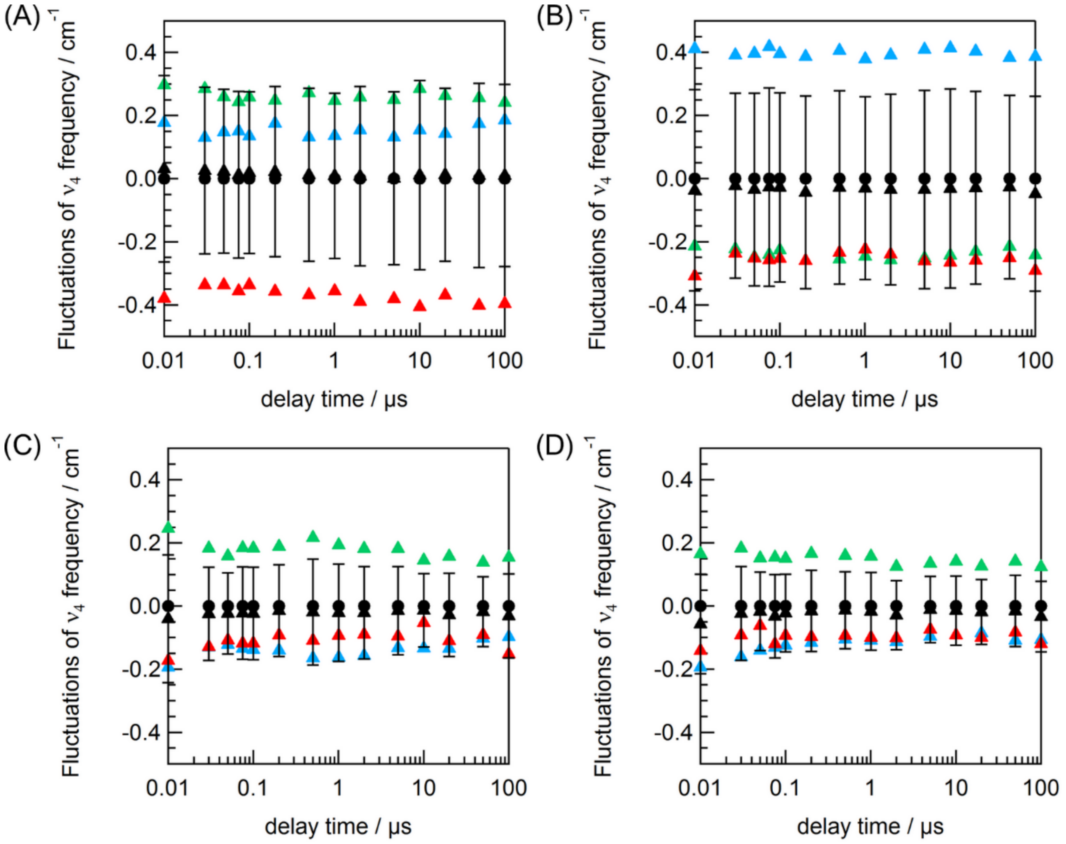

Figure 2-28 Fluctuations of the "ν_4 frequency" relative to its average value, in the case of wild-type rHb at pH 8.0 (A), R mutant at pH 8.0 (B), wild-type rHb at pH 6.4 (C), and T mutant+IHP at pH 6.4 (D), respectively. In each panel, the red, blue, and green triangles represent the spectra in the first, second, and third independent measurement, respectively; the black triangles represent the arithmetic mean values of the red, blue, and green data.

In all, the reproducibility of the "ν_4 frequency shift between two delay times" and of the "ν_4 frequency" have been carefully examined. Table 2-6 summarized the standard deviations. We once worried that our time-resolved RR measurements were not perfectly simultaneous, so that the random environmental perturbations of the apparatus might affect our results. The high reproducibility of the "ν_4 frequency shift between two delay times" implies that the environmental perturbations within 10-20 minutes are negligible, using our time-resolved RR apparatus and experimental strategy (Table 2-3). In other words, all the transient spectra recorded in the same measurements can be regarded as measured quasi-simultaneously.

On the contrary, the random environmental perturbations must be considered if two spectra to be compared are measured by a time interval of many hours, as indicated by the relatively lower reproducibility of the "ν_4 frequency". In our study, the time interval between two adjacent independent measurements fell into the range of 4 to 12 hours, which is long enough to result in a random frequency drift. Our results demonstrate that the random frequency drift is on the scale of 0.1-0.3 cm^{-1} (Table 2-6).

Table 2-5. Standard deviations of "ν_4 frequency shift between two delay times" and "ν_4 frequency".

		ν_4 frequency shift between two delay times / cm^{-1}	ν_4 frequency / cm^{-1}
pH 8.0	Wild-type rHb	0.022	0.28
	R mutant	0.025	0.30
pH 6.4	Wild-type rHb	0.022	0.14
	T mutant+IHP	0.031	0.12

(2) Match of peak intensities

In the present study, each raw spectrum was first baseline-flattened, and then normalized so that its ν_4 intensity was equal to 1.

(3) Increase of signal to noise ratio

In the present study, each transient spectrum was totally accumulated for 18 minutes by three independent measurements (6 minutes each). Consequently, the S/N ratio was largely improved to a satisfied value.

One thing to note is that, as shown in Figure 2-26D, the data directly calculated from the average spectra (black dots) should be more accurate than the arithmetic mean values (black triangles), when the influence of S/N ratio is taken into account. The former were calculated based on the 18-min-accumulated average spectra, whereas the latter were averages of three sets of data (red, blue, and green triangles), which were obtained from the 6-min-accumulated spectra. Since the S/N ratio of the 18-min-accumulated spectra were certainly higher than that of the 6-min-accumulated ones, it is rational that the data directly calculated from the average spectra is more accurate. Therefore, data plotted in Figure 4-6 of Chapter 4 were directly calculated from the average spectra, not the arithmetic mean values of three independent measurements.

(4) Summarization of Section 2.5.1.2

In this section, we carefully examined our apparatus, as well as the data accumulation and analysis method, verifying that our current method generally fulfill all the requirements of applying RDS. Therefore, in Chapter 4, we used RDS to investigate the temporal behavior of ν_4 frequency.

References

1. Shen, T. J.; Ho, N. T.; Zou, M.; Sun, D. P.; Cottam, P. F.; Simplaceanu, V.; Tam, M. F.; Bell, D. A.; Ho, C., *Protein Engineering* **1997,** *10* (9), 1085-1097.

2. Looker, D.; Mathews, A. J.; Neway, J. O.; Stetler, G. L., *Methods in Enzymology* **1994,** *231*, 364-374.

3. Shen, T. J.; Ho, N. T.; Simplaceanu, V.; Zou, M.; Green, B. N.; Tam, M. F.; Ho, C., *Proceedings of the National Academy of Sciences of the United States of America* **1993,** *90* (17), 8108-8112.

4. Nagai, M.; Nagai, Y.; Aki, Y.; Imai, K.; Wada, Y.; Nagatomo, S.; Yamamoto, Y., *Biochemistry* **2008,** *47* (2), 517-525.

5. Birukou, I.; Schweers, R. L.; Olson, J. S., *Journal of Biological Chemistry* **2010,** *285* (12), 8840-8854.

6. Hofrichter, J.; Sommer, J. H.; Henry, E. R.; Eaton, W. A., *Proceedings of the National Academy of Sciences of the United States of America-Biological Sciences* **1983,** *80* (8), 2235-2239; Balakrishnan, G.; Case, M. A.; Pevsner, A.; Zhao, X. J.; Tengroth, C.; McLendon, G. L.; Spiro, T. G., *Journal of Molecular Biology* **2004,** *340* (4), 843-856; Cammarata, M.; Levantino, M.; Wulff, M.; Cupane, A., *Journal of Molecular Biology* **2010,** *400* (5), 951-962; Fischer, S.; Olsen, K. W.; Nam, K.; Karplus, M., *Proceedings of the National Academy of Sciences* **2011,** *108* (14), 5608-5613.

7. Friedman, J. M.; Stepnoski, R. A.; Stavola, M.; Ondrias, M. R.; Cone, R. L., *Biochemistry* **1982,** *21* (9), 2022-2028.

8. Laane, J.; Kiefer, W., *Journal of Chemical Physics* **1980,** *72* (10), 5305-5311.

9. Laane, J., *Journal of Chemical Physics* **1981,** *75* (6), 2539-2545.

10. Bodenhei.Js; Berenblu.Bj; Wilkinso.Gr, *Chemical Physics Letters* **1972,** *14* (4), 533-535; Eng, J. F.; Czernuszewicz, R. S.; Spiro, T. G., *Journal of Raman Spectroscopy* **1985,** *16* (6), 432-437; Kamogawa, K.; Kitagawa, T., *Journal of Physical Chemistry* **1990,** *94* (10), 3916-3921.

11. Kiefer, W., *Applied Spectroscopy* **1973,** *27* (4), 253-257.

12. Deckert, V.; Liebler, W.; Eck, R.; Kiefer, W., *Applied Spectroscopy* **1997,** *51* (7), 939-943.

13. Frosch, T.; Meyer, T.; Schmitt, M.; Popp, J., *Analytical Chemistry* **2007,** *79* (16), 6159-6166.

Chapter 3 Effect of the N-terminal Residues on the Quaternary Dynamics of Human Adult Hemoglobin

3.1 Introduction

Dynamic properties of proteins are essential for specific biological functions. The molecular mechanism of cooperativity of human adult hemoglobin (HbA) is a typical example in which structural changes of the protein regulate its function. HbA, the major blood oxygen transporter, is a tetrameric hemoprotein that composed of two α- and two β-globins. The heme, iron-protoporphrin IX, within each subunit is responsible for the binding of diatomic molecules, such as O_2, CO, and NO. The quaternary structure of HbA undergoes reversible transition between the low-affinity (T or tense) state and the high-affinity (R or relaxed) state upon partial ligation/deligation of the four hemes, which constitutes the structural basis of the cooperativity and allostery of HbA[1]. For many decades, a substantial amount of efforts have been made to uncover the mysterious R→T allosteric transition pathway of HbA[2-6]. However, detailed molecular mechanisms are still not fully understood.

In order to study the structure-function relationships of HbA, an efficient expression system is needed for producing a large amount of recombinant Hb (rHb) as well as rationally designing Hb mutants. In many respect, *Escherichia coli* (*E. coli*) expression system is the best choice. However, the endogenous methionine aminopeptidase (Met-AP) of *E. coli* cannot cleave the initiator methionine (Met) from both α- and β-globins of rHb[7]. The extensions of the N-termini interfere with some functional and structural properties of the whole protein[7-10], probably because the natural N-terminal Valine (Val) residues of HbA are involved in Bohr effect[11, 12] and interactions with inorganic anions[12] and organic phosphate[13]. Two strategies have been used to circumvent this problem. One strategy is to add a Met-AP gene into the rHb expression plasmid. The initiator Met of rHb may be cleaved by a mass of coexpressed Met-AP. Ho's group used this strategy to construct the pHE2, pHE4, and pHE7 plasmids, proving that these plasmids were capable of expressing normal rHb in *E. coli*[8, 14].

A much simpler strategy is to replace the N-terminal Val codons by the initiator Met codons to yield the α(V1M)/β(V1M) double mutant. Since the functional roles of the N-terminal residues are primarily contributed by the more reactive amino groups, side chain substitutions of the N-terminal residues should have minimal effect on the properties of rHb. Looker *et al*[15] and Hernan *et al*[9, 16] adopted this strategy independently. Experimental data[9] demonstrated that despite of the slightly lower oxygen affinity, the kinetic and thermodynamic properties, as well as the cooperativity of the α(V1M)/β(V1M) double mutant closely approximate those of HbA. Therefore, the α(V1M)/β(V1M) double mutant has been used as a suitable surrogate of HbA for structure-function studies[15, 17-19]. However, to our knowledge, the structural dynamics along the R→T transition pathway of the α(V1M)/β(V1M) double mutant has not been examined yet.

Time-resolved resonance Raman (RR) spectroscopy provides valuable information on protein dynamics. In this study, we measured heme-resonant Raman spectra of the α(V1M)/β(V1M) double mutant and the normal rHb expressed in *E. coli*, then compared their spectra with those of HbA purified from blood. The result showed that the dynamic behavior of the α(V1M)/β(V1M) double mutant was distinct from that of HbA in the tens of microseconds region, whereas the dynamic properties of normal rHb was quite similar to those of HbA. The implications of this result on understanding the allosteric pathway of HbA are discussed in detail.

3.2 Experimental section

3.2.1 Preparation of protein samples

3.2.1.1 Human adult hemoglobin (HbA)

Ferrous stabilized HbA was purchased from Sigma and was used without further purification.

3.2.1.2 Preparation of normal rHb

The normal rHb was expressed from the pHE7 expression plasmid, in which cDNA α- and β-globin genes and the *E. coli* methionine aminopeptidase (Met-AP) gene are coexpressed under the control of separate promoters[8]. Results confirmed that over 97% polypeptides in the purified samples had no initiator Met residue in the N-termini. Detailed procedures are described in Section 2.2 of Chapter 2.

3.2.1.3 Preparation of α(V1M)/β(V1M) double mutant

The α(V1M)/β(V1M) double mutant was expressed from the pSGE1702 expression plasmid in *E. coli* SGE1661 and purified according to a previously described procedure[17, 18, 20], see also Section 2.3 of Chapter 2 for detailed information. The pSGE1702 expression plasmid contains one copy each of the α- and β-globin genes, in which the valine residues at the N-termini were substituted by methionine. The kinetic and thermodynamic properties, as well as the cooperativity of the α(V1M)/β(V1M) double mutant closely approximate those of HbA[9], therefore, the double mutant has been used as a surrogate of HbA for many structure-function studies.

3.2.2 Steady-state and time-resolved heme-resonant Raman measurements

Nanosecond pulse lasers operating at 1 kHz were employed in the measurements[18, 21], see Section 2.3 of Chapter 2 for detailed information. In brief, probe pulses at 436 nm (0.5 μJ/pulse) was used to excite the protein sample. In time-resolved measurements, pump pulses, which do not have resonant effect on heme, were adjusted to 185 μJ/pulse to photodissociate CO from Hb.

The concentration of Hb samples for Raman measurements was 100 μM (heme).

3.3 Results

3.3.1 Static resonance Raman spectra of the deoxy and CO-bound forms

Figure 3-1 shows the static RR spectra of HbA from blood, normal rHb, and the α(V1M)/β(V1M) double mutant in the deoxy (A) and CO-bound (B) forms. One thing to be noted is that, all the deoxy spectra were obtained in the single measurements due to limited protein samples, which might generate an experimental error within 1 cm^{-1}. As a result, for the comparison of the static deoxy spectra, only the frequency shift larger than 1-cm^{-1} is worth to be discussed. In this sense, the frequencies of each band in Figure 3-1 were very similar between three Hb species, in both deoxy and CO-bound forms.

In addition, this is the first time to show the deoxy and CO-bound spectra of Hb in the present thesis, so that it is necessary to introduce the mode assignments[22] in detail. All the bands in the 1000-1700 cm^{-1} region arise from the in-plane vibrations of the heme. The frequencies of the ν_4, ν_3, ν_2, and ν_{10} bands were 1372, 1499, 1586, and 1635 cm^{-1} in the CO-bound form (Figure 3-1B), and downshifted to 1356, 1472, 1568, and 1623 cm^{-1} in the deoxy form (Figure 3-1A), manifesting that the core size of the heme was expanded after the ligand photolysis.

The static RR spectra in the 170-850 cm^{-1} region were more informative. In the deoxy spectra (Figure 3-1A), the bands at 213/214, 299/300, 340/341, and 364/365 cm^{-1} were assigned to vibrations of the heme. The band at 213 or 214 cm^{-1} denotes the stretching mode of the covalent band between the heme iron and the N_ε of the proximal His, ν(Fe-His). It should be noted that the ν(Fe-His) bands were asymmetric, so that the frequencies were not labeled at the peak positions, but were calculated as the average frequencies. The bands at 299 or 300 cm^{-1} were assigned to an out-of-plane mode, γ_7. The bands at 340 or 341 cm^{-1} arise from a metal-pyrrole stretch and substituents bend, ν_8. The bands at 364 or 365 cm^{-1} were assigned to a substituent mode which involves deformation of the propionate methylene groups, $\delta(C_\beta C_c C_d)$. Another important band located at 672 cm^{-1}, which was assigned to a breathing-like mode of the porphyrin inner ring and labeled as ν_7.

The CO-bound spectra in the 170-850 cm^{-1} region (Figure 3-1B) were distinct from the deoxy spectra in the same region. The ν(Fe-His) mode disappeared and the ν_7 band right-shifted to 674 cm^{-1}. In addition, a new peak at 502 cm^{-1} occurred and was ascribed to the stretching mode of the covalent band between the heme iron and the carbon atom of the carbon monoxide, ν(Fe-CO).

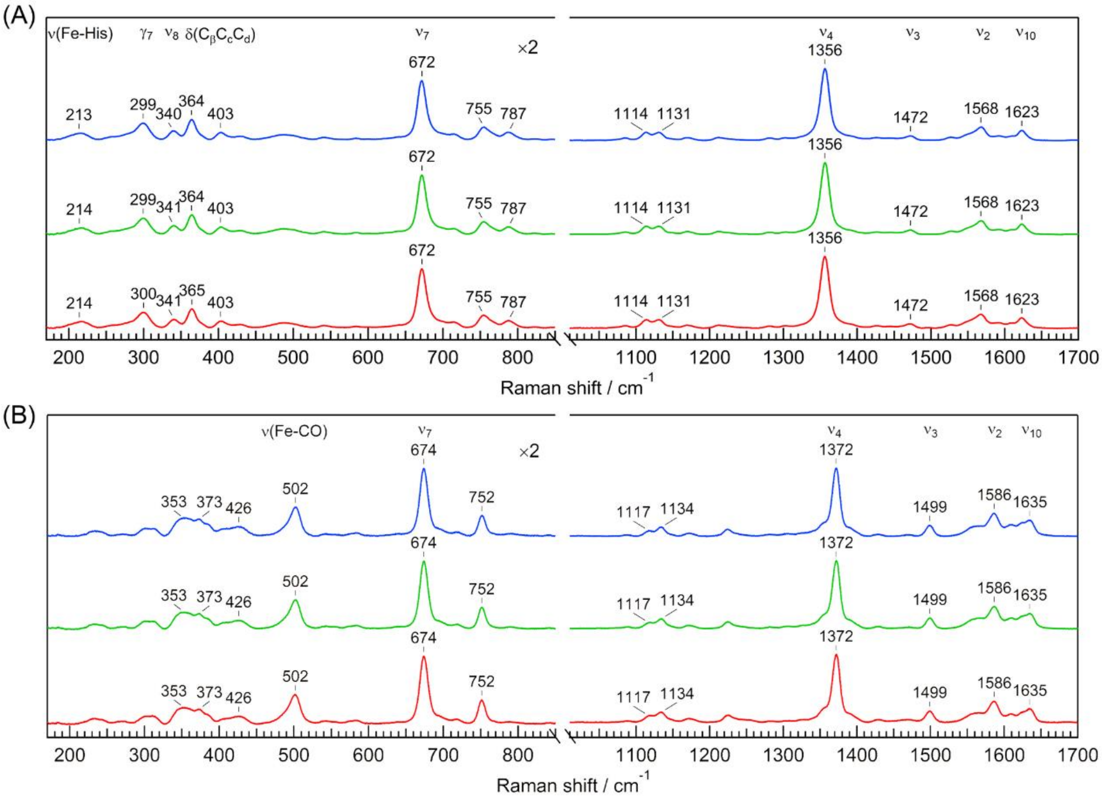

Figure 3-1. Static spectra of the three Hb samples in the deoxy (A) and CO-bound (B) forms. In each panel, the blue, green, and red traces represent spectra of HbA from blood, normal rHb, and the α(V1M)/β(V1M) double mutant, respectively. The intensity of each spectrum in the 170-850 cm^{-1} region was multiplied by 2. The accumulation time for each spectrum was 60 minutes, except for the high frequency part of the CO-bound form, which was 18 minutes.

3.3.2 Time-resolved resonance Raman spectra

Figure 3-2 exhibits the nanosecond time-resolved RR spectra of HbA from blood (a and b), normal rHb (c and d), and the α(V1M)/β(V1M) double mutant (e and f), following the photodissociation of CO. For each Hb species, the left panel shows the spectra in the 1000-1700 cm^{-1} region, while the right panel display the spectra in the 170-850 cm^{-1} region. The transient spectra resemble the spectra of the deoxy form, except that the frequencies or intensities of some bands deviated from the deoxy values. In each panel of Figure 3-2, the band frequencies were labeled in the spectra at 30 ns and 100 μs, helping us to figure out the variation trends of some important bands. Obviously, the variation trends for normal rHb and α(V1M)/β(V1M) double mutant were similar to those of HbA from blood.

The variation trends of some important bands for HbA from blood were summarized from Figure 3-2a and 2b. In the 1000-1700 cm^{-1} region (Figure 3-2a), the frequencies of ν_2, ν_3, ν_4, and ν_{10} bands at 30 ns were dramatically left-shifted from the CO-bound values (Figure 3-1B), but showed only slightly difference from the deoxy values (Figure 3-1A). Moreover, the band frequencies at 100 μs almost approached the deoxy values. Therefore, it could be inferred that after the photodissociation of CO, the core size of the heme promptly expands within 30 ns, and then slightly contracted to its deoxy size.

In the 170-850 cm^{-1} region (Figure 3-2b), the transient spectrum resembled the spectra of the deoxy form (Figure 3-1A) immediately after the photolysis of CO. At 30 ns, the frequencies of ν(Fe-His) and γ_7 bands were higher than those in the spectra of the deoxy form. In addition, almost half of the ν_8 band was overlapped with the $\delta(C_\beta C_c C_d)$ band. As the delay time increased, the frequencies of ν(Fe-His) and γ_7 bands left-shifted. Meanwhile, the ν_8 became more prominent due to the downshift of its frequency and the increase of its intensity. Furthermore, the intensity of the $\delta(C_\beta C_c C_d)$ band also increased. At 100 μs, the spectrum was very similar to the deoxy spectrum (Figure 3-1A) except the ν(Fe-His) frequency.

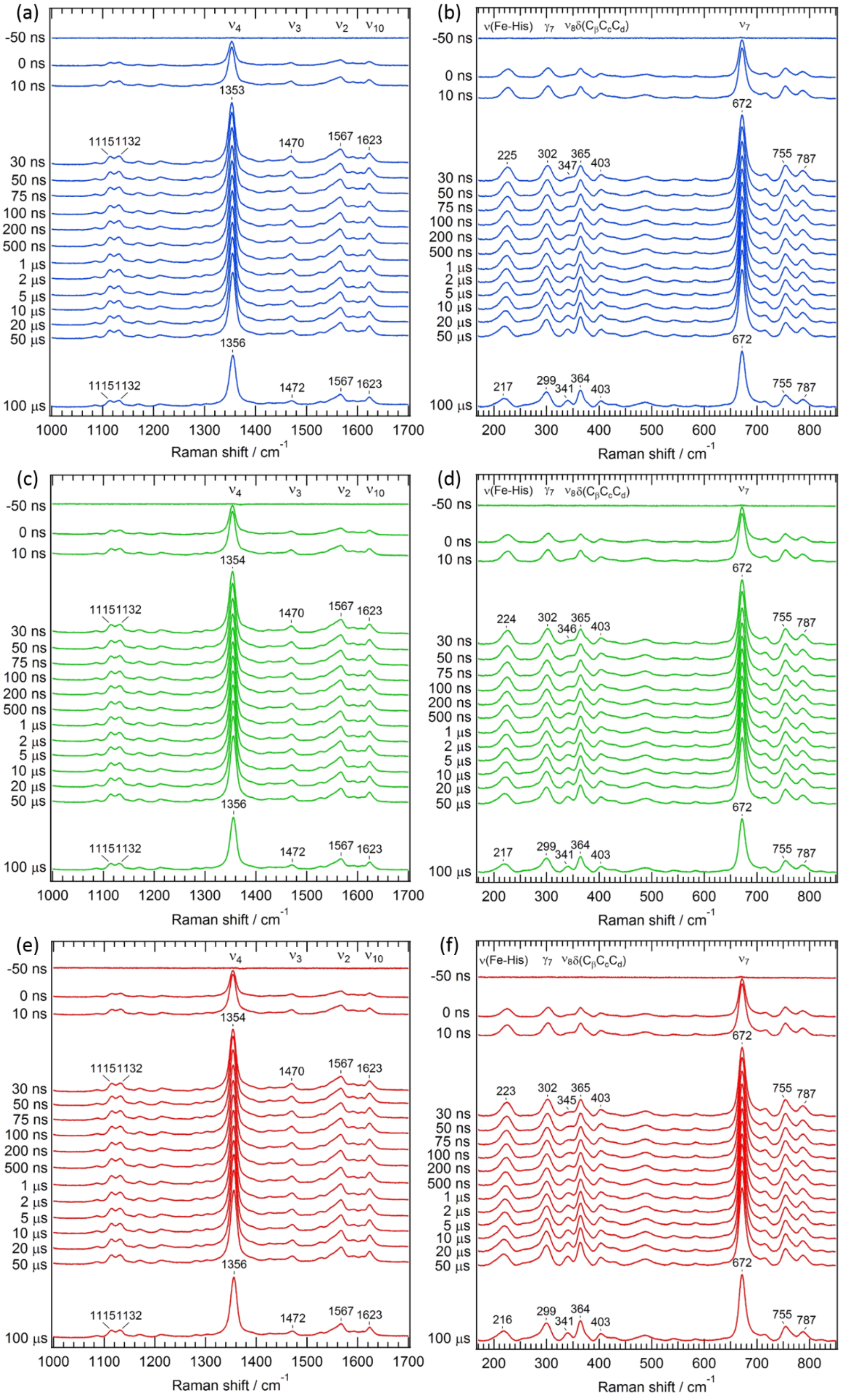

Figure 3-2. Time-resolved RR spectra of HbA from blood (a and b), normal rHb (c and d), and the α(V1M)/β(V1M) double mutant (e and f). The accumulation time for each transient spectrum in the 1000-1700 cm^{-1} region was 18 minutes, and in the 170-850 cm^{-1} region was 60 minutes.

The expanded view of the time-resolved spectra near the ν(Fe-His) and ν_8 bands are shown in Figure 3-3. Besides that, Figure 3-4 compares the temporal evolutions of the ν(Fe-His) frequency and the intensity of the ν_8 band of three Hb species upon the photodissociation of CO. The intensities shown in this figure are the relative values to the intensity of the ν_7 band. To make a further investigation, multiple-exponential functions were employed to fit the raw data. For ν(Fe-His) frequency, the triple- exponential function was used; while in the case of the ν_8 intensity, the double-exponential function was applied. All the time constants were summarized in Table 3-1.

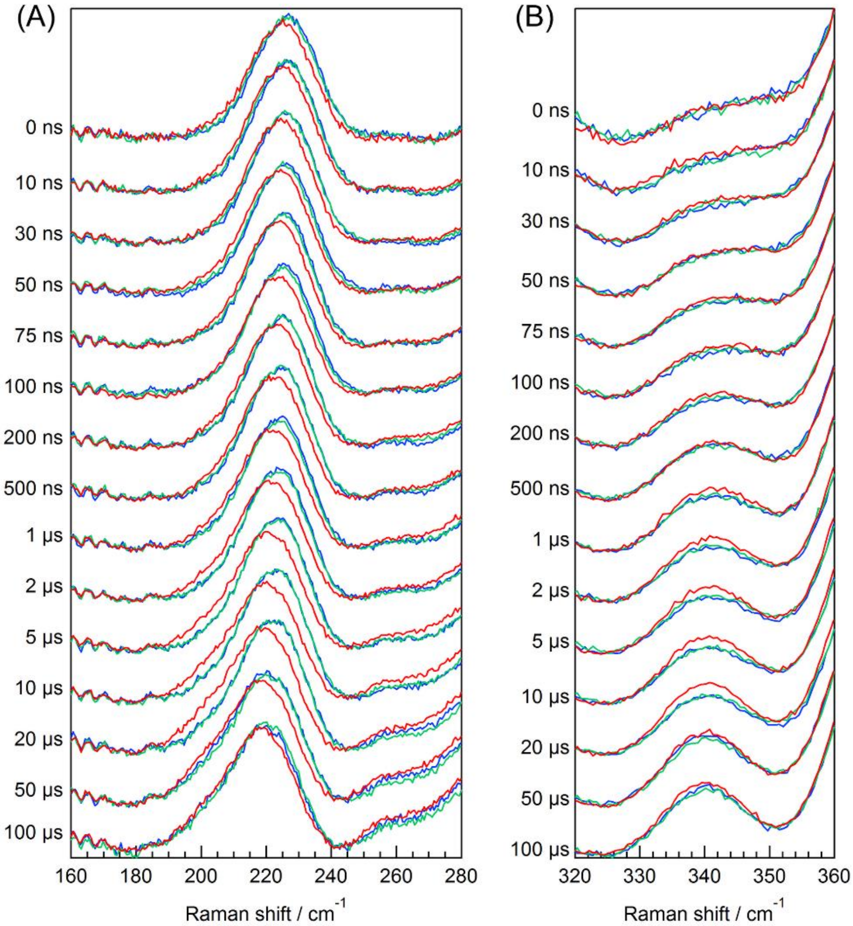

Figure 3-3. Expanded time-resolved RR spectra of HbA from blood (blue), normal rHb (green), and the α(V1M)/β(V1M) double mutant (red) in the 180-260 (A), and 320-360 (B) cm^{-1} region. Note that all the spectra were normalized according to the intensity of the ν_7 band.

As displayed in Figure 3-4, the data of the normal rHb were indistinguishable from the corresponding ones of the HbA in allowable experimental error. On the contrary, the dynamic behavior of the α(V1M)/β(V1M) double mutant was different from that of HbA. Apparently, the main dynamic difference was in the time region of tens of microseconds, which can be inferred from the τ_3 values of the ν(Fe-His) frequency shift, as well as the τ_2 values of the intensity change of ν_8 band. For HbA from blood and normal rHb, the time constants was ~30 μs; whereas for the double mutant, they were reduced, only ~10 μs. That is to say, the conformational change in tens of microseconds was accelerated by the mutation of the N-terminus residues.

Besides the dynamic difference in the tens of microseconds region, the ν(Fe-His) frequency of the double mutant systematically decreased by 1.6 cm^{-1}, as compared to the corresponding values of the other two Hb species. Moreover, it should be noticed that this frequency decrease was observed at the time as early as 10 ns.

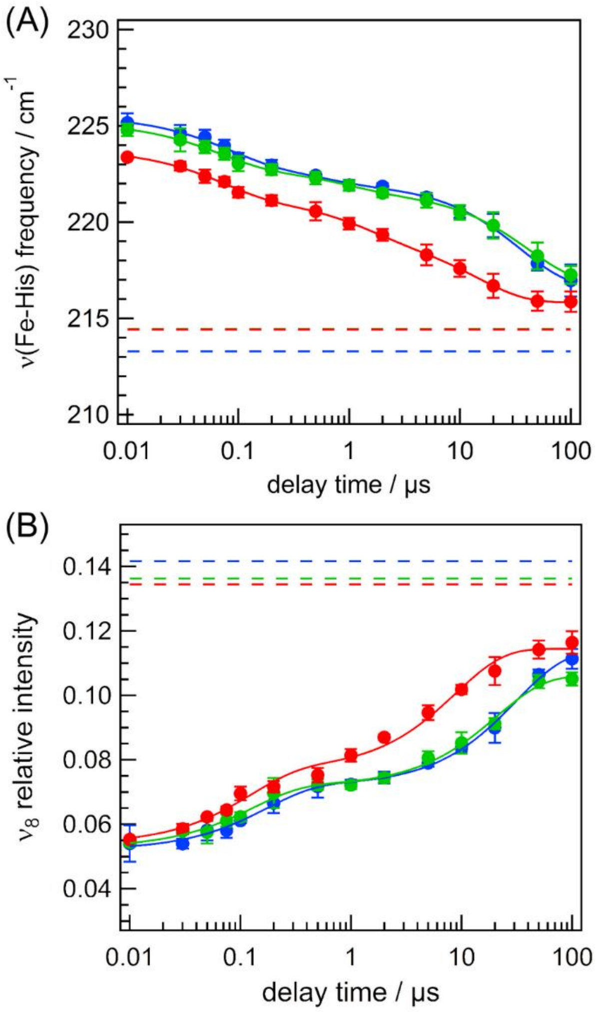

Figure 3-4. Logarithmic time plots of the ν(Fe−His) frequency (A) and the relative intensity of the ν_8 band (B). The blue, green, and red circles represent the values for HbA from blood, normal rHb, and the α(V1M)/β(V1M) double mutant, respectively. They are averages for ten independent measurements. The error bars show standard deviations calculated for the independent measurements. The solid curves indicate the best fit obtained using a sum of exponential functions. The broken lines show the values for the deoxy forms, which were obtained in the single measurements.

Table 3-1. Time constants of temporal evolution of Raman bands from three hemoglobin species.

		τ_1 / ns	τ_2 / μs	τ_3 / μs
ν(Fe−His)	HbA from blood	75±34 (26±9%)	0.50±0.45 (13±9%)	35±5 (61±3%)
	Normal rHb	65±11 (28±2%)	0.91±0.29 (15±2%)	41±4 (57±2%)
	α(V1M)/β(V1M) double mutant	69±10 (31±2%)	1.3±0.4 (25±3%)	14±2 (44±3%)

		τ_4 / ns	τ_5 / μs
ν_8	HbA from blood	170±30 (32±2%)	31±3 (68±2%)
	Normal rHb	130±20 (36±3%)	21±2 (64±3%)
	α(V1M)/β(V1M) double mutant	120±30 (38±5%)	8.9±1.4 (62±3%)

Numbers in parentheses show the fraction of that component.

3.4 Discussion

The effects of N-terminal substitution on the equilibrium protein structure [9, 23], oxygen affinity [9, 23-25], Bohr effect [23, 24], and kinetic features [9, 23] have been previously studied, but the present work is the first to clarify the effect on the structural dynamics of the protein along the allosteric pathway.

3.4.1 Protein dynamics along the allosteric pathway

As early as 1979, Baldwin and Chothia[2] proposed the famous model to describe the R→T transition. In this model, the αβ dimer is regarded as a semi-rigid body, and the R→T quaternary transition is interpreted as the relative rotation/translation of the two αβ-dimers. Their model also indicated that, during the rotation of the two αβ-dimers, the $\alpha_1\beta_1$ interface undergoes dramatic structural change.

The earliest time-resolved absorption spectroscopy[3] suggested that the rotation of the two αβ-dimers happened at ~20 μs. However, this time scale was challenged by later studies. In 2004, Spiro *et al*[4] discovered that the R→T quaternary transition is stepwise. In other words, there is a fast (3 μs) as well as a slow (20 μs) step. Moreover, in 2010, the experimental data of time-resolved wide-angle X-ray scattering (TR-WAXS)[5] reveal that the main structural rearrangement takes place ~2 μs after the photodissociation of CO, the time-scale of which should be correlated to the rotation of two αβ-dimers.

In 2011, Karplus *et al*[6] proposed a "two-quaternary-transition state" model based on their computational results, which can satisfactorily interpret most of the published time-resolved spectroscopic experimental results[4, 5]. However, some parts of their model still need more experimental evidence. According to Karplus' model[6], the fast quaternary step (~2 μs) corresponds to the rotation of two αβ-dimers, while an unexpected quaternary process dominates the slow step (~20 μs). They suggested that during the slow step, the protein behaves as if there were three semi-rigid bodies: the α_1-subunit, the α_2-subunit, and the $\beta_1\beta_2$-dimer. Two α-subunits rotates simultaneously relative to the "stationary" $\beta_1\beta_2$-dimer. Consequently, the $\alpha_1\alpha_2$ interface is predicted to change during the slow quaternary transition step. Therefore, if there is experimental result to show that mutation(s) in the $\alpha_1\alpha_2$ interface can affect the slow quaternary step of HbA, Karplus' model may be more convincible. However, to our knowledge, there is no such evidence, since almost all the researchers have focused their attention on the $\alpha_1\beta_2$ interface.

It is indicated from the present results that the mutation of the N-terminal residues accelerates the slow quaternary step (~20 μs) of HbA. The X-ray crystallographic evidence have proved that the side-chain of αV1 faces to the outward (Figure 3-5) and protrudes into the $\alpha_1\alpha_2$ interface (Figure 3-6B and C), whereas the side-chain of βV1 is buried in its own subunit (Figure 3-5). It is known that quaternary structural change only occurs in the interface between different subunits. Therefore, the quaternary transition is much more likely affected by the αV1→M mutation, rather than the βV1→M mutation. As a result, an interesting relationship might be built between the αV1→M mutation and Karplus' "two-quaternary-transition state" model: our present results indicate that the αV1→M mutation may probably affect the slow quaternary step, which coincides with the prediction of Karplus' model.

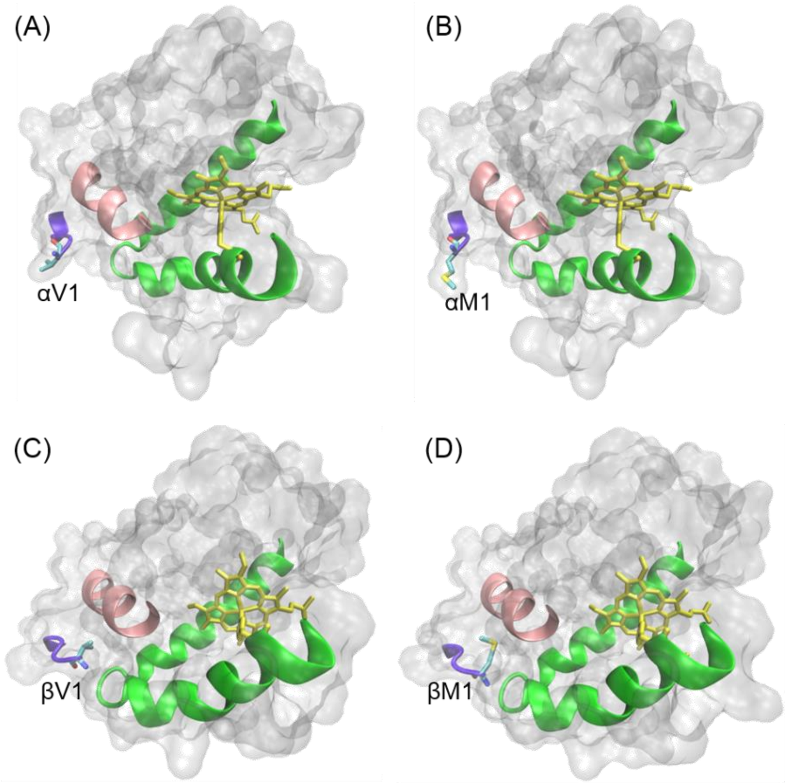

Figure 3-5. Conformations of N-terminal residues in T state. (A) and (B) represent α subunit, while (C) and (D) represent β subunit. The PDB IDs of the crystal structures shown in (A), (B), (C), and (D) are 2DN2, 1BZZ, 2DN2, and 1DXU, respectively.

3.4.2 Acceleration of the second step by the V1→M mutation.

The present data showed that the V1→M mutation accelerates the second step in the R→T quaternary transition but does not affect the first step. This acceleration can be attributed to differences in the Val and Met side chains. In this section, a possible molecular mechanism was proposed.

Figure 3-6 compares the crystallographic structures of the R and T states of HbA. The side chain of α_1V1 has closest contact with the side chain of α_2S138 of all the α_2 residues (Figure 3-6B and C), so α_2S138 can most significantly perturb the α_1V1 side chain. Figure 3-6A compares the crystal structures of HbA in the R and T states [26]. The structures of the α subunits in the R and T states are overlaid in panel A. The H helices of the α_1 and α_2 subunits shift away from each other upon the R→T transition. α_2S138 is located adjacent to the end of the α_2H helix and moves together with the helix. Thus, the distance between α_2S138 and α_1V1 is shorter in the R state than in the T state, resulting in stronger repulsion between the side chain of α_1V1 and α_2S138 (Figure 3-6A). In fact, the side chain of α_1V1 rotates around the C_α−C_β bond during the R→T transition. A detailed comparison of the conformations of α_1V1 in the T and R states is shown in Figure 3-6D.

The side chain of α_1M1 in the mutant is more perturbed by α_2S138 than is the Val in HbA due to stronger repulsion between α_2S138 and α_1M1 upon the R→T transition. This stronger perturbation arises from the Met side chain being larger than the Val side chain. Indeed, the crystal structure of the αV1M mutant in the T state shows that the αM1 side chain is highly disordered [9]. Figure 3-6E shows the B-factors of the C_γ, S_δ, and C_ε atoms obtained by crystallographic analysis. All these B-factors are larger than 100 $Å^2$, indicating flexibility of the side chain. This is in contrast to the B-factors of the atoms of α_1V1, which are about 30-60 $Å^2$, as shown in Figure 3-5D. The highly disordered structure of the α_1M1 side chain suggests that the V1→M mutation destabilizes the protein. For the V1M mutant, the R state is more destabilized than the T state because the distance between α_2S138 and α_1V1 is shorter in the R state. It is highly likely that the destabilization of the R state is why the V1→M mutation accelerates the R→T transition.

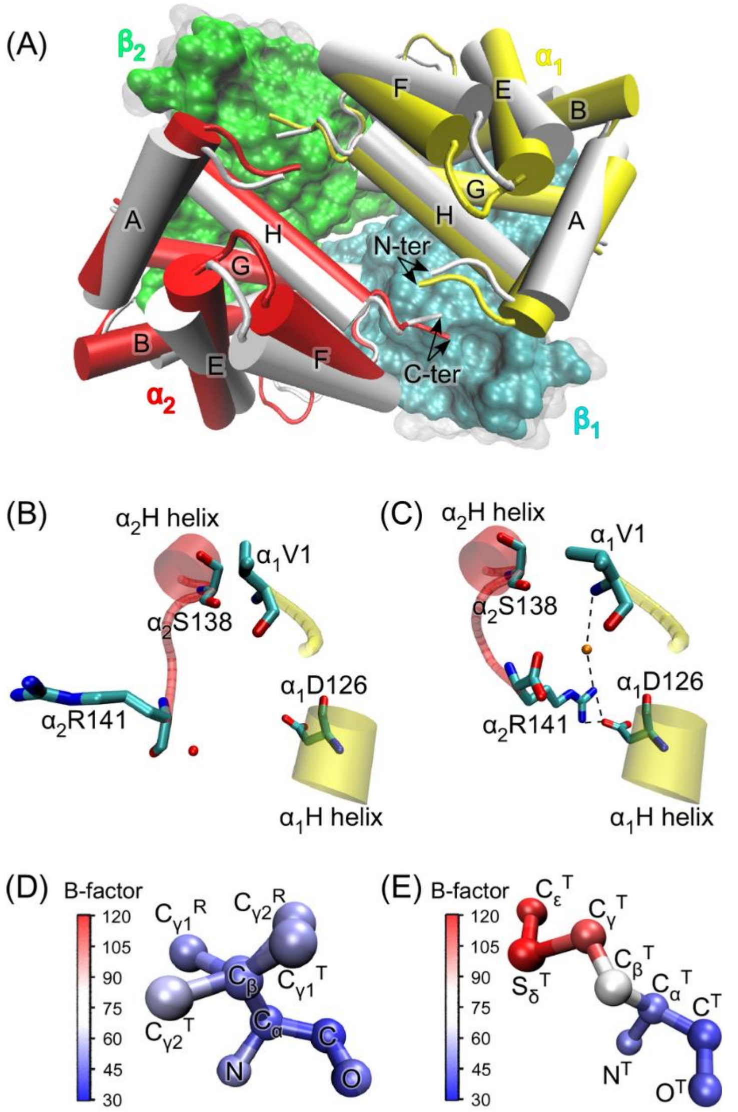

Figure 3-6. Crystallographic structures of the R and T states of HbA. Panel (A) shows the global structural changes between the R (in color) and T (in white) states. The C-helices of the α-subunits are hidden behind the F-helices. Panels (B) and (C) show the local structure around α1V1 in the R and T states, respectively. The red sphere in (B) represents the oxygen atom of the α2R141 carboxyl group, whose position is poorly defined. The orange sphere in (C) represents the oxygen of a water molecule present only in the T state. Although the area of the orange sphere was refined as an O atom of a water molecule, it is thought to be an inorganic anion binding site.[9, 27] Panel (D) shows the B-factors for each atom of α1V1 in the R and T states and Panel (E) shows the B-factors for each atom of α1M1 in the T state. The PDB IDs of the R state of HbA, the T state of HbA, and the T state of the αV1M mutant are 2DN3, 2DN2, and 1BZZ, respectively.

3.5 Conclusions

In this study, we examined in detail the temporal behavior of time-resolved RR spectra of two recombinant Hbs, the α(V1M)/β(V1M) double mutant and normal rHb, as well as Hb isolated from blood. Spectral changes in the frequency shift of the ν(Fe−His) band and increases in the intensity of the ν_8 band were observed for all three Hb samples. The spectral changes of the α(V1M)/β(V1M) double mutant were distinct from those of HbA in the tens of microseconds region, whereas the spectral changes of normal rHb and HbA were similar. The present study demonstrated that structural changes in the N-termini are involved in the second step of the R→T quaternary transition of HbA. In addition, the importance of the $\alpha_1\alpha_2$ interface on the quaternary transition is verified. These findings help further characterize the protein dynamics regulating the allosteric pathway of Hb.

References

1. Monod, J.; Wyman, J.; Changeux, J. P., *Journal of Molecular Biology* **1965,** *12* (1), 88-118.

2. Baldwin, J.; Chothia, C., *Journal of Molecular Biology* **1979,** *129* (2), 175-220.

3. Hofrichter, J.; Sommer, J. H.; Henry, E. R.; Eaton, W. A., *Proceedings of the National Academy of Sciences of the United States of America-Biological Sciences* **1983,** *80* (8), 2235-2239.

4. Balakrishnan, G.; Case, M. A.; Pevsner, A.; Zhao, X. J.; Tengroth, C.; McLendon, G. L.; Spiro, T. G., *Journal of Molecular Biology* **2004,** *340* (4), 843-856.

5. Cammarata, M.; Levantino, M.; Wulff, M.; Cupane, A., *Journal of Molecular Biology* **2010,** *400* (5), 951-962.

6. Fischer, S.; Olsen, K. W.; Nam, K.; Karplus, M., *Proceedings of the National Academy of Sciences* **2011,** *108* (14), 5608-5613.

7. Hoffman, S. J.; Looker, D. L.; Roehrich, J. M.; Cozart, P. E.; Durfee, S. L.; Tedesco, J. L.; Stetler, G. L., *Proceedings of the National Academy of Sciences of the United States of America* **1990,** *87* (21), 8521-8525.

8. Shen, T. J.; Ho, N. T.; Zou, M.; Sun, D. P.; Cottam, P. F.; Simplaceanu, V.; Tam, M. F.; Bell, D. A.; Ho, C., *Protein Engineering* **1997,** *10* (9), 1085-1097.

9. Hui, H. L.; Kavanaugh, J. S.; Doyle, M. L.; Wierzba, A.; Rogers, P. H.; Arnone, A.; Holt, J. M.; Ackers, G. K.; Noble, R. W., *Biochemistry* **1999,** *38* (3), 1040-1049.

10. Doyle, M. L.; Lew, G.; Deyoung, A.; Kwiatkowski, L.; Wierzba, A.; Noble, R. W.; Ackers, G. K., *Biochemistry* **1992,** *31* (36), 8629-8639.

11. Perutz, M. F.; Muirhead, H.; Mazzarel.L; Crowther, R. A.; Greer, J.; Kilmarti.Jv, *Nature* **1969,** *222* (5200), 1240-1243; Kilmarti.Jv; Rossiber.L, *Nature* **1969,** *222* (5200), 1243-1246; Garner, M. H.; Bogardt, R. A.; Gurd, F. R. N., *Journal of Biological Chemistry* **1975,** *250* (12), 4398-4404.

12. Odonnell, S.; Mandaro, R.; Schuster, T. M.; Arnone, A., *Journal of Biological Chemistry* **1979,** *254* (23), 2204-2208.

13. Perutz, M. F., *Nature* **1970,** *228* (5273), 734-739; Arnone, A., *Nature* **1972,** *237* (5351), 146-

149.

14. Shen, T. J.; Ho, N. T.; Simplaceanu, V.; Zou, M.; Green, B. N.; Tam, M. F.; Ho, C., *Proceedings of the National Academy of Sciences of the United States of America* **1993,** *90* (17), 8108-8112.

15. Looker, D.; Abbottbrown, D.; Cozart, P.; Durfee, S.; Hoffman, S.; Mathews, A. J.; Millerroehrich, J.; Shoemaker, S.; Trimble, S.; Fermi, G.; Komiyama, N. H.; Nagai, K.; Stetler, G. L., *Nature* **1992,** *356* (6366), 258-260.

16. Hernan, R. A.; Sligar, S. G., *Journal of Biological Chemistry* **1995,** *270* (44), 26257-26264.

17. Birukou, I.; Schweers, R. L.; Olson, J. S., *Journal of Biological Chemistry* **2010,** *285* (12), 8840-8854.

18. Yamada, K.; Ishikawa, H.; Mizutani, Y., *Journal of Physical Chemistry B* **2012,** *116* (6), 1992-1998.

19. Yamada, K.; Ishikawa, H.; Mizuno, M.; Shibayama, N.; Mizutani, Y., *Journal of Physical Chemistry B* **2013,** *117* (41), 12461-12468.

20. Looker, D.; Mathews, A. J.; Neway, J. O.; Stetler, G. L., *Methods in Enzymology* **1994,** *231*, 364-374.

21. Mizutani, Y.; Kitagawa, T., *Journal of Physical Chemistry B* **2001,** *105* (44), 10992-10999.

22. Abe, M.; Kitagawa, T.; Kyogoku, Y., *J. Chem. Phys.* **1978,** *69* (10), 4526-4534.

23. Doyle, M. L.; Lew, G.; De Young, A.; Kwiatkowski, L.; Wierzba, A.; Noble, R. W.; Ackers, G. K., *Biochemistry* **1992,** *31* (36), 8629-8639.

24. Looker, D.; Abbott-Brown, D.; Cozart, P.; Durfee, S.; Hoffman, S.; Mathews, A. J.; Miller-Roehrkh, J.; Shoemaker, S.; Trimble, S.; Fermi, G.; Komiyama, N. H.; Nagai, K.; Stetler, G. L., *Nature* **1992,** *356* (6366), 258-260.

25. Looker, D.; Mathews, A. J.; Neway, J. O.; Stetler, G. L., *Methods Enzymol.* **1994,** *231*, 364-74.

26. Park, S.-Y.; Yokoyama, T.; Shibayama, N.; Shiro, Y.; Tame, J. R. H., *J. Mol. Biol.* **2006,** *360* (3), 690-701.

27. O'Donnell, S.; Mandaro, R.; Schuster, T. M.; Arnone, A., *J. Biol. Chem.* **1979,** *254* (23), 12204-8.

Chapter 4 Time-resolved Resonance Raman Studies on Tertiary Dynamics in R and T Quaternary Structures of Human Adult Hemoglobin

4.1 Introduction

The apparent binding affinity of HbA increases as the number of bound oxygen molecules increases, which is called cooperativity. According to the widely accepted Monod-Wyman-Changeux (MWC) model[1], HbA achieves its cooperativity by a reversible transition between two distinct quaternary structural states, the low-affinity (T or tense) state and the high-affinity (R or relaxed) state. To realize the quaternary transition, certain tertiary structural changes are also indispensable.

In order to further illustrate the mechanism of cooperativity, it is necessary to characterize the dynamics of higher-order structure of HbA. Several researchers[2, 3] attempted to selectively study the tertiary transition, while the quaternary structure maintains unchanged. Most of their methods share one common point: encapsulating Hb in gel to decelerate the structural changes[3]. However, gel is not a physiological environment, which might affect the dynamics of HbA. Consequently, it is better to investigate the tertiary structural changes in solution. My strategy is to use two Hb mutants[4], Hb Kempsey and Hb Kansas[5]. Hb Kempsey is restricted in R quaternary state[6], whereas Hb Kansas is constrained in T quaternary state in the presence of IHP[7]. They only have tertiary structural changes, so that tertiary structural changes in R and T states can be observed. For convenience, in this chapter, Hb Kempsey and Hb Kansas are called R and T mutants, respectively.

Time-resolved resonance Raman (RR) spectroscopy provides valuable information on protein dynamics. The ν(Fe-His) frequency in the heme-resonant Raman spectrum of Hb is often used as a marker to study the dynamics of Hb. In addition, the ν_4 frequency and the ν_8 intensity are all good Raman markers to monitor the structural changes of rHb. In this study, I tried to separate the quaternary and tertiary transitions of Hb in solution, using ν_4, ν(Fe-His) and ν_8 bands as markers.

4.2 Experimental section

4.2.1 Site-directed mutagenesis

The pHE7 expression plasmid[8], which contains human α- and β-globin cDNAs, was used as a template to construct the mutant plasmids. Detailed description of how to generate mutated plasmids was shown in Chapter 2.

In brief, for the plasmid expressing R mutant (βD99N), the DNA sequence of the 99th residue of the β-globin was mutated from “GAT” to “AAT”. Similarly, in the case of T mutant (βN102T), the DNA sequence of the 102nd residue of the β-globin was mutated from “AAC” to “ACC”.

4.2.2 Preparation of protein samples

The wild-type rHb and two Hb mutants were prepared using the same method, as described in Chapter 2. Actually, the wild-type rHb mentioned in this chapter is exactly the same as normal rHb studied in Chapter 3.

4.2.3 Steady-state and time-resolved heme-resonant Raman measurements

Nanosecond pulse lasers operating at 1 kHz were employed in the measurements, see Chapter 2 for detailed information. In brief, probe pulses at 436 nm was used to obtain heme-resonant Raman spectra. In time-resolved measurements, pump pulses, which do not have resonant effect on heme, were adjusted to 185 μJ/pulse to photodissociate CO from Hb.

The concentration of Hb samples for Raman measurements was 100 μM (heme). For R mutant, the buffer of protein solution was 50 mM sodium phosphate at pH 8.0. Since a low pH environment and the presence of inositol hexakisphosphate (IHP) are two necessary conditions to keep the CO-derivative of T mutant stay in the T quaternary state, HEPES buffer at pH 6.4 was used to dissolve the T mutant. For each of the two Hb mutants, wild-type rHb was used as a control, so that its spectra were measured in both buffer conditions.

4.3 Results

4.3.1 Static-state heme-resonant Raman spectra

Static-state heme-resonant Raman spectra of different Hb species were shown and compared in this section. The mode assignments are the same as those illustrated in Chapter 3, so that are not introduced in detail in this section. Another point to be noted is that, all the deoxy spectra were obtained in the single measurements due to limited protein samples, which might generate an experimental error within 1 cm^{-1}. As a result, for the comparison of the static deoxy spectra, only the frequency shift larger than 1-cm^{-1} is worth to be discussed.

4.3.1.1 Comparison of R mutant with wild-type rHb

Figure 4-1 shows the static-state spectra of R mutant and wild-type rHb measured at pH 8.0. In their deoxy forms (Figure 4-1A), the spectra of these two Hb species display some clear differences, which indicates that the deoxy heme pocket of the R mutant is apparently different from that of the wild-type rHb. In the 160-850 cm^{-1} region, the most obvious distinction between two Hb species is a 4-cm^{-1} frequency shift of the ν(Fe-His) band. Besides the ν(Fe-His) frequency, the intensity of ν_8 band also provides valuable structural information on the heme pocket. The intensity of the ν_7 band of each deoxy spectrum was used as a standard and normalized to 1, and then the relative intensities of the ν_8 bands were compared, as shown in Figure 4-1C. The ν_8 band of the R mutant is obviously to be less prominent than that of the wild-type rHb.

In the 1000-1700 cm^{-1} region of the deoxy RR spectra, the frequency shifts of the ν_4 and ν_2 bands are small (slightly larger than 1 cm^{-1}) but real, which is indicated from Figure 4-1A and D. The spectra of these two Hb species were normalized according to the intensities of the ν_4 bands, and then the difference spectrum was calculated (Figure 4-1D). The derivative band shapes near 1355 cm^{-1} and 1367 cm^{-1} in the difference spectrum manifest that the frequency shifts of the ν_4 and ν_2 bands indeed exist, which agrees with previously reported data[9].

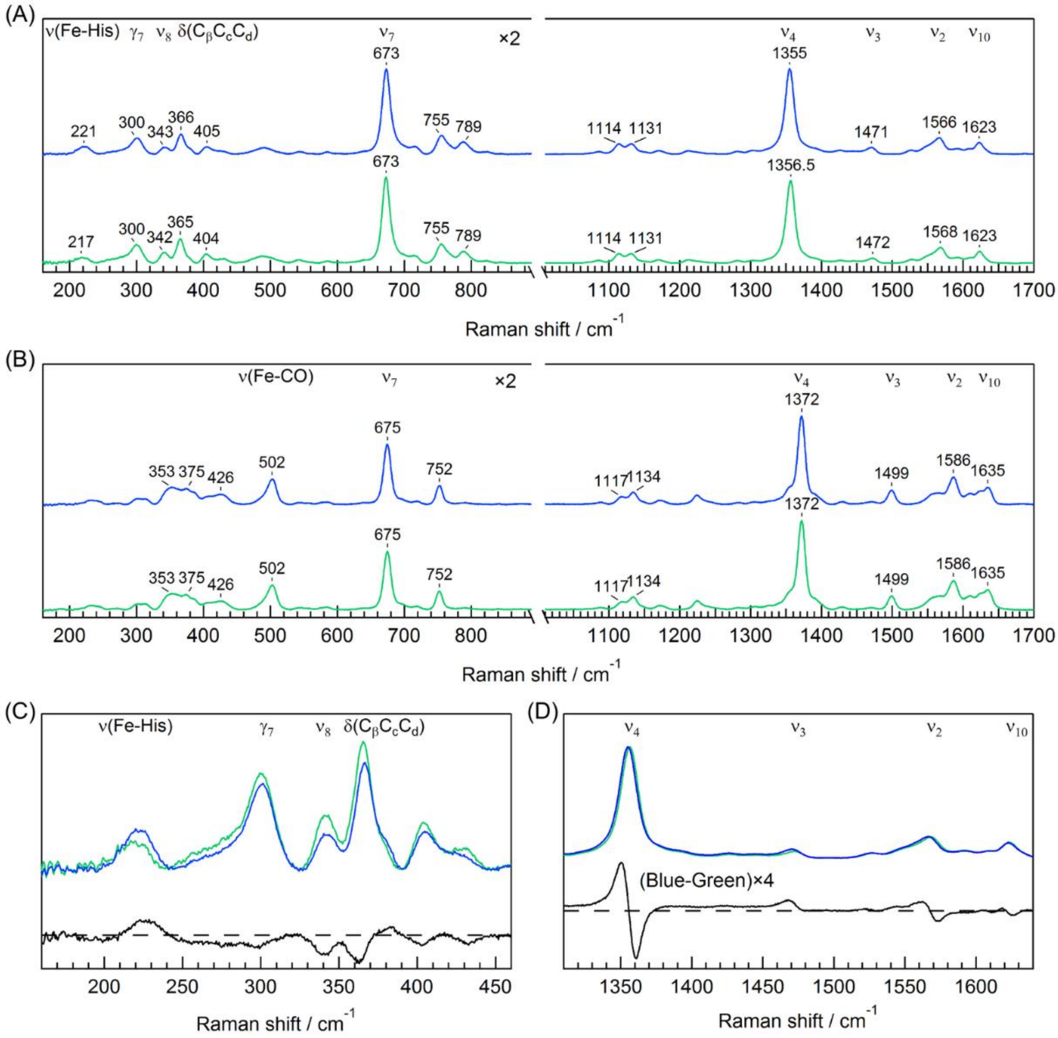

Figure 4-1. The static spectra of R mutant (blue) and wild-type rHb (green) measured in deoxy (A, C, and D) and CO-bound (B) forms. The raw spectra are shown in (A) and (B), except that the intensity of each spectrum in the 160-850 cm^{-1} region was multiplied by 2. (C) and (D) show the expanded views of the normalized deoxy spectra. The normalization methods in the 160-890 and the 1000-1700 cm^{-1} regions are to scale the intensities of the ν_7 and the ν_4 bands to 1, respectively. In addition, the black curves in (C) and (D) are the difference spectra of the blue and green spectra, and the black broken lines represent the position of zero intensity. Protein samples were dissolved in 50 mM sodium phosphate buffer, at pH 8.0. In all these panels, the accumulation time for each spectrum was 60 minutes, except for the high frequency part of the CO-bound form, which was 18 minutes.

Therefore, the frequency shifts of the ν(Fe-His), ν_4 and ν_2 bands, as well as the intensity loss of the ν_8 band, clearly reveal the difference between the deoxy R mutant and the deoxy wild-type rHb. These results consist with the data in a previous paper[9]. However, in contrast to the deoxy spectra, the static-spectra of R mutant and wild-type rHb in their CO-bound forms have no significant variations, as viewed from Figure 4-1B. This result demonstrates that the heme pockets and their environments are quite similar, if these two Hb species are in the static CO-bound forms.

4.3.1.2 Comparison of T mutant with wild-type rHb

A low pH environment is one necessary condition to keep the CO-derivative of the βN102T mutant (i.e. T mutant) stay in the T quaternary state[7]. Therefore, in this part, HEPES buffer at pH 6.4 was used to dissolve the proteins samples, which is distinctive from the buffer and pH condition used in 4.3.1.1. Since the buffer and pH condition may slightly affect the RR spectra of Hb, it is reasonable that the spectra of wild-type rHb shown in this part are not exactly the same as those shown in 4.3.1.1.

Figure 4-2A compares the static-state spectra of T mutant with wild-type rHb in their deoxy forms. The deoxy spectra of these two Hb species are quite similar, except that the ν(Fe-His) frequency seems slightly shift (1 cm^{-1}). The ν(Fe-His) frequency is the most significant marker band monitored in this study, so that it is necessary to figure out whether its frequency really shift. The expanded view of the superimposed ν(Fe-His) bands is shown in Figure 4-3A. Unfortunately, the signal-to-noise ratio of the T mutant spectrum is too low to draw a meaningful conclusion. Further effort was made. The deoxy spectra of T mutant and wild-type rHb were re-measured in another machine time (May 2015), the result of which is shown in Figure 4-3B. Since the signal-to-noise ratio was largely improved, it can be concluded from Figure 4-3B that the deoxy ν(Fe-His) frequencies of these two Hb species are almost the same. In all, the deoxy spectra of T mutant is quite similar to that of wild-type rHb.

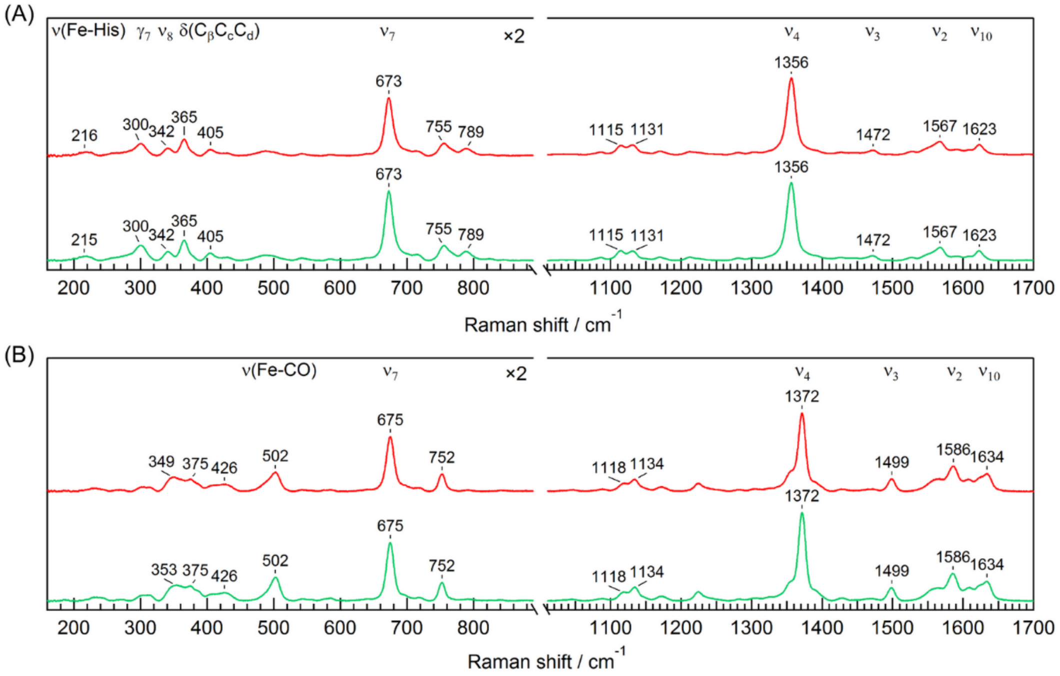

Figure 4-2. The static spectra of T mutant (red) and wild-type rHb (green) measured in deoxy (A) and CO-bound (B) forms. The intensity of each spectrum in the 160-850 cm^{-1} region was multiplied by 2. Protein samples were dissolved in 50 mM HEPES buffer, at pH 6.4. In all these panels, the accumulation time for each spectrum was 60 minutes, except for the high frequency part of the CO-bound form, which was 18 minutes.

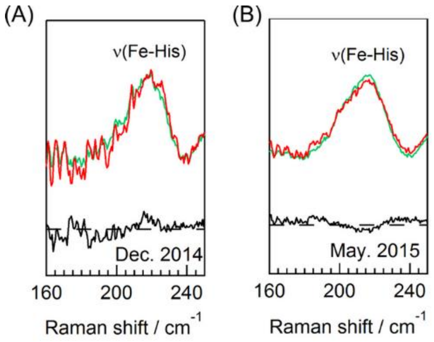

Figure 4-3. Comparison of the ν(Fe-His) bands in deoxy spectra. (A) and (B) were measured in Dec. 2014 and May 2015, respectively. Actually, (A) is an expanded view of Figure 4-2A. In each panel, the spectra of T mutant and wild-type rHb are colored in red and green, respectively. In addition, the black curve is the difference spectrum (Red-Green), and the black broken line represents the position of zero intensity. Protein samples were dissolved in 50 mM HEPES buffer, at pH 6.4. The accumulation time for each spectrum was 60 minutes.

By the way, despite that the static spectra measured in May 2015 (Figure 4-3B) obtained better resolution around the ν(Fe-His) band, the static spectra measured in Dec. 2014 are shown in Figure 4-2A, in order to make a better comparison with the time-resolved spectra measured in Dec. 2014.

Figure 4-2B compares the static-state spectra in the CO-bound forms. Only one small difference is observed, that is, the 353 cm^{-1} band downshifts to 349 cm^{-1} due to the βN102→T mutation. The seemingly large frequency shift (4 cm^{-1}) is only ascribed to a small change in symmetry of the broad 353/349 cm^{-1} band. Thus, this frequency shift has no significant implication. Therefore, it seems that the heme pocket of the CO-bound T mutant and CO-bound wild-type rHb are similar.

4.3.2 Time-resolved heme-resonant Raman spectra

Time-resolved heme-resonant Raman spectra of different Hb species at 16 delay times, ranging from -50 ns to 100 μs, were shown and compared in this section. Among all those spectra, the spectra at two specific delay times were picked out and focused on. The spectra at 30 ns characterize the structure of heme pocket and its environment right after the CO photolysis. On the contrary, the spectra at 100 μs provide the structure information of the nearly relaxed heme pocket.

At each delay time, transient spectra at two frequency regions were measured separately. In the high frequency region (1000-1700 cm^{-1}), the spectra are averages of three independent measurements; whereas in the low frequency region (160-850 cm^{-1}), the spectra are averages of ten independent measurements. These independent measurements contribute to reduce the experimental errors, so that small frequency shifts and small intensity variations are worth discussing.

4.3.2.1 Time-resolved spectra in the high frequency region

Figure 4-4 shows the time-resolved RR spectra of different Hb species following the photodissociation of CO in the high frequency region. The first two panels compare the spectra of R mutant (Figure 4-4A) with those of wild-type rHb (Figure 4-4B), and the rest two panels make a comparison between T mutant (Figure 4-4C) and wild-type rHb (Figure 4-4D). The reason that R and T mutants were measured under different buffer conditions is that the T mutant requires a low pH condition as well as the presence of IHP to maintain in T quaternary state[7]. As seen from Figure 4-4, the frequencies of the ν_4 and ν_3 bands upshifted for about 1 to 2 cm^{-1} from 30 ns to 100 μs, the extent of which is obviously larger than the other bands. Subsequently, the frequency shifts of ν_4 and ν_3 bands are inspected in detail.

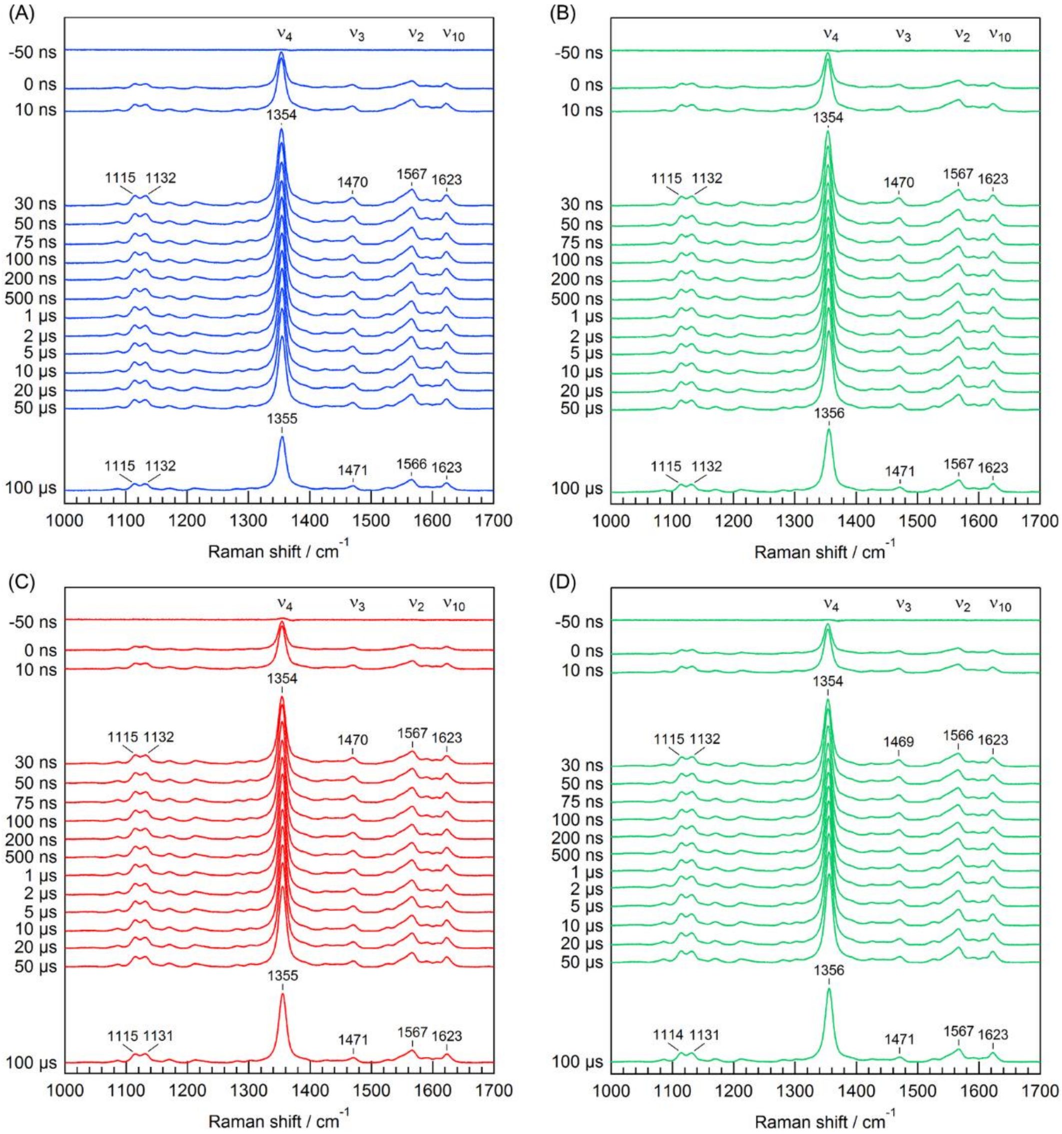

Figure 4-4. Time-resolved RR spectra of R mutant (A) and wild-type rHb (B) at pH 8.0, as well as T mutant+IHP (C) and wild-type rHb (D) at pH 6.4, in the 1000-1700 cm^{-1} region. Furthermore, (A) and (B) were measured using the 50 mM phosphate buffer, whereas (C) and (D) were obtained with the 50 mM HEPES buffer. The accumulation time for each transient spectrum was 18 minutes.

(1) Frequency shift of the ν_4 bands

The ν_4 band is an in-plane symmetric stretching mode of skeletal atoms and is often referred to as the electron density marker[10]. Upon the photodissociation of CO, the ν_4 frequency of the photoproduct has been observed to be lower than that of the stable deoxy form. The extents of the frequency shift[11] have been detected to be ~2.5, ~1.1, and ~1.8 cm^{-1} for HbA, R mutant, and Hb_{Kansas}+IHP (the same T mutant as used in this study), respectively, by comparing the 10-ns photolyzed species with their own deoxy forms. The time-resolved measurements conducted in the present study produced similar results. It should be noted that, due to instrument response of our measurement system, the intensity of 10-ns transient spectrum was low. In addition, our time-resolved results showed that the ν_4 frequencies at 10 ns and 30 ns were similar (Figure 4-5). Therefore, in our study, a comparison was carried out between the 30-ns transient spectra (Figure 4-4) with their corresponding deoxy spectra (Figure 4-1 and 4-2). For wild-type rHb, R mutant, and T mutant, the frequency shifts were observed to be ~2.5, 1.3, and 2.2 cm^{-1}, respectively.

In the present study, a careful investigation of the time dependence of the ν_4 frequency was also performed. From 30 ns to 100 μs, the ν_4 frequency was found to upshift to approach its deoxy value. However, in this time period, the total frequency shift is only ~1 to 2 cm^{-1}, not to mention the frequency difference between two adjacent time points, making it quite difficult to track the frequency variation accurately. Fortunately, a linear correlation was found to exist between the minor frequency shift of the ν_4 band and the intensity of the corresponding derivative-shaped band in the difference spectra (see Section 2.5 of Chapter 2 for detailed description). As a result, the very difficult problem of probing the frequency variation of the ν_4 band can be converted to a much easier one, that is, to track the intensity change of the derivative-shaped ν_4 band in the time-resolved difference spectra[12].

Figure 4-5 shows the time-resolved difference spectra of each Hb species. In each panel, the difference spectrum at delay time *t* was calculated based on the following equation:

$$\text{Difference spectrum } (t) = \text{Transient spectrum } (t) - \text{Transient spectrum (30 ns)} \qquad (4\text{-}1)$$

In Figure 4-5, the intensities of the derivative ν_4 bands were read, and then were multiplied by a ratio to work out the frequency shift relative to the frequency at 30 ns, that is, Δ(ν_4 frequency at 30 ns).

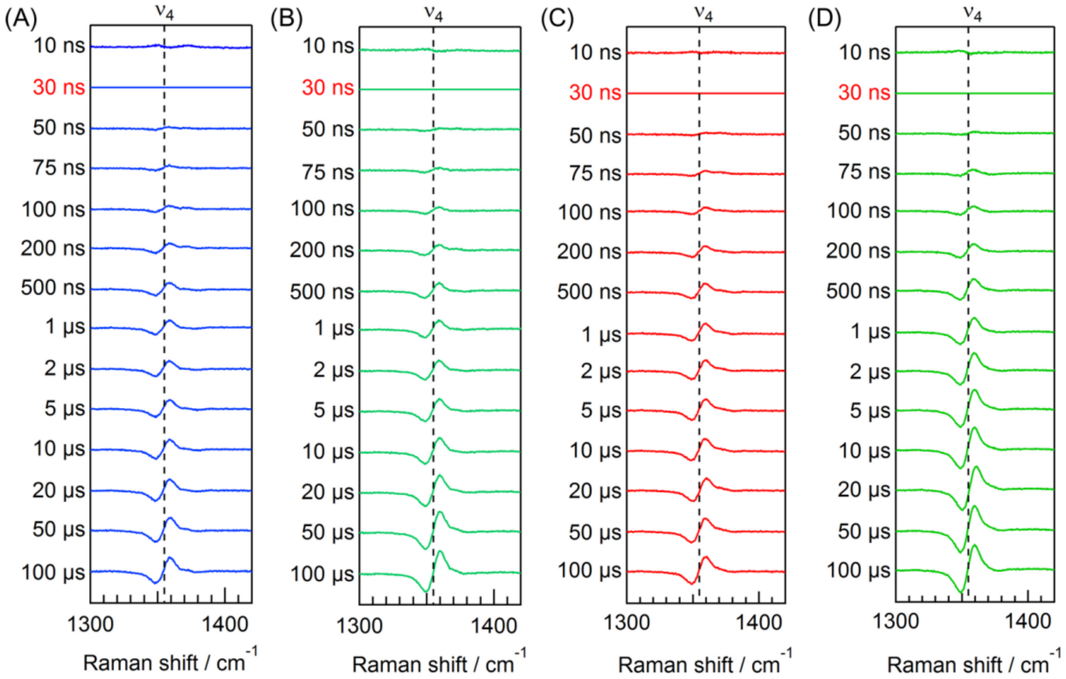

Figure 4-5. Time-resolved difference RR spectra of R mutant (A) and wild-type rHb (B) at pH 8.0, as well as T mutant+IHP (C) and wild-type rHb (D) at pH 6.4, in the 1300-1420 cm^{-1} region. In each panel, the difference spectrum at each delay time was obtained by subtracting the 30-ns transient spectrum from the transient spectrum at each delay time.

Figure 4-6 reveals the time dependence of the ν_4 frequency shift, using the ν_4 frequency at 30 ns as a reference. The standard deviations of all the data points were very small ($\sigma \approx 0.02$ cm^{-1}), except the data for the deoxy forms ($\sigma = 0.1$-0.3 cm^{-1}). This is just because the deoxy spectra were measured in the single experiments, which are separately from the time-resolved measurements.

For detailed information about the standard deviations of the "ν_4 frequency" and the "ν_4 frequency shift between two delay times", please see Section 2.5.2.2 of Chapter 2.

Back to the present section, since the standard deviations of all the "transient" data points were very small, convincible time constants can be obtained by fitting the time plots of Δ(ν_4 frequency at 30 ns). Table 4-1 summarizes all the time constants.

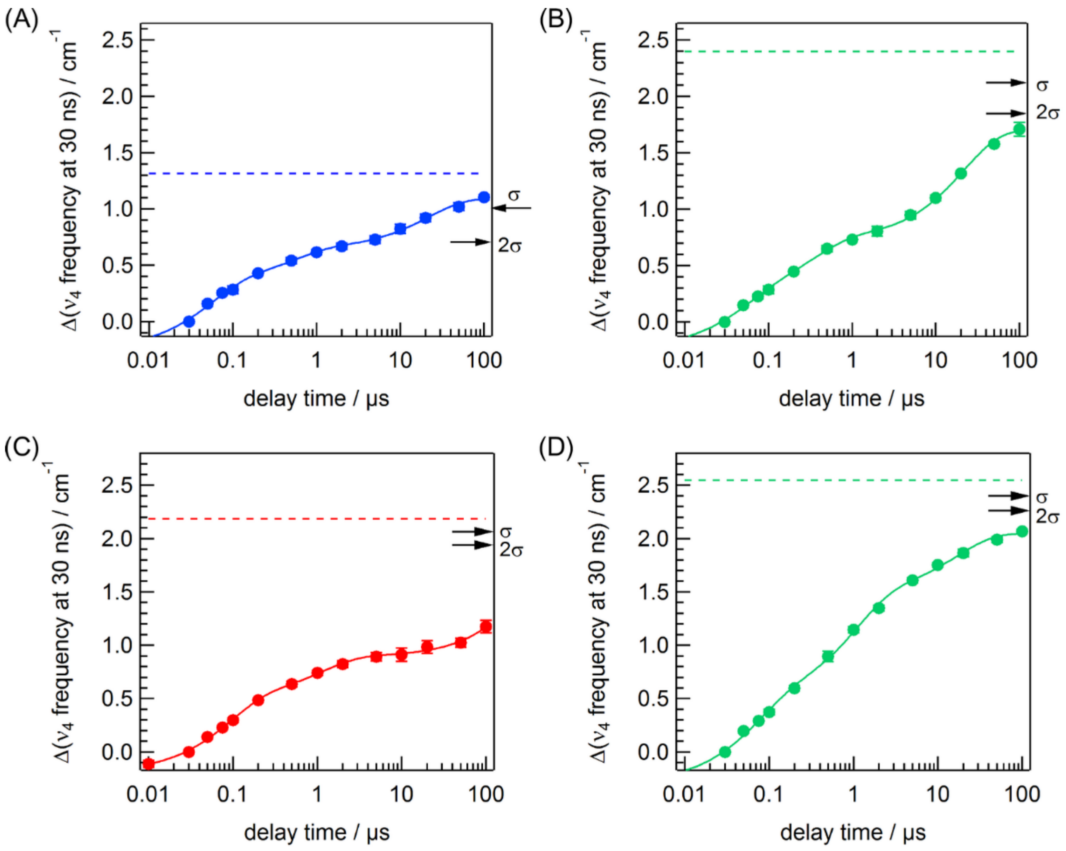

Figure 4-6. Time dependence of the ν_4 frequency shift of R mutant (A) and wild-type rHb (B) at pH 8.0, as well as T mutant+IHP (C) and wild-type rHb (D) at pH 6.4. Note that in each panel, the ν_4 frequencies were not shown in their absolute values, but their relative values to the ν_4 frequency at 30 ns. All the frequencies are averages for three independent measurements, except the frequencies for the deoxy form (broken lines). The deoxy spectra were obtained in the single measurements, so that the standard deviations of the ν_4 frequency (σ) were also shown in the figure (arrows).

Table 4-1. Time constants of temporal evolution of Δ(ν_4 frequency at 30 ns).

		τ_1 / ns	τ_2 / μs	τ_3 / μs	$-A_1$ / cm^{-1}	$-A_2$ / cm^{-1}	$-A_3$ / cm^{-1}
pH	R mutant	53±11	0.52±0.20	22±4	0.59±0.06	0.30±0.06	0.45±0.03
8.0	Wild-type rHb	49±15	0.34±0.09	22±2	0.46±0.09	0.51±0.09	0.97±0.02
pH	T mutant+IHP	89±11	1.1±0.2	440±1400	0.69±0.04	0.39±0.04	1.4±3.9
6.4	Wild-type rHb	70±13	1.0±0.2	17±4	0.77±0.07	0.98±0.08	0.58±0.07

*A_1, A_2, and A_3 are amplitudes of the frequency shift in the first, second, and third step, respectively.

At pH 8.0, from 30 ns to 100 μs, the ν_4 frequency of R mutant and of wild-type rHb increased by 1.1 and 1.7 cm^{-1}, respectively (Figure 4-6A and B). Apparently, for R mutant, the amplitude of the frequency shift is much smaller, especially in the third step, as indicated by the value of A_3 (Table 4-1). In addition, for R mutant, the ν_4 frequency at 100 μs was very similar to the deoxy frequency, indicating the completion of the ν_4 frequency shift. As for the time constants, they were indistinguishable between R mutant and wild-type rHb, within the fitting errors (Table 4-1).

At pH 6.4, the ν_4 frequency shift of T mutant was compared with that of wild-type rHb. Similar to R mutant, the total frequency shift from 30 ns to 100 μs for T mutant+IHP was 1.2 cm^{-1} (Figure 4-6C), which was also much smaller than that of wild-type rHb (2.1 cm^{-1}, Figure 4-6D). However, at 100 μs, the ν_4 frequency of T mutant+IHP was still 1 cm^{-1} lower than the deoxy frequency, suggesting that the frequency shift has not completed yet. This finding is also supported by the time constants listed in Table 4-1, *i.e.*, the values of τ_3. For wild-type rHb, the τ_3 value was within normal range; however, for T mutant+IHP, the τ_3 was surprisingly very large, 440±1400 μs.

Because the τ_3 value of T mutant+IHP exceeds the largest delay time (100 μs), I did another experiment and added two delay times, that is, 200 and 350 μs. It is impossible to further extend the delay time, due to the limitation of the experimental method. Another thing to be noted is that, since the amount of protein sample of T mutant was not sufficient, the accumulation time for each transient spectra in the new experiment was only 6 minutes. With two new data points, Figure 4-6C turns into Figure 4-7, meanwhile, the new time constants were shown in Table 4-2. Now, the error from the fitting procedure was largely reduced, making the value of τ_3 more reliable. Therefore, it is indicated that τ_3 value of the ν_4 frequency shift is increased by one order of magnitude, if Hb is at all times constrained in T quaternary structure.

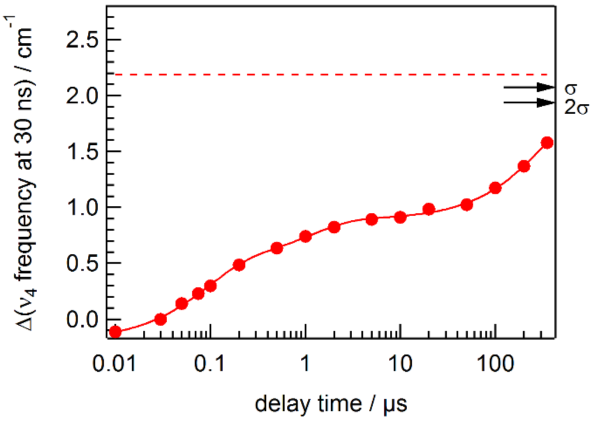

Figure 4-7. Time dependence of the ν_4 frequency shift of T mutant+IHP at pH 6.4, after adding two additional time points. Other descriptions of this figure are the same as Figure 4-5.

Table 4-2. Time constants of temporal evolution of Δ(ν_4 frequency at 30 ns) after extending the delay time to 350 μs.

		τ_1 / ns	τ_2 / μs	τ_3 / μs	$-A_1$ / cm^{-1}	$-A_2$ / cm^{-1}	$-A_3$ / cm^{-1}
pH 6.4	T mutant+IHP	89±9	1.1±0.2	320±60	0.69±0.04	0.39±0.04	1.0±0.1

From Figure 4-5 to 4-7, the time dependence of ν_4 frequency shift of each Hb species were studied independently. Next, in Figure 4-8, the ν_4 frequency differences between Hb mutants and wild-type rHb at each delay were investigated. In panel (A) and (B), the difference spectrum at delay time *t* were calculated based on the following equations, respectively:

Difference spectrum (*t*, pH 8.0) = Transient spectrum of R mutant (*t*, pH 8.0)

– Transient spectrum of wild-type rHb (*t*, pH 8.0)   (4-2)

Difference spectrum (*t*, pH 6.4) = Transient spectrum of T mutant+IHP (*t*, pH 6.4)

– Transient spectrum of wild-type rHb (*t*, pH 6.4)   (4-3)

ν_4 frequency differences between either Hb mutant and the wild-type rHb were calculated from the intensities shown in panels (A) and (B), and then plotted in panels (C) and (D), respectively. Because the spectra of Hb mutants and wild-type rHb were measured in separate experiments, the standard deviations of "ν_4 frequency" (σ = 0.1-0.3 cm^{-1}) must be taken into account, shown as broken lines in panels (C) and (D).

At pH 8.0, the ν_4 frequencies of R mutant and wild-type rHb were similar until 20 μs. However, from 50 μs, the ν_4 frequency of R mutant became lower than that of wild-type rHb.

At pH 6.4, the ν_4 frequency of T mutant+IHP was higher than that of wild-type rHb until 0.5 μs. From 1 μs to 10 μs, the frequencies between these two Hb species seems to be similar within the experimental error. From 20 μs to 100 μs, the frequency of T mutant+IHP was slightly lower than that of wild-type rHb.

The variation of ν_4 frequency difference between either Hb mutant and wild-type rHb is surprisingly reversely correlated with the temporal behavior of ν(Fe-His) frequency difference (section 4.3.2.2). This interesting finding will be discussed in section 4.4.*.

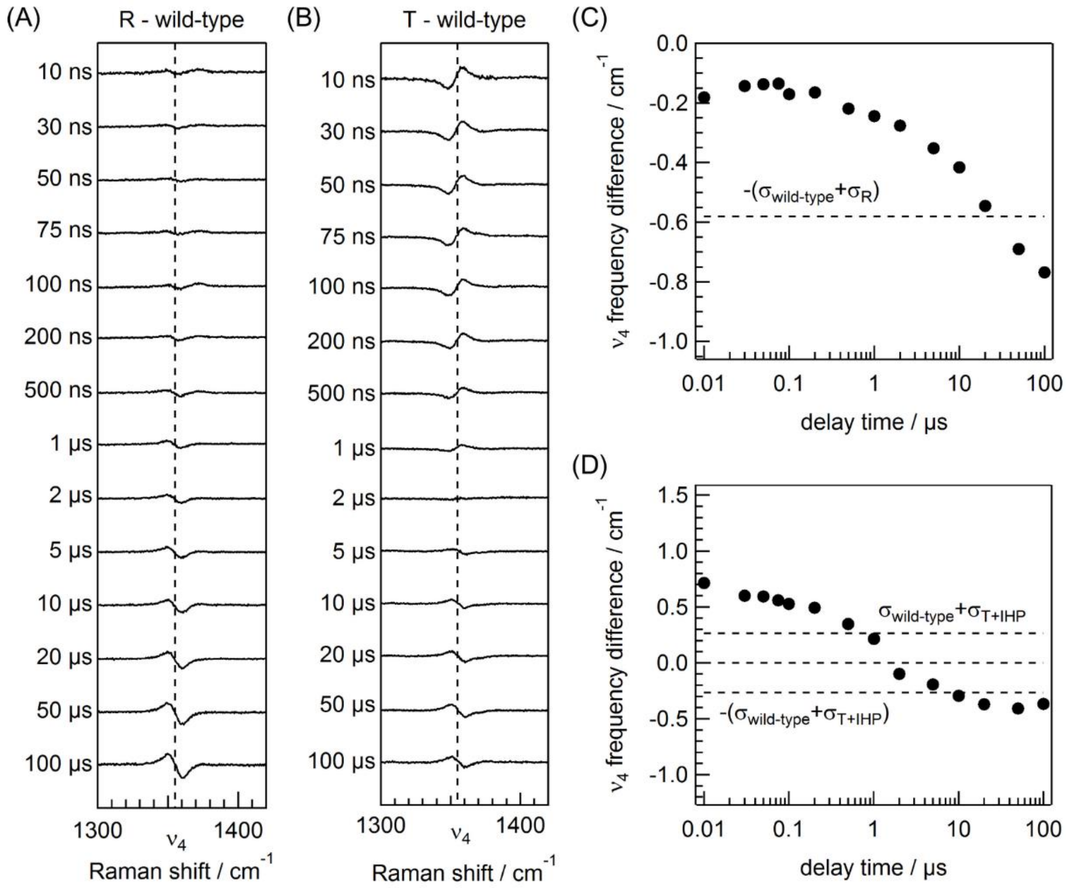

Figure 4-8. Time-resolved difference RR spectra between R mutant and wild-type rHb at pH 8.0 (A), as well as between T mutant+IHP and wild-type rHb at pH 6.4 (B), in the 1300-1420 cm^{-1} region. (C) and (D) are time plots of ν_4 frequency difference, which were derived from (A) and (B), respectively.

(2) Frequency shift of the ν_3 bands

The porphyrin core of heme is defined as the distance between the four pyrrole nitrogen atoms. Typically, the distance between a pyrrole nitrogen atom and the heme center is used to monitor the core size. It has been proved that the frequency of ν_3 band is sensitive to the core size[13], with a high sensitivity[14] of ~0.002 Å/cm^{-1}. Consequently, small shift in ν_3 frequency predicts important structural information. The upshift of the ν_3 represents the contract of core size, otherwise, the downshift means the core size is expanded.

It has been established that the core size of the deoxy Hb is more expanded compared to CO-bound form. In addition, the core size of the HbCO photoproduct is not in the middle, but rather more expanded than deoxy Hb. Set the ν_3 frequency variation of wild-type rHb as an example (Figure 4-1 and 4-3). At pH 8.0, the frequencies in CO-bound spectrum was 1499 cm^{-1}. Soon after the photolysis of CO (30 ns), the frequency downshift to 1470 cm^{-1}, totally by ~30 cm^{-1}. Then from 30 ns to the fully relaxed deoxy state, the frequency slightly upshift to 1472 cm^{-1}, only by ~2 cm^{-1}.

In the present study, we compared the ν_3 frequency shift of different Hb species, trying to figure out if the quaternary structure influence the core size. The expanded time-resolved spectra near ν_3 band are shown in Figure 4-9, note that the whole spectra were normalized according to the intensity of ν_4 band. It is obvious that, during this time period, the frequency of ν_3 band upshift, concomitantly, the band intensity slightly decreased (Figure 4-9A and B). Since the intensity loss has little significance, we only focus on the frequency shift.

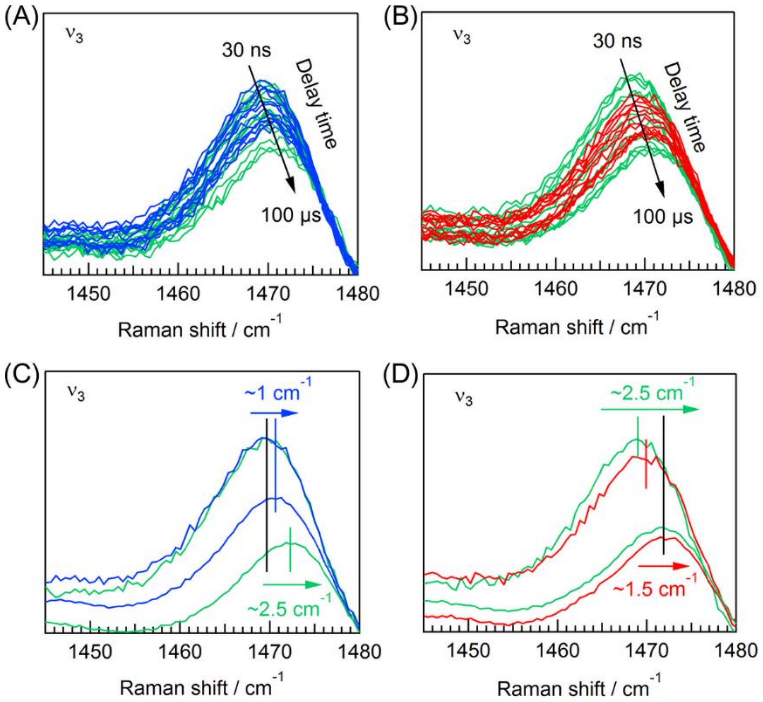

Figure 4-9. RR spectra near ν_3 band. (A) and (B) show the time-resolved spectra from 30 ns to 100 μs, while (C) and (D) compare the spectra at 30 ns with the static deoxy spectra. Spectra in (A) and (C) were measured at pH 8.0, and those in (B) and (D) were measured at pH 6.4. In this figure, blue, red, and green curves represent the spectra of R mutant, T mutant+IHP, and wild-type rHb, respectively.

As seen in Figure 4-9C, at 30 ns, the ν_3 frequencies of R mutant and wild-type rHb were very similar. However, from 30 ns to the fully relaxed deoxy state, the ν_3 frequency of R mutant only varied by ~1 cm^{-1}, which was smaller than that of wild-type rHb (~2.5 cm^{-1}). These results indicate that the R quaternary structure constrains the core size from fully contraction.

On the contrary, in the case of T mutant+IHP, the situation is opposite (Figure 4-8B and D). At 30 ns, the ν_3 frequency of T mutant+IHP was 1 cm^{-1} larger compared with wild-type rHb. However, at the static deoxy state, the ν_3 frequency of T mutant+IHP was similar to that of wild-type rHb. Consequently, it seems that the T quaternary structure prefers a more contracted core size.

In summary, it is interesting to observe that the quaternary structure has influence on the core size: the R quaternary structure prefers a relatively expanded core size, whereas the T quaternary structure seems to make the core size more contracted.

4.3.2.2 Time-resolved spectra in the low frequency region

Experiments in this section mainly fall into three parts: (1) compare R mutant with wild-type rHb at pH 8.0; (2) compare T mutant+IHP with wild-type rHb at pH 6.4; and (3) study the influence of IHP on the dynamics of wild-type rHb at pH 6.4. In each part, time dependence of the ν(Fe-His) frequency, as well as of the ν_8 intensity, was investigated to monitor the time course of structural changes of each rHb species, using the same method as mentioned in Section 3.2.2.

Experiments in this section were conducted in three separate machine times, as listed in Table 4-3. It is worth noting that only the data obtained in the same machine time can be compared directly.

Table 4-3. Summarization of the Raman measurements in the low frequency region.

Machine time	pH	species	Number of independent measurements	Accumulation time / min
Nov. 2014	8.0	R mutant Wild-type rHb	10	60
	6.4	T mutant+IHP Wild-type rHb	10	60
May 2015	6.4	T mutant+IHP	2[a]	28
		Wild-type rHb	2[a]	28
		T mutant	3	18
Jul. 2015	6.4	Wild-type rHb	5	30
		Wild-type rHb+IHP	5	30

[a] There were only 7 delay times, not 16 delay times in other measurements. As a result, in each single measurement, the transient spectrum at each delay time was accumulated for 14 minutes.

(1) Compare R mutant with wild-type rHb at 8.0

Figure 4-10 shows the time-resolved RR spectra of R mutant (A) and wild-type rHb (B) following the photodissociation of CO in the low frequency region. The spectra of these two Hb species at 30 ns were very similar. However, the spectra at 100 μs showed some differences, particularly in the ν(Fe-His) and ν_8 bands.

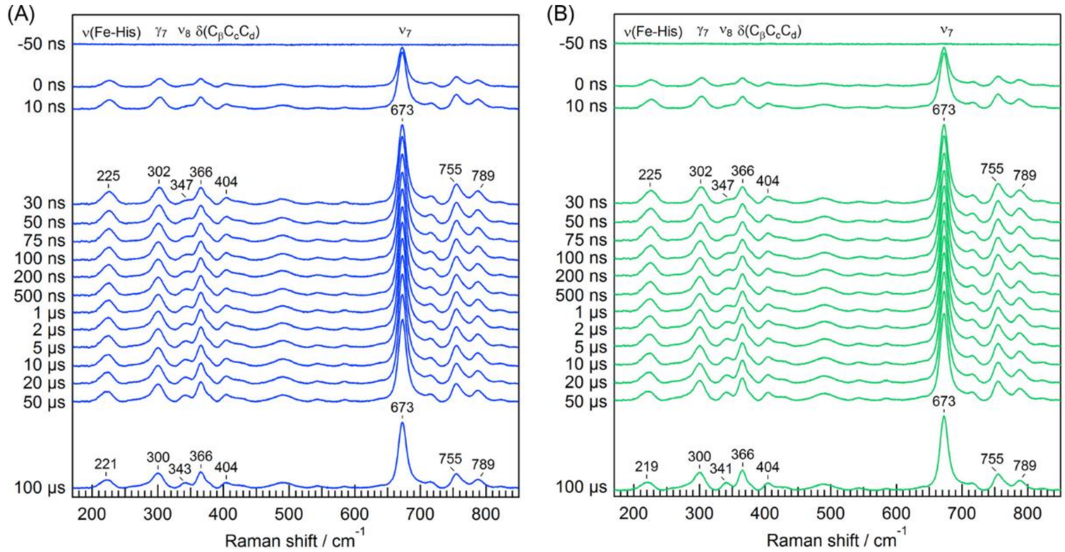

Figure 4-10. Time-resolved RR spectra of R mutant (A) and wild-type rHb (B) at pH 8.0 in the 170-850 cm^{-1} region. Spectra were measured using the 50 mM phosphate buffer. The accumulation time for each transient spectrum was 60 minutes.

The expanded view of the time-resolved spectra near the ν(Fe-His) and ν_8 bands are shown in Figure 4-11. Besides that, the time plots of ν(Fe-His) frequency and ν_8 bands are shown in Figure 4-12. Table 4-4 summarizes all the time constants. Obviously, there was no significant difference between R mutant and wild-type rHb until ~50 μs. Almost from the same time (~50 μs), the data of R mutant approached their deoxy values, indicating that the tertiary structural changes under R quaternary structure complete within 50 μs.

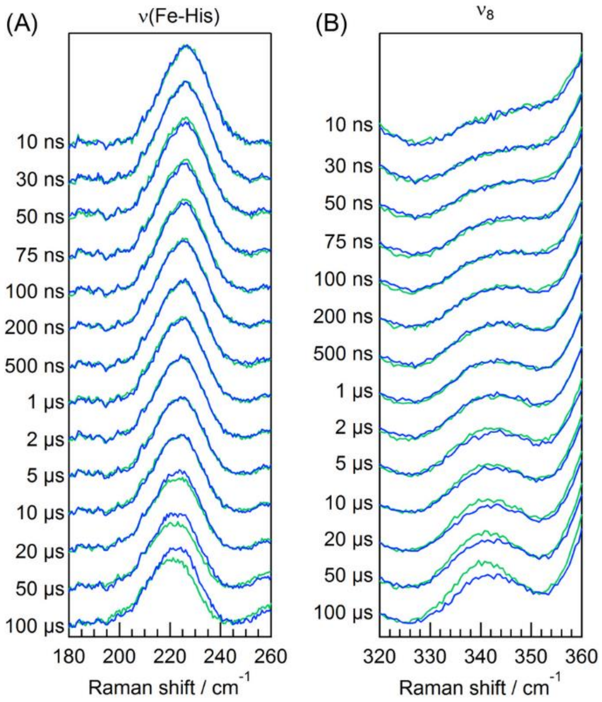

Figure 4-11. Expanded time-resolved RR spectra of R mutant (blue) and wild-type rHb (green) in the 180-260 (A), and 320-360 (B) cm^{-1} region. Note that all the spectra were normalized according to the intensity of the ν_7 band.

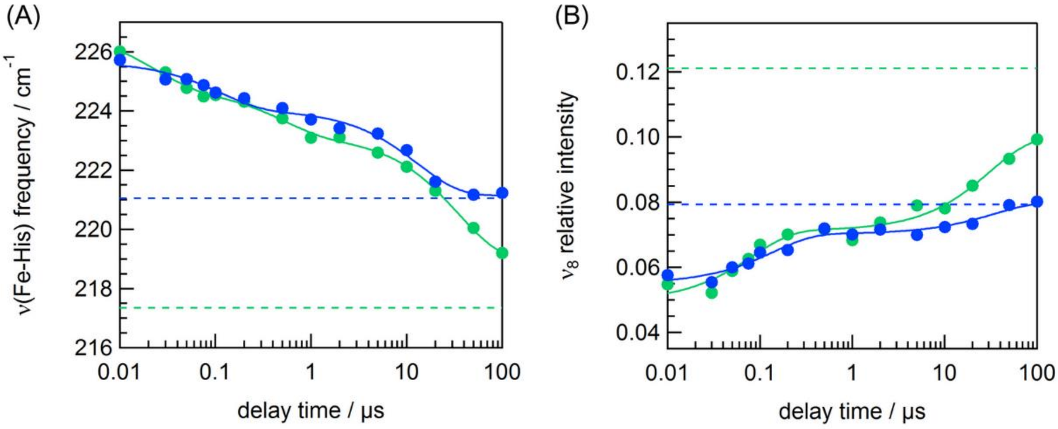

Figure 4-12. Time dependence of the ν(Fe-His) frequency (A) and of the ν_8 relative intensity (B). The blue and green colors represent R mutant and wild-type rHb, respectively. The solid curves indicate the best fit obtained using a sum of exponential functions. The broken lines show the values for the deoxy forms, which were obtained in the single measurements.

Table 4-4. Time constants of temporal evolution of Raman bands.

		τ_1 / ns	τ_2 / μs	τ_3 / μs	A_1 / cm^{-1}	A_2 / cm^{-1}	A_3 / cm^{-1}
ν(Fe-His)	R mutant		0.11±0.03	13±2		1.6±0.2	2.9±0.2
	Wild-type rHb	23±8	0.49±0.14	35±5	2.0±0.3	1.6±0.2	4.2±0.2

		τ_4 / ns	τ_5 / μs	A_4 * 1000	A_5 * 1000
ν_8	R mutant	140±40	51±39	15±2	12±4
	Wild-type rHb	82±25	31±10	22±3	29±3

(2) Compare T mutant+IHP with wild-type rHb at 6.4

Figure 4-13 shows the time-resolved RR spectra of T mutant+IHP and wild-type rHb following the photodissociation of CO in the low frequency region. It was unexpected that, at 100 μs, the ν(Fe-His) frequency of T mutant+IHP was higher as compared with wild-type rHb, suggesting that it did not approach the deoxy value. Therefore, an extra experiment was conducted to extend the delay time to 350 μs.

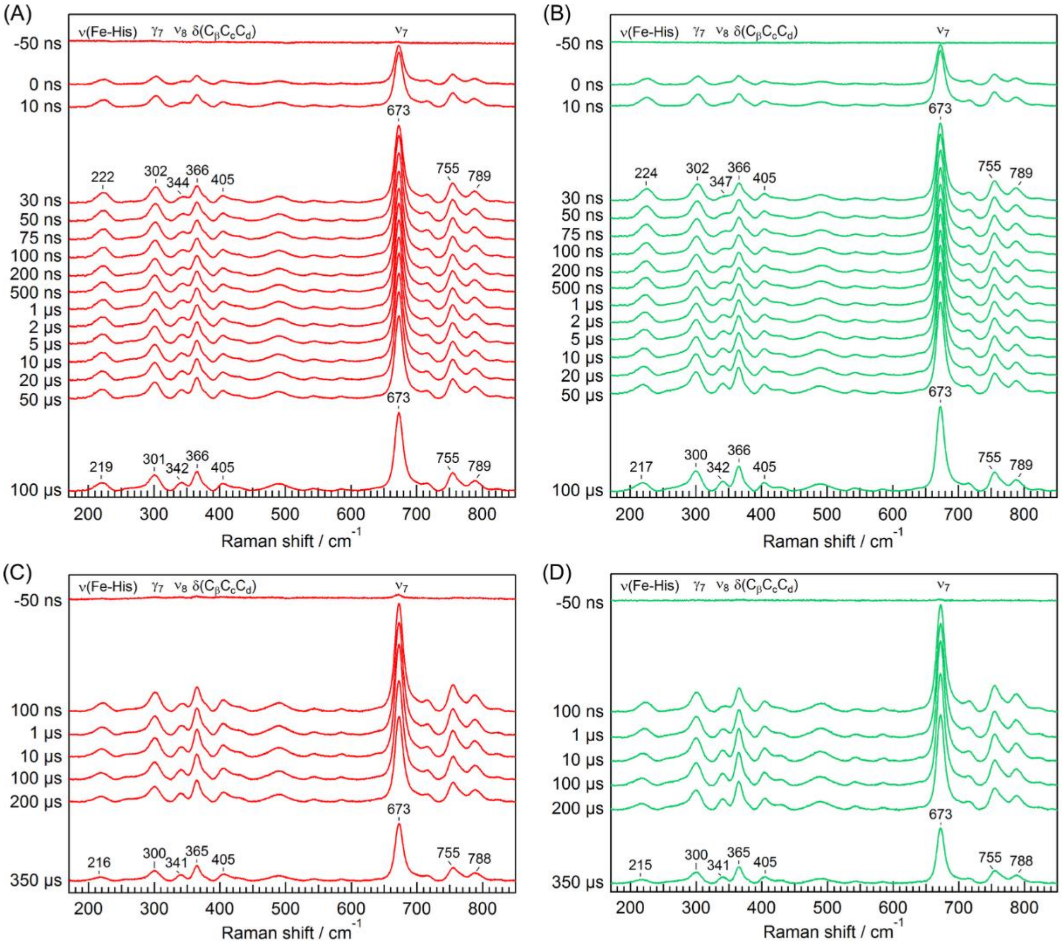

Figure 4-13. Time-resolved RR spectra of T mutant+IHP (red) and wild-type rHb (green) at pH 6.4 in the 170-850 cm^{-1} region. Spectra were measured using the 50 mM HEPES buffer. (A) and (B) were measured in the same machine time, with the accumulation time of 60 minutes for each spectrum. (C) and (D) were measured in another machine time, with the accumulation time of 28 minutes for each spectrum.

The expanded view of the time-resolved spectra are shown in Figure 4-14, meanwhile, the time plots were shown in Figure 4-15. The former visualize the difference between T+mutant and wild-type rHb, while the latter analyze the data using mathematical methods.

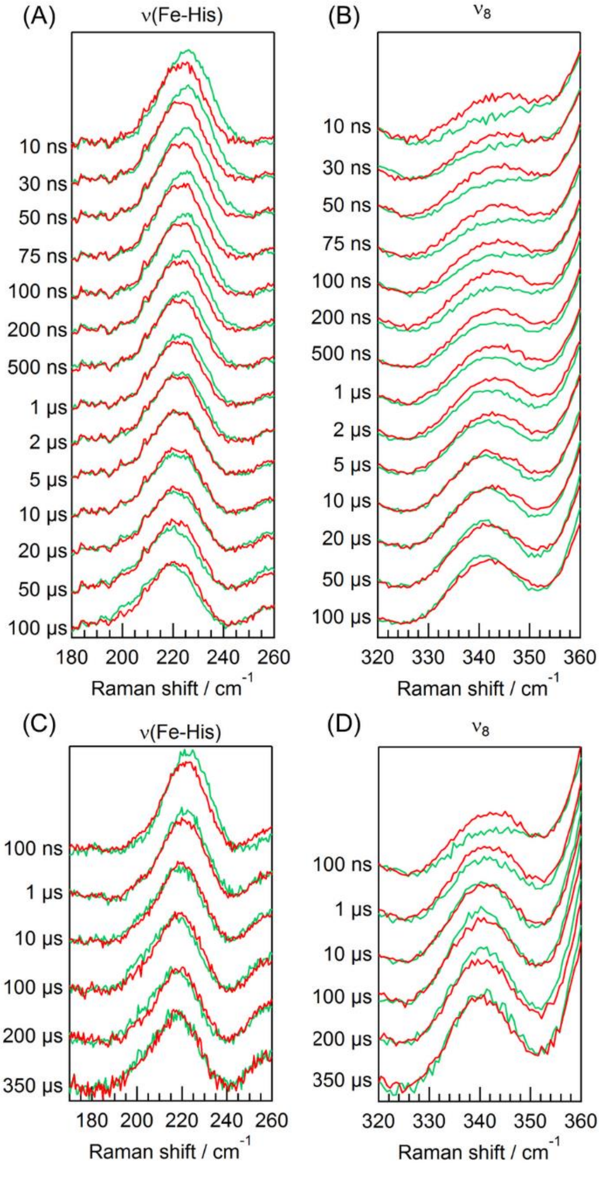

Figure 4-14. Expanded time-resolved RR spectra of T mutant+IHP (red) and wild-type rHb (green) in the 180-260 (A), and 320-360 (B) cm^{-1} region. Note that all the spectra were normalized according to the intensity of the ν_7 band. (A) and (B) were measured in the same machine time, while (C) and (D) were measured in another machine time.

The temporal behavior of the ν(Fe-His) frequency is discussed first. At 30 ns, the frequency of T mutant+IHP was lower (Figure 4-14A and 4-15A). From 30 ns to 100 μs, the frequency of T mutant+IHP only decreased by 2.5 cm^{-1}, which was much smaller than the frequency shift of wild-type rHb (7 cm^{-1}) during the same period. At 100 μs, the frequency shift of wild-type rHb had already completed (Figure 4-15C). However, at the same time, the frequency of T mutant+IHP was 2 cm^{-1} higher than wild-type rHb. The time constants corresponded to Figure 4-14A were shown in Table 4-5. At this stage, only two time components were detected for T mutant+IHP.

As shown in Figure 4-14C and 4-15C, the frequency of T mutant+IHP was still higher at 200 μs. However, at 350 μs, the frequencies of these two Hb species were similar. Although it is impossible to calculate reliable time constants based on only six points, it seems reasonable that the third time constant of T mutant+IHP was several hundreds of microseconds, which is abnormally larger for tertiary structural changes.

The temporal behavior of ν_8 intensity were similar with ν(Fe-His) frequency, also predicting a time constant of several hundreds of microseconds, as seen from Figure 4-14D and 4-15D.

One possible explanation for this abnormally larger time constant is that it is due to the influence of IHP. To check this explanation, the effect of IHP on wild-type rHb were investigated. Results are shown in the next part.

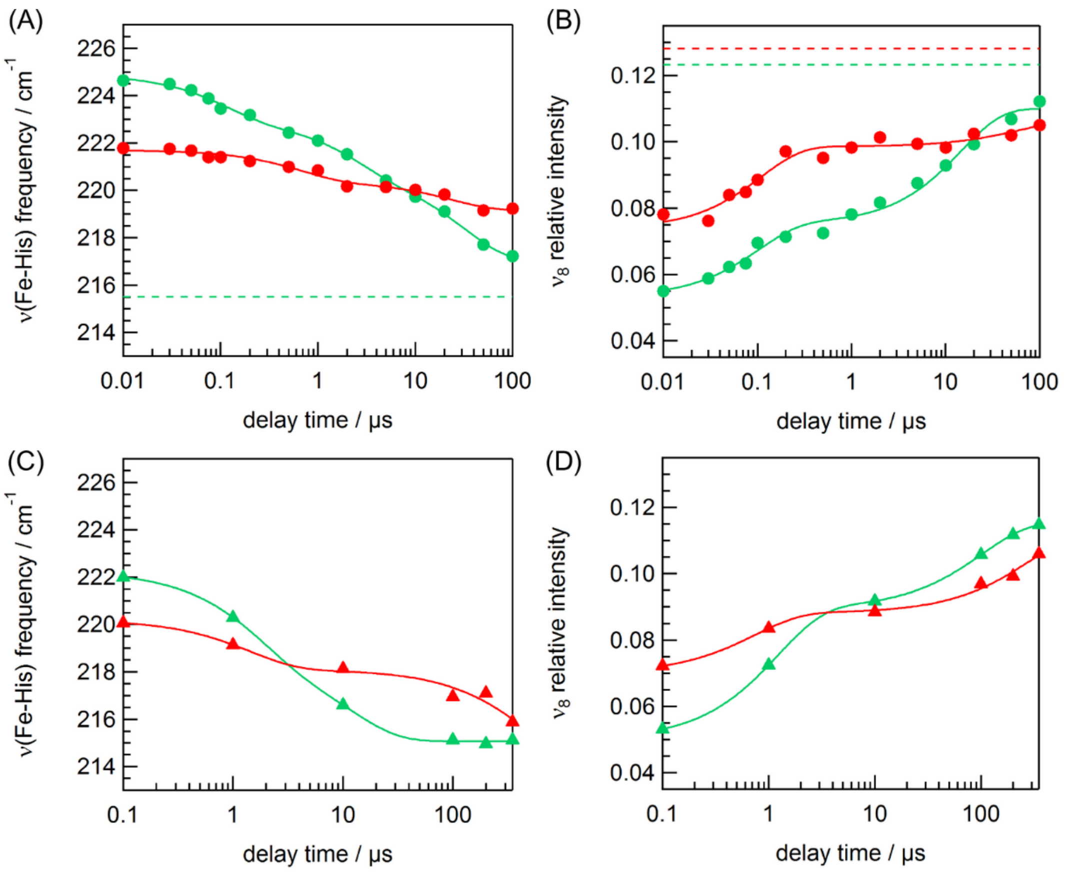

Figure 4-15. Time dependence of the ν(Fe-His) frequency (A, C) and of the ν_8 relative intensity (B, D). The red and green colors represent T mutant and wild-type rHb, respectively. Other descriptions are similar as Figure 4-12.

Table 4-5. Time constants of temporal evolution of Raman bands.

		τ_1 / ns	τ_2 / μs	τ_3 / μs	A_1 / cm^{-1}	A_2 / cm^{-1}	A_3 / cm^{-1}
ν(Fe-His)	T mutant+IHP		0.68±0.25	24±12		1.3±0.2	1.2±0.2
	Wild-type rHb	110±30	2.4±0.8	32±7	1.9±0.2	2.2±0.3	3.7±0.3

		τ_4 / ns	τ_5 / μs	A_4 * 1000	A_5 * 1000
ν_8	T mutant+IHP	110±26	56±110	25±3	7±7
	Wild-type rHb	102±28	15±3	22±3	35±2

(3) The influence of IHP on the dynamics of wild-type rHb at pH 6.4

This part is to check the effect of IHP on dynamics of wild-type rHb. Time-resolved RR spectra are shown in Figure 4-16. At 30 ns, the presence of IHP slightly lowered the ν(Fe-His) frequency. In contrast, at 100 μs, IHP has little effect on the RR spectrum.

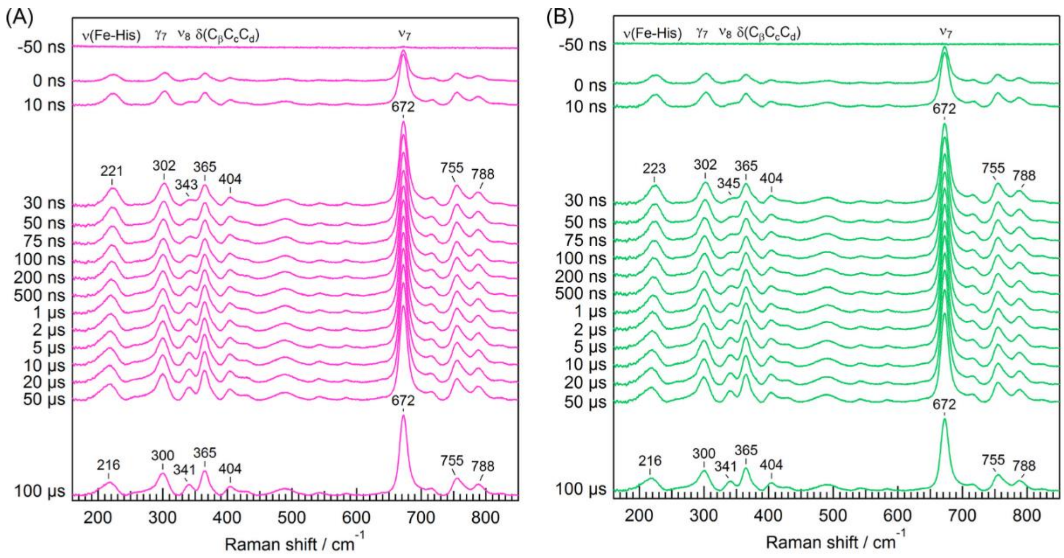

Figure 4-16. Time-resolved RR spectra of Wild-type rHb+IHP (pink) and wild-type rHb (green) at pH 6.4 in the 170-850 cm^{-1} region. Spectra were measured using the 50 mM HEPES buffer. The accumulation time for each transient spectrum was 30 minutes.

Expanded time-resolved spectra near the ν(Fe-His) and the ν_8 bands are shown in Figure 4-17. It is clear that, from 30 ns to 10 μs, the influence of IHP is to slightly lower the ν(Fe-His) frequency, as well as increase the ν_8 intensity. After 20 μs, IHP has no significant effect.

In all, results in this part demonstrated that the presence of IHP did not slow the structural change of rHb.

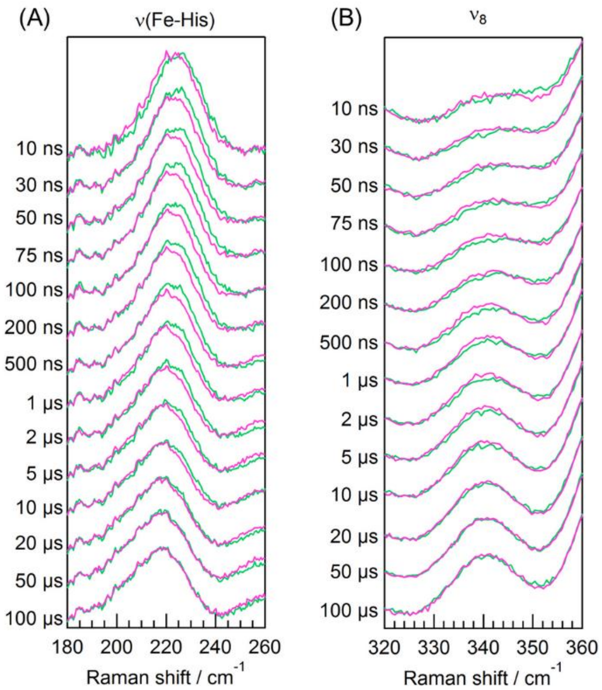

Figure 4-17. Expanded time-resolved RR spectra of Wild-type rHb+IHP (pink) and wild-type rHb (green) in the 180-260 (A), and 320-360 (B) cm^{-1} region. Note that all the spectra were normalized according to the intensity of the ν_7 band.

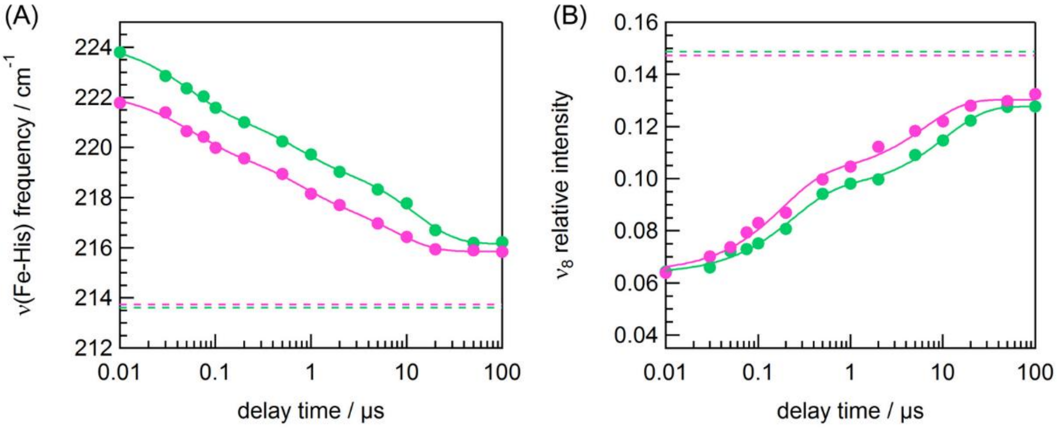

Figure 4-18. Time dependence of the ν(Fe-His) frequency (A) and of the ν_8 relative intensity (B). The pink and green colors represent wild-type rHb in the presence and without IHP, respectively. Other descriptions are similar as Figure 4-12.

4.4 Discussion

4.4.1 Dynamics of the tertiary structural changes

The original purpose of this study is to investigate the dynamics of tertiary structural changes, if the quaternary structure of Hb is fixed. To achieve this, I mutated the wild-type rHb into two Hb mutants. One mutant is restricted in R quaternary state, so that it is called R mutant in this thesis. The other mutant is constrained in T quaternary state in the presence of IHP, consequently, it is donated as T mutant+IHP.

For each Hb mutant, no quaternary structural change occurs after the photodissociation of CO. Therefore, the time constants only represent the dynamics of tertiary structural changes. In this study, three marker bands were used to determine the time constants, that is, the ν_4 band in the high frequency region, as well as the ν(Fe-His) and ν_8 bands in the low frequency region. Similar conclusions can be drew from the time dependence of these three bands.

Our results indicated that the tertiary structural changes within the R quaternary state is completed with the time constant of ~10-50 μs. Nevertheless, the situation is more complicated for T mutant+IHP. The tertiary structural changes do not completed until at ~350 μs. This is to say, the time constant of T mutant+IHP is one order of magnitude larger as compared with the R mutant.

4.4.2 Influence of quaternary states on the size of the porphyrin core

An interesting observation of my research is that the quaternary structure has remarkable influence on the core size: the R quaternary structure prefers a relatively expanded core size, whereas the T quaternary structure seems to make the core size more contracted.

The expansion or contraction of the core size is controlled by the tertiary structure of the nearby residues, which constitutes the heme binding pocket. Therefore, the results of the core size imply that the tertiary structure of the heme pocket is different between R and T quaternary states.

This conclusion may provide an explanation for the deceleration of the tertiary structural changes within T quaternary state.

4.4.3 Inverse correlation between ν(Fe-His) and ν_4 in the time evolution data

It has been demonstrated that there is a linear inverse correlation between the frequency of ν(Fe-His) and of ν_4 for both steady state[9] and 10-ns photolyzed[15] species of Hb. However, earlier studies (in 1980s) stated that this correlation is lost in the time evolution data[16]. Now, over 30 years have passed. As technology advances, more reliable conclusion can be drawn regarding the correlation between the temporal evolution of ν(Fe-His) and of ν_4.

In the "Results" part, the temporal behavior of ν(Fe-His) and of ν_4 have been examined independently. Figure 4-19 shows the linearly inverse correlation between the frequency of ν(Fe-His) and of ν_4 for each rHb species. Table 4-6 summarizes the fitting parameters. From these data it appears that the inverse correlation between the frequency of ν(Fe-His) and of ν_4 almost holds at every delay time, especially for the data measured at pH 8.0 (Panels A).The values of R^2 all exceeded 0.9, implying that there is a direct link between the behavior of the Fe-His stretching mode and the distribution of electrons within the π system of porphyrin.

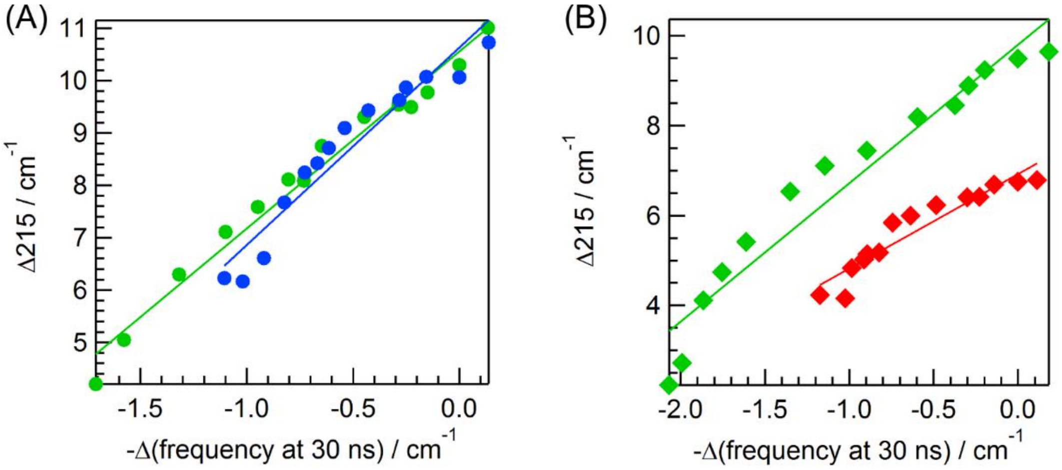

Figure 4-19 The inverse correlation between the frequency of ν(Fe-His) and of ν_4 for photolyzed species of rHb. (A) shows the data of R mutant (Blue) and Wild-type rHb (green) at pH 8.0, while (B) plots the data of T mutant+IHP (red) and wild-type rHb (green) at pH 6.4.

Table 4-6. Summarization of the fitting parameters

pH	species	-Δ215 / Δ(frequency at 30 ns)	R^2
8.0	R mutant	3.8±0.3	0.93
	Wild-type rHb	3.4±0.1	0.98
6.4	T mutant+IHP	2.1±0.2	0.90
	Wild-type rHb	3.1±0.2	0.94

4.5 Conclusions

In this study, we examined in detail the temporal behavior of time-resolved RR spectra of the R mutant and T mutant+IHP, as compared with wild-type rHb. The results revealed that the tertiary structural changes within R quaternary state completed with the time constant of ~10-30 μs. However, the tertiary structural changes within T quaternary state were slowed down by one order of magnitude. We also observed that the core size is difference between R and T quaternary states, indicating that the tertiary structure of heme pocket is also distinct between R and T quaternary states. This observation may provide a possible explanation for the deceleration of structural changes within T quaternary structure. Another important finding is that the frequency of ν(Fe−His) and of ν_4 were shown to be linearly inverse correlated in the time-evolution data. These findings help further characterize the protein dynamics regulating the allosteric pathway of Hb.

References

1. Monod, J.; Wyman, J.; Changeux, J. P., *Journal of Molecular Biology* **1965,** *12* (1), 88-118.

2. Viappiani, C.; Abbruzzetti, S.; Ronda, L.; Bettati, S.; Henry, E. R.; Mozzarelli, A.; Eaton, W. A., *Proceedings of the National Academy of Sciences of the United States of America* **2014,** *111* (35), 12758-12763.

3. Jones, E. M.; Balakrishnan, G.; Spiro, T. G., *Journal of the American Chemical Society* **2012,** *134* (7), 3461-3471.

4. Thom, C. S.; Dickson, C. F.; Gell, D. A.; Weiss, M. J., *Cold Spring Harbor Perspectives in Medicine* **2013,** *3* (3).

5. Reissmann, K.; Ruth, W. E.; Nomura, T., *Journal of Clinical Investigation* **1961,** *40* (10), 1826-1833.

6. Reed, C. S.; Hampson, R.; Gordon, S.; Jones, R. T.; Novy, M. J.; Brimhall, B.; Edwards, M. J.; Koler, R. D., *Blood* **1968,** *31* (5), 623-632.

7. Kilmartin, J. V.; Anderson, N. L.; Ogawa, S., *Journal of Molecular Biology* **1978,** *123* (1), 71-87; Ogawa, S.; Shulman, R. G.; Mayer, A., *Biochemical and Biophysical Research Communications* **1972,** *49* (6), 1485-1491.

8. Shen, T. J.; Ho, N. T.; Zou, M.; Sun, D. P.; Cottam, P. F.; Simplaceanu, V.; Tam, M. F.; Bell, D. A.; Ho, C., *Protein Engineering* **1997,** *10* (9), 1085-1097.

9. Ondrias, M. R.; Rousseau, D. L.; Shelnutt, J. A.; Simon, S. R., *Biochemistry* **1982,** *21* (14), 3428-3437.

10. Spiro, T. G.; Burke, J. M., *Journal of the American Chemical Society* **1976,** *98* (18), 5482-5489.

11. Friedman, J. M.; Stepnoski, R. A.; Stavola, M.; Ondrias, M. R.; Cone, R. L., *Biochemistry* **1982,** *21* (9), 2022-2028.

12. Laane, J.; Kiefer, W., *Journal of Chemical Physics* **1980,** *72* (10), 5305-5311; Laane, J., *Journal of Chemical Physics* **1981,** *75* (6), 2539-2545.

13. Spiro, T. G.; Stong, J. D.; Stein, P., *Journal of the American Chemical Society* **1979,** *101* (10), 2648-2655; Choi, S.; Spiro, T. G.; Langry, K. C.; Smith, K. M.; Budd, D. L.; Lamar, G. N.,

Journal of the American Chemical Society **1982,** *104* (16), 4345-4351.

14. Spaulding, L. D.; Chang, C. C.; Yu, N. T.; Felton, R. H., *Journal of the American Chemical Society* **1975,** *97* (9), 2517-2525.

15. Friedman, J. M.; Rousseau, D. L.; Ondrias, M. R., *Annual Review of Physical Chemistry* **1982,** *33*, 471-491.

16. Sassaroli, M.; Rousseau, D. L., *Biochemistry* **1987,** *26* (11), 3092-3098.

Chapter 5 Conclusion

Allostery is an important phenomenon that accounts for the regulation of the activity of many enzymes and regulatory proteins. To study the mysterious mechanism of protein allostery, human adult hemoglobin (HbA) serves as a paradigm and offers the best platform for developing mechanistic insights. Instead of purifying protein sample from blood donors, I used recombinant Hb (rHb) in this thesis, due to the convenience of performing site-directed mutagenesis and the possibility of obtaining a substantial amount of protein sample.

In this thesis, Chapter 1 introduces the research progress of the quaternary and tertiary dynamics of HbA, meanwhile, describes the principle of resonance Raman spectroscopy and its applications in studying Hb. Chapter 2 illustrates the experimental methods in detail, including mutagenesis, protein expression, time-resolved resonance Raman measurement, and spectral analysis.

Chapter 3 aims to identify an appropriate expression plasmid of rHb. The *Escherichia coli* (*E. coli*) expression system has a defect when it expresses rHb. Two strategies have been used to circumvent this problem. The pSGE1702 plasmid utilizes one strategy and yields the α(V1M)/β(V1M) double mutant, whereas the pHE7 plasmid adopts the other strategy and is capable of expressing normal rHb. The α(V1M)/β(V1M) double mutant has been suggested as a suitable surrogate of HbA in many respects, however, to our knowledge, its structural dynamics along the R→T transition pathway has not been examined yet.

In Chapter 3, the temporal behavior of time-resolved RR spectra of two recombinant Hbs, the α(V1M)/β(V1M) double mutant and normal rHb, as well as HbA isolated from blood, was investigated in detail. The results demonstrates that the structural dynamics of α(V1M)/β(V1M) double mutant were distinct from those of HbA in the tens of microseconds region, whereas the spectral changes of normal rHb and HbA were similar. Two valuable insights are obtained from this study: (1) Normal rHb expressed from the pHE7 plasmid better mimics HbA from blood, as compared with the α(V1M)/β(V1M) double mutant. Therefore, in Chapter 4, the pHE7 plasmid, not the pSGE1702 plasmid, was used as a starting point to perform site-directed mutagenesis. (2) It is the first time to reveal that structural changes in the N-termini are involved in the second step of the R→T quaternary transition of HbA. This finding helps further characterize the protein dynamics regulating the allosteric pathway of Hb.

The purpose of Chapter 4 is to characterize the tertiary structural changes, which are indispensable in realizing the quaternary transition of Hb. Hb Kempsey and Hb Kansas are two naturally occurring Hb mutants. Hb Kempsey is restricted in R quaternary state, whereas Hb Kansas is constrained in T quaternary state in the presence of IHP. Since no quaternary transition occurs, these two Hb mutants are appropriate candidates to investigate the tertiary dynamics in R and T quaternary states. Nevertheless, in Chapter 4, we did not purify protein sample from blood donors, ascribed to several disadvantages of using naturally occurring Hb mutants. Instead, since the mutation sites of Hb Kempsey and Hb Kansas have already been reported, we constructed two mutant plasmids using pHE7 as a template, and produced rHb Kempsey and rHb Kansas utilizing the *E. coli* expression system. For convenience, in Chapter 4, rHb Kempsey and rHb Kansas are called R and T mutants, respectively.

After successfully producing a large amount of R and T mutants, we applied the time-resolved resonance Raman spectroscopy to study their tertiary dynamics, and made a comparison with the dynamics of wild-type rHb. The ν(Fe-His) frequency and ν_8 intensity used in Chapter 3 were also used in this Chapter as Raman markers to monitor the dynamics of rHb species. Besides that, two new structural markers were also used, i.e. the ν_4 and ν_3 bands. The results revealed that the tertiary structural changes within T quaternary state were decelerated by one order of magnitude, as compared with the tertiary structural changes within R quaternary state. The other observation is that the core size is difference between R and T quaternary states, which may provide a possible explanation for the deceleration of structural changes within T quaternary structure. Another important finding is that the frequency of ν(Fe−His) and of ν_4 were shown to be linearly inverse correlated in the time-evolution data. These findings help further characterize the protein dynamics regulating the allosteric pathway of Hb.

In summary, in this thesis, the structural changes of several rHb species were monitored using time-resolved Raman spectroscopy, the results of which provide valuable insights into understanding the quaternary and tertiary dynamics of HbA.

List of Publications

Paper

1) Effect of the N-terminal residues on the quaternary dynamics of human adult hemoglobin.

Shanyan Chang, Misao Mizuno, Haruto Ishikawa, and Yasuhisa Mizutani

Chem. Phys. **469–470**, 31–37 (2016).

Acknowledgment

This thesis is a summary of author’s studies from 2013 to 2016 at Department of Chemistry, Graduate School of Science, Osaka University. This work is carried out under the supervision of Prof. Yasuhisa Mizutani at Osaka University. The author would like to express her sincerest gratitude for his fruitful discussion and affectionate guidance and encouragement through her study and for his leading her to an exciting scientific field of time-resolved resonance Raman spectroscopy.

This work would not been possible without help of all the members in Mizutani Laboratory. The author is grateful for their variable discussions and friendly encouragement, in particular to Dr. Misao Mizuno and Dr. Haruto Ishikawa. She is thankful to all other Lab members for their hearty kindness both at and out work.

The author thanks Prof. John S. Olson and Dr. Eileen Singleton of Rice University for providing the pSGE1702 plasmid and E. Coli SGE1661, and the protocols for protein expression and purification. She thanks Prof. Chien Ho of Carnegie Melon University for donating the E. coli Hb expression plasmid pHE7 and instructions for protein expression and purification. She is grateful to Prof. Masako Nagai of Hosei University for her valuable advice on the preparation of normal rHb. She thanks Prof. Shigenori Nagatomo of the University of Tsukuba and Prof. Tomohisa Takaya of Gakushuin University for valuable discussion on the data analysis.

The author thanks the support from a Grant-in-Aid for Scientific Research on Innovative Areas “Soft Molecular Systems” (No. 25104006) to Y.M. from the Ministry of Education, Culture, Sports, Science and Technology of Japan, and the financial support from China Scholarship Council.

Finally, the author expresses the greatest gratitude to her mother and husband for their continuous encouragement throughout her study, she loves them forever.